Savannah River National Laboratory®

A U.S. DEPARTMENT OF ENERGY NATIONAL LAB • SAVANNAH RIVER SITE • AIKEN, SC • USA

Direct Stabilization of LAW with Advanced Engineered Cellular Magmatics

Hanford Road Map Project No. 277995 Year 1 Report

Cory L. Trivelpiece, Elizabeth M. Tsekrekas, Robert Hausrath, Alex D. Cozzi, Gert Nielsen, Kathleen Richardson, Rashi Sharma, Kevin Brown, David Kosson, Lesa Brown, Collin Wilkinson, Lauren Meyer, Noah Koltenuk

September 2025

SRNL-TR-2025-00597

srnl.gov

DISCLAIMER

Printed in the United States of America

Prepared for
U.S. Department of Energy

Direct Stabilization of LAW with Advanced Engineered Cellular Magmatics

Hanford Road Map Project No. 277995 Year 1 Report

Cory L. Trivelpiece, Elizabeth M. Tsekrekas, Robert Hausrath, Alex D. Cozzi, Kathleen Richardson, Rashi Sharma, Kevin G. Brown, David Kosson, Lesa Brown, Collin Wilkinson, Noah Koltenuk, Lauren Meyer, Gert Nielsen

September 2025

Savannah River National Laboratory is operated by Battelle Savannah River Alliance for the U.S. Department of Energy under Contract No. 89303321CEM000080

Reviews and Approvals

AUTHORS:

CORY TRIVELPIECE (Affiliate)
Digitally signed by CORY TRIVELPIECE (Affiliate)
Date: 2025.09.03 14:27:25 -04'00'

Cory L. Trivelpiece, Glass, Cement and Ceramic Sciences, SRNL

ELIZABETH TSEKREKAS (Affiliate)
Digitally signed by ELIZABETH TSEKREKAS (Affiliate)
Date: 2025.09.03 15:44:36 -04'00'

Elizabeth M. Tsekrekas, Glass, Cement and Ceramic Sciences, SRNL

TECHNICAL REVIEWERS:

BRINLEY SWANSON (Affiliate)
Digitally signed by BRINLEY SWANSON (Affiliate)
Date: 2025.09.08 14:47:02 -04'00'

Brinley Swanson, Glass, Cement and Ceramic Sciences, SRNL

APPROVAL:

WILLIAM JOLIN (Affiliate)
Digitally signed by WILLIAM JOLIN (Affiliate)
Date: 2025.09.08 22:41:17 -04'00'

William Jolin, Manager, Glass, Cement, and Ceramic Science, SRNL

JOSEPH MANNA (Affiliate)
Digitally signed by JOSEPH MANNA (Affiliate)
Date: 2025.09.09 07:46:17 -04'00'

Joseph Manna, Director,
Materials Technology & Energy Sciences Division
Environmental & Legacy Management Directorate, SRNL Date

Acknowledgements

The work presented in this report was funded by the U.S. Department of Energy - Office of Environmental Management, Hanford Roadmap Lab Call Program Award No. 277995. The PIs would like to thank Ming Zhu and John Kelly for their tremendous efforts at enabling the success of the EM Lab Call program.

Executive Summary

This report summarizes our team's efforts throughout Year 1/Phase 1 of the Hanford Lab Call Project No. 277995. The primary focus of this work is to develop an alternative technology for the disposition of low activity waste (LAW) generated at the Hanford site. For the past six years, SRNL and its partners have been developing engineered cellular magmatics (ECMs) – ECMs are porous, glass ceramics that are primarily synthesized from repurposed materials destined for landfills (e.g., post-consumer glass). The goal of this work is to develop an ECM that reacts cementitiously with LAW streams to produce grout or geopolymer-like waste forms that are suitable for permanent disposition at off-site locations. The go/no-go milestone for Year 1 was to produce a lab-scale quantity of ECM that reacted with LAW simulant resulting in a product that was solid and had no free-standing liquid upon the completion of the main reaction.

Section 1 of the report details the development of an ideal glass composition (IGC) space that was designed to mimic the properties of grout premix materials: ordinary Portland cement (OPC), Class F fly ash, and blast furnace slag (BFS). The resulting designs yielded 16 glasses that had a similar composition to BFS. Nearly all of these glasses were inverted, meaning that the ratio of modifier to network former was significantly higher than typical glass compositions. As a result, many of these compositions were unstable under plate quenching conditions and crystallized into mineral phases that rendered them unusable for cementitious materials. To investigate the stability of this glass compositional space, we synthesized an additional 16 uniformly spaced glasses (USG) that shed light on the relationship between glass stability and cementitious reactivity. Out of the original 16 IGC glasses, 9 compositions were sufficiently stable to warrant further investigation. All the USG glasses were stable upon plate quenching.

Section 2 of the report covers budget and schedule details for year 1 of the work.

Section 3 – Section 6 of the report documents the various characterization methods and measurement results used to classify the properties of the IGC and USG compositions. We focused on determining the following: glass structure through the use of Raman spectroscopy, thermal properties of the glasses (such as viscosity and differential scanning calorimetry), and isothermal calorimetry to measure cementitious reactivity. We drew correlations between the glass structure and thermal measurements to cementitious reactivity allowing us to understand the compositional mechanisms driving the reactivity of supplemental cementitious materials like BFS. All of the glasses that were synthesized in the IGC and USG series demonstrated some degree of cementitious reactivity when in contact with the simulated LAW.

The extensive characterization was valuable in guiding experimental direction during Phase 1, as well as, being used as inputs for physics-driven machine learning and predictive modeling, which is described in Section 7. The compositional space for the IGC and USG glasses is sparse in terms of historical data; therefore, the measurements made during Phase 1 provided invaluable data for improving model uncertainty. Furthermore, we developed novel algorithms to determine "foaming windows" for the glasses in this compositional space as well as more traditional glass forming regions. The foaming window provides processing parameters that are optimized to produce ECMs with tailored properties for given applications.

Section 8 describes our efforts to understand the slag dissolution phenomenology associated with historical grout samples – efforts were taken to characterize legacy grout samples through scanning electron microscopy (SEM) and energy dispersive X-ray spectroscopy (EDS). Our

measurements revealed that the slag particles form a sort of “surface rind” like material with a significantly different composition than the bulk slag or the surrounding cementitious matrix. These studies are ongoing and will help our team understand how to target certain ECM properties throughout the course of the remaining work.

Section 9 of the report outlines our approach at determining the industrial scalability index (ISI) of our proposed solutions. This technoeconomic analysis serves several important functions related to guiding experimental directions and product development. Most importantly, the ISI is a metric that can quickly determine if a potential solution is cost and time-competitive with alternative technologies enabling us to rapidly design experiments focused on the ultimate goal, rather than optimizing technologies at the lab-scale that will not be transferrable to industrial scale processes. The primary findings of the Phase 1 ISI work indicate that when considering IGC-type glasses, the best available option would be to add the glass fabrication facility to the front-end of the ECM processing line rather than offload that aspect of the material production to a third-party producer. While this would significantly enhance the initial capital expenditure of our technology, that cost would be recovered within years when compared to using a third-party producer.

The final section of the report highlights the completion of the first go/no-go milestone. The criteria associated with Milestone 1 was:

“Production of one or more ECM materials based on the IGC that are cementitiously reactive in the presence of simulated LAW streams.”

To that end, we successfully demonstrated the production of an ECM based on a modified-IGC composition that showed remarkable absorption capacity for water (nearly ~80% by mass) as well as cementitious reactivity. The final product, once removed from the isothermal calorimeter, was a solid, pelletized waste with no free-standing liquid present in the test vial. The formation of calcium silicate hydrate (CSH)-like phases was indicated through SEM analysis. This final form would be suitable for permanent disposal at an off-site, commercial repository.

Table of Contents

List of Tables

List of Figures

List of Abbreviations

SRNL	Savannah River National Laboratory
ECM	Engineered Cellular Magmatic
LAW	Low-activity Waste
WTP	Waste Treatment and Immobilization Plant
IDF	Integrated Disposal Facility
WRPS	Washington River Protection Solutions
NAS	National Academy of Sciences
NNLEMS	Network of National Laboratories for Environmental Management
FFRDC	Federally-funded Research and Development Center
NDAA	National Defense Authorization Act
SLAW	Supplemental LAW
OPC	Ordinary Portland Cement
CRESP	Consortium for Risk Evaluation with Stakeholder Participation
IGC	Ideal Glass Composition
DOEx	Design of Experiments
BFS	Blast Furnace Slag
FA(F)	Class F Fly Ash
USG	Uniform Spacing Glasses
DSC	Differential Scanning Calorimetry
XRD	X-ray Diffraction
PPV	Parallel-plate Viscometry
SLS	Soda-lime Silicate Glass
BO	Bridging Oxygen
FWHM	Full Width Half Maximum
MAS NMR	Magic-angle Spinning Nuclear Magnetic Resonance
ITC	Isothermal Calorimetry
SEM	Scanning Electron Microscopy
EDS	Energy Dispersive X-ray Spectroscopy
ISI	Industrial Scalability Index
DWPF	Defense Waste Processing Facility
SRS	Savannah River Site
TPY	Tons Per Year
ROM	Rough Order of Magnitude
CSH	Calcium Silicate Hydrate

1. Introduction

Our team, led by the Savannah River National Laboratory, was selected to investigate the "Direct Stabilization of LAW with Advanced Engineered Cellular Magmatics" as a part of the Hanford Lab Call projects awards (Award No. 277995). The primary objective of this program is to develop an advanced engineered cellular magmatic (ECM) composition/system that is cementitiously reactive with low-activity salt waste streams. In other words, when the material comes into contact with low activity waste, it will react to form cementitious phases (e.g., calcium silicate hydrates) that solidify into a waste form suitable for permanent disposal.

ECMs are a synthetic, pumice-like material traditionally made from upcycled silica-based waste products such as post-consumer (i.e., "recycled" glass). In 2019, SRNL developed the first generation of ECMs to mimic the chemical, mineralogical, and physical properties of volcanic materials used in ancient Roman concrete – this volcanic tephra is hypothesized to be one of the key ingredients giving ancient Roman concrete its unparalleled durability. From this foundation, SRNL researchers and industry partners have developed a wide-array of ECM materials suitable for applications ranging from wastewater filtration to biological substrates for hydrocarbon-remediating microbes.

1.1 Problem Statement

The Department of Energy Office of Environmental Management is tasked with disposing of more than 56 million gallons of radioactive and hazardous waste stored in 177 underground storage tanks at the Hanford Site in southeastern Washington State. The Hanford Tank Waste Treatment and Immobilization Plant (WTP) is being constructed to treat these wastes and immobilize them in a glass waste form. At least a portion (~35%) of the Low Activity Waste (LAW) will be converted to glass in the LAW vitrification facility and will be disposed of onsite at the Integrated Disposal Facility (IDF). However, a second facility will be needed for the expected volume of LAW requiring immobilization.

Revision 7 of the Washington River Protection Solutions[1] (WRPS) Technology and Innovation Roadmap identifies the need for technology maturation efforts to enable solidifying Supplemental Low Activity Waste (SLAW) into a cementitious waste form [1]. Recent evaluations by the National Academies of Sciences, Engineering and Medicine (NAS) [2], the Network of National Laboratories for Environmental Management and Stewardship (NNLEMS) [3], and a Federally Funded Research and Development Center (FFRDC) as part of Section 3125 2022 National Defense Authorization Act (NDAA) [4] have noted that an improved containerized grout formulation and process can facilitate the implementation of SLAW should a grout waste form be selected for on-site disposal. In the River Protection Project System Plan revision 9, the system description for Low-Activity Waste Supplemental Treatment identified the need for a future facility regardless of the treatment technology implemented [5]. As such, there is a great deal of flexibility in terms of preparation and processing methodologies as well as types of media that will be applied for the disposition of this waste.

Our technology is an alternative to traditional grout-based waste forms. Rather than requiring the use of premix materials such as ordinary Portland cement (OPC), slag, or fly ash, our

[1] Washington River Protection Solutions is the former liquid waste contractor at the Hanford Site.

materials react cementitiously with waste streams in a one-step process (i.e., direct stabilization) to solidify high ionic strength, high pH solutions. The main advantage of this technology is the elimination of grouting facilities to mix materials, drastically reducing the capital expense and on-site operations required to disposition a LAW stream. Furthermore, our technology will ideally eliminate the dependence of low-activity waste disposition on high-demand construction products such as, fly ash and blast furnace slag while simultaneously lowering the amount of OPC needed to produce stabilized waste forms.

1.2 Team

The team consists of SRNL as the lead institution with Dr. Cory Trivelpiece as the lead PI. SRNL is responsible for program management, ECM formulation development, and waste form development. Our industry partner, Silica-X, Inc. (co-PI, Gert Nielsen), is responsible for techno-economic analyses and industrial scalability, as well as producing pilot-scale quantities of ECM materials for testing. Our academic partners Alfred University (co-PI, Prof. Collin Wilkinson) is responsible for computational glass science and predictive modeling via machine learning; University of Central Florida (co-PI, Prof. Kathleen Richardson) is responsible for glass characterization and compositional development, and Vanderbilt University/CRESP (co-PI, Dr. Kevin Brown) is responsible for waste form characterization and testing. The full team breakout is shown in Figure 1.

Lead: Cory Trivelpiece	**Lead:** Gert Nielsen	**Lead:** Collin Wilkinson	**Lead:** Kathleen Richardson	**Lead:** Kevin Brown
• Alex Cozzi • Elizabeth Tsekrekas • Rob Hausrath • Ben Pershing • Ethan Pham • Madison Hsieh	• Rob Hust • Philip Galland • Chris Lynch	• Lauren Meyer • Noah Koltenuk	• Rashi Sharma	• David Kosson • Lesa Brown

Figure 1: The breakout of Project 277995 team as of the completion of Year 1 of the program.

1.3 Project Plan

The work conducted under this program is divided into four phases spanning three years of work. The various aspects of the phases are detailed here:

Phase 1 – Design of an ideal glass composition (IGC) that mimics the properties of grout waste form-based premix materials.

Phase 2 – Investigate the use of alternative feedstock materials to produce glass compositions and ECMs that have similar cementitious reactivity to the properties of the initial IGCs.

Phase 3 – Functionalization of the ECM materials to enhance their capabilities at sequestering various high-mobility contaminants with similar or better retention capacities than current waste forms.

Phase 4 – Pilot-scale demonstration of the technology with a simulated LAW stream.

A detailed project plan was given in the initial proposal and the work breakdown structure for this research is shown in Figure 2.

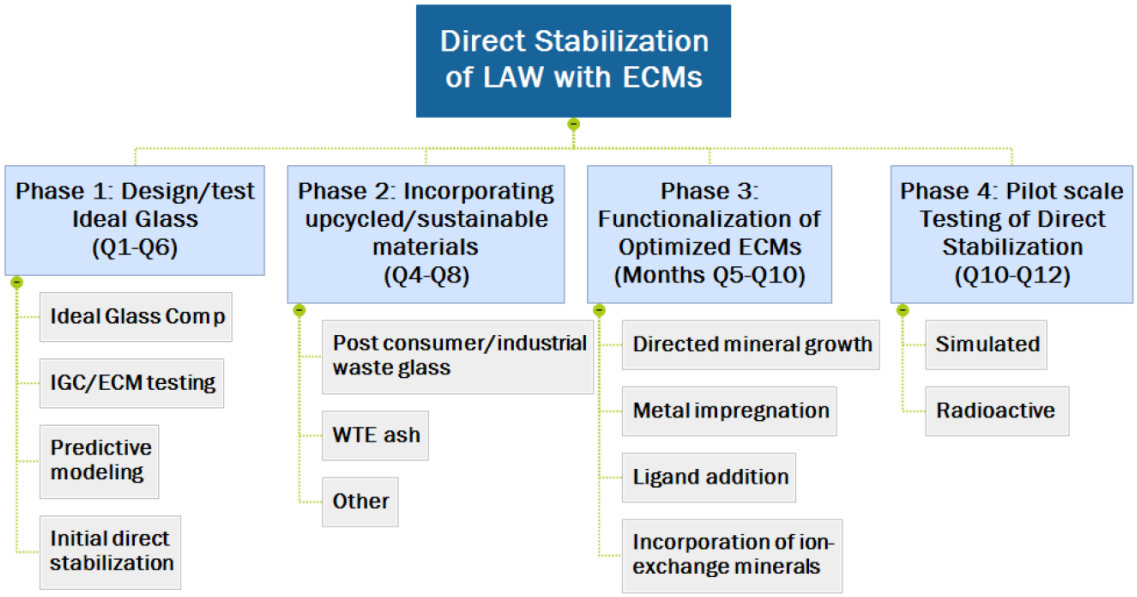

Figure 2: Work breakdown structure for the four phases of work showing the tasks and subtasks along with proposed timing.

2. Schedule and Budget Review

2.1 Schedule

The Figure 3 Gantt Chart shows the schedule for Year 1 along with the completion percentage of each of the scheduled tasks. As of the end of Year 1, we were ahead of schedule with the overall project progress and had successfully completed the go/no-go milestone set forth in the proposal for Phase 1 (Section 10). Phase 2 work will begin in Year 2 concurrently with the completion of the remaining Phase 1 tasks.

Task Name	Start	Finish	% Complete
1. Phase 1	**Mon 4/1/24**	**Tue 9/30/25**	**79%**
1.1 Synthesize IGC	**Mon 4/1/24**	**Mon 3/31/25**	**94%**
1.1.1 ID Compositional Space	Mon 4/1/24	Sun 6/30/24	100%
1.1.2 Model IGC properties (current models)	Mon 4/1/24	Fri 9/27/24	100%
1.1.3 IGC Batch Synthesis	Mon 7/1/24	Fri 12/27/24	100%
1.1.4 IGC-ECM Synthesis	Tue 10/1/24	Mon 3/31/25	80%
1.2 IGC/ECM Characterization/testing	**Mon 7/15/24**	**Mon 6/30/25**	**83%**
1.2.1 Aqueous Testing	Mon 7/15/24	Tue 1/14/25	80%
1.2.2 Detailed Viscosity Measurements	Tue 10/1/24	Mon 3/31/25	90%
1.2.3 XRD of IGC/ECMs	Tue 10/1/24	Mon 6/30/25	80%
1.3 Modeling/optimization of IGC properties	**Tue 10/1/24**	**Tue 9/30/25**	**74%**
1.3.1 MD	Tue 10/1/24	Mon 3/31/25	80%
1.3.2 Statistical Mechanics	Wed 1/1/25	Mon 3/31/25	90%
1.3.3 Machine Learning	Wed 1/1/25	Mon 6/30/25	85%
1.3.4 Lab-scale synthesis of optimized IGCs/ECMs	Tue 4/1/25	Tue 9/30/25	50%
1.4 Initial Direct Stabilization Tests	**Wed 1/1/25**	**Tue 9/30/25**	**61%**
1.4.1 Direct Stablization with ECMs	Wed 1/1/25	Mon 6/30/25	70%
Go/No-Go Demonstration of DS	Wed 4/2/25	Wed 4/2/25	100%
1.4.2 Evaluation of Novel Waste Forms	Tue 4/1/25	Mon 6/30/25	65%
1.4.3 Optimization of Direct Stablization Formulations	Tue 4/1/25	Tue 9/30/25	50%

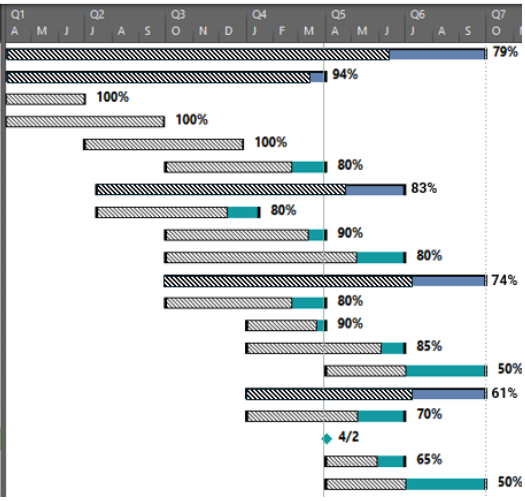

Figure 3: Gantt Chart showing the program progress as of March 31st, 2025.

2.2 Year 1 Budget Review

Figure 4 and Table 1 give the project's total budget information as of the end of program Year 1.

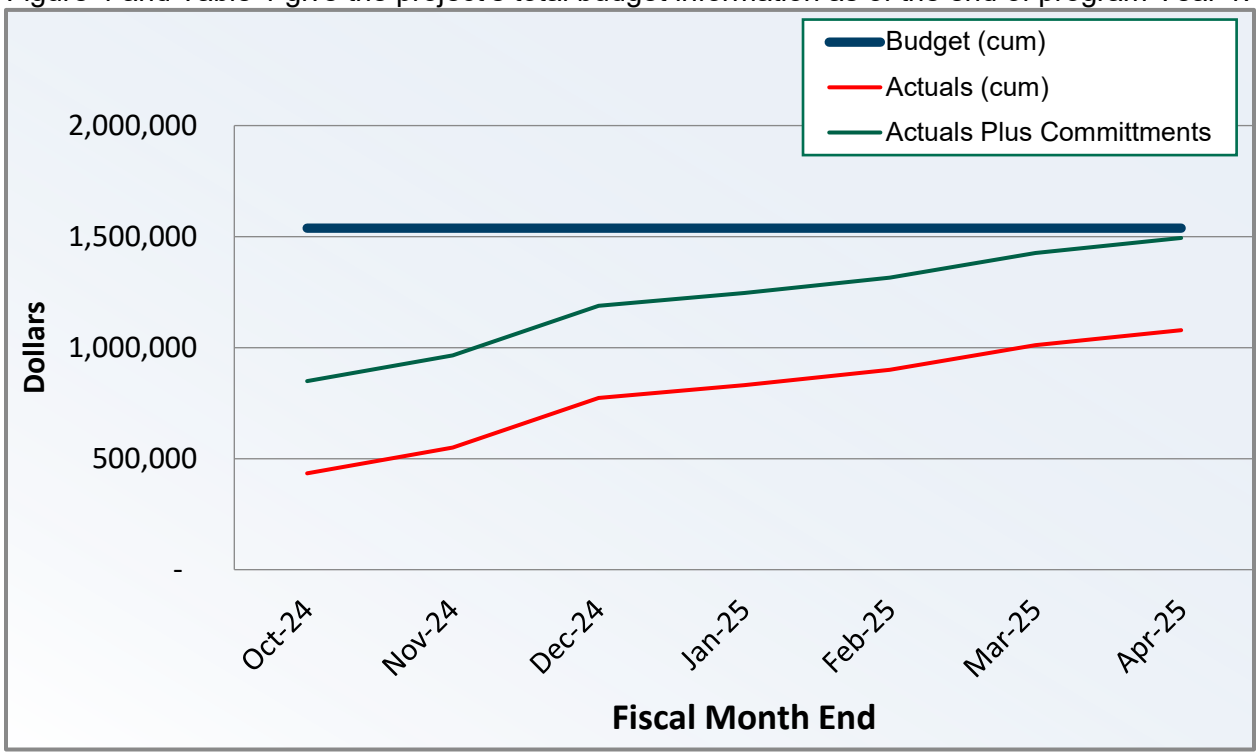

Figure 4: Budget information for Year 1.

Table 1: Budget information for Year 1

Fiscal Month	Carryover	Apr-24	May-24	Jun-24	Jul-24	Aug-24	Sep-24
Budget (cum.)		$ 893,998	$ 893,998	$ 893,998	$ 893,998	$ 893,998	$ 893,998
Actual Cost		$ 8,703	$ 52,724	$ 44,214	$ 75,498	$ 64,294	$ 113,492
Actuals (cum.)		$ 8,703	$ 61,427	$ 105,641	$ 181,139	$ 245,433	$ 358,925

Fiscal Month	Carryover	Oct-24	Nov-24	Dec-24	Jan-25	Feb-25	Mar-25	Apr-25
Budget (cum.)		$ 1,537,995	$ 1,537,995	$ 1,537,995	$ 1,537,995	$ 1,537,995	$ 1,537,995	$ 1,537,995
Actual Cost		$ 74,899	$ 115,782	$ 223,206	$ 57,884	$ 69,838	$ 110,580	$ 67,417
Actuals (cum.)		$ 433,824	$ 549,606	$ 772,812	$ 830,696	$ 900,534	$ 1,011,114	$ 1,078,531

Allocated Funding:	$	1,537,995
Actual Cost to Date:	$	1,078,532
Commitments:	$	415,366
Remaining Balance:	$	44,097

3. Design and Fabrication of Cementitious Glasses

We used a combination of historical reference data and statistical modeling to develop the initial composition space for the IGCs. Based on prior art related to Saltstone premix materials, we had an idea of what the IGC compositional space would look like prior to engaging in the design of the development of the IGCs. Wilhite and Langton[6] give the ranges in Table 2 as the "Acceptable Formulation Range for Saltstone".

Table 2: The premix material ranges used for the design of the IGC.

Material	Minimum	Reference	Maximum
Grade 120 Slag	10 wt.%	25 wt.%	40 wt.%
Class F Fly ash	10 wt.%	25 wt.%	40 wt.%
Cement or $Ca(OH)_2$	0 wt.%	3 wt.%	10 wt.%
Water/Total Solids (dry)	0.40	0.50	0.64

3.1 Design of the IGC System

These ranges were then used to initiate a “Design of Experiments (DOEx)” methodology to develop a set of compositions in the space of these three premix components along with the constraint of the water/total solids ratio. The initial design resulted in the various mixtures shown in the ternary of Figure 5.

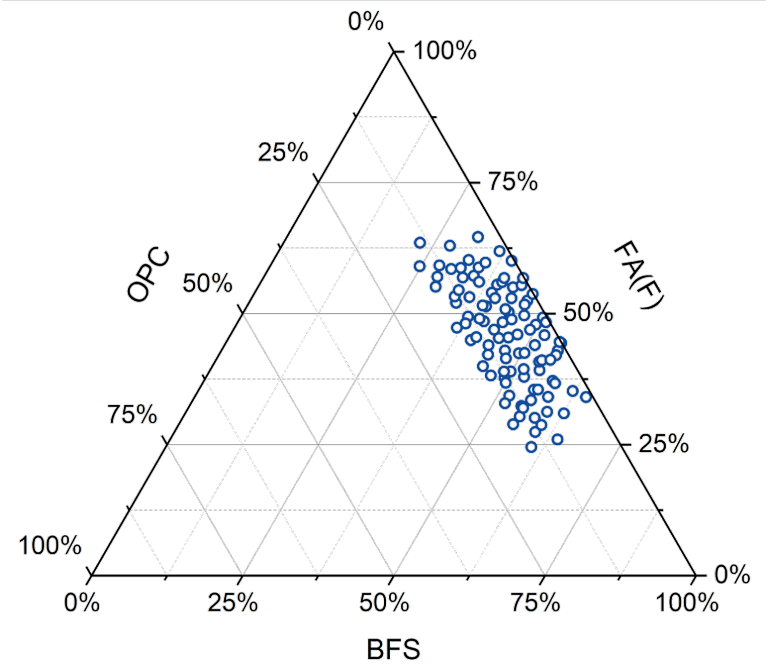

Figure 5: The ternary of possible premix compositions using the ranges given in Table 1 with a constraint based on the W/S ratio. The components shown in the ternary are blast furnace slag (BFS), Class F fly ash (FA(F)), and ordinary Portland cement (OPC).

We then transformed these premix compositions into their oxide components using data collected from a literature review. The minimum, maximum, and average values for common oxide components were determined based on the historical data show in Figure 6

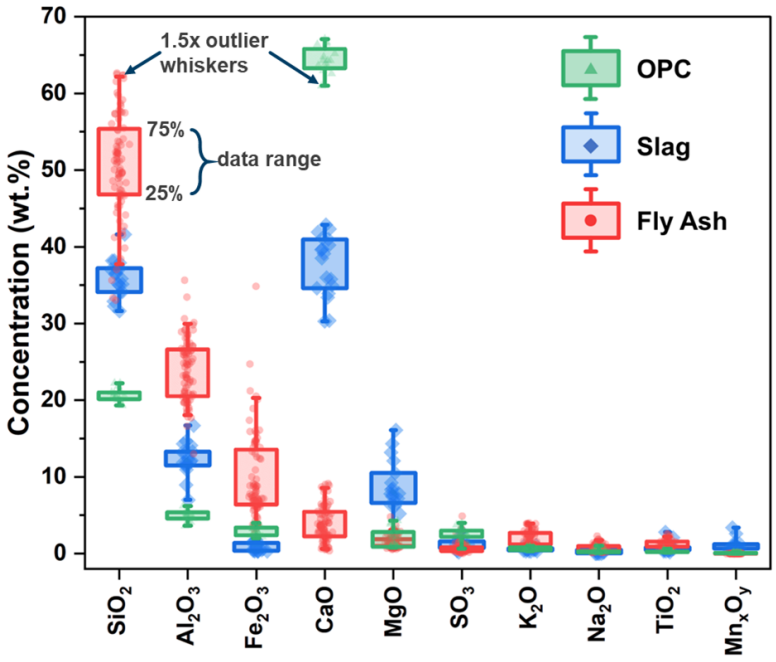

Figure 6: A literature review of historical composition data for premix component compositions in oxide form yielded the minimum and maximum values that were used in the transformation from the mixtures shown in Figure 5 to the actual IGC compositional space.

The transformation from premix compositional space to oxide compositional space was accomplished via the system of matrices shown in Equation 1.

$$\begin{pmatrix} F_1 & B_1 & O_1 \\ \vdots & \ddots & \vdots \\ F_N & B_N & O_N \end{pmatrix} x \begin{pmatrix} (R_xO_y)_{F_{min}} \\ (R_xO_y)_{B_{min}} \\ (R_xO_y)_{O_{min}} \end{pmatrix}_i , \begin{pmatrix} (R_xO_y)_{F_{max}} \\ (R_xO_y)_{B_{max}} \\ (R_xO_y)_{O_{max}} \end{pmatrix}_i = \left[(R_xO_y)_{min,i} , (R_xO_y)_{max,i} \right]_n \quad (1)$$

In Equation 1, F_n, B_n, and O_n are the weight percents of FA(F), BFS, and OPC, respectively, in a given mixture in Figure 5; $(R_xO_y)_{F_{min}}$ is the minimum concentration of a particular oxide (e.g., SiO_2) from the historical data shown in Figure 6, whereas $(R_xO_y)_{F_{max}}$ represents the maximum concentration of a particular oxide from the historical data shown in Figure 6. Thus, for a given mixture, n, in Figure 5, we arrive a minimum and maximum concentration for each oxide in the mixture, which is represented by the RHS of Equation 1. In an effort to simplify the first iteration of IGC designs, we limited the design to min/max values of SiO_2, Al_2O_3, CaO, and MgO, as we hypothesized these four oxides play the most significant roles in forming cementitious phases. We then used these mixtures to initiate another DOEx system to generate 1000 possible compositions for the IGC glasses in the space defined by the preceding efforts. These compositions are shown in Figure 7.

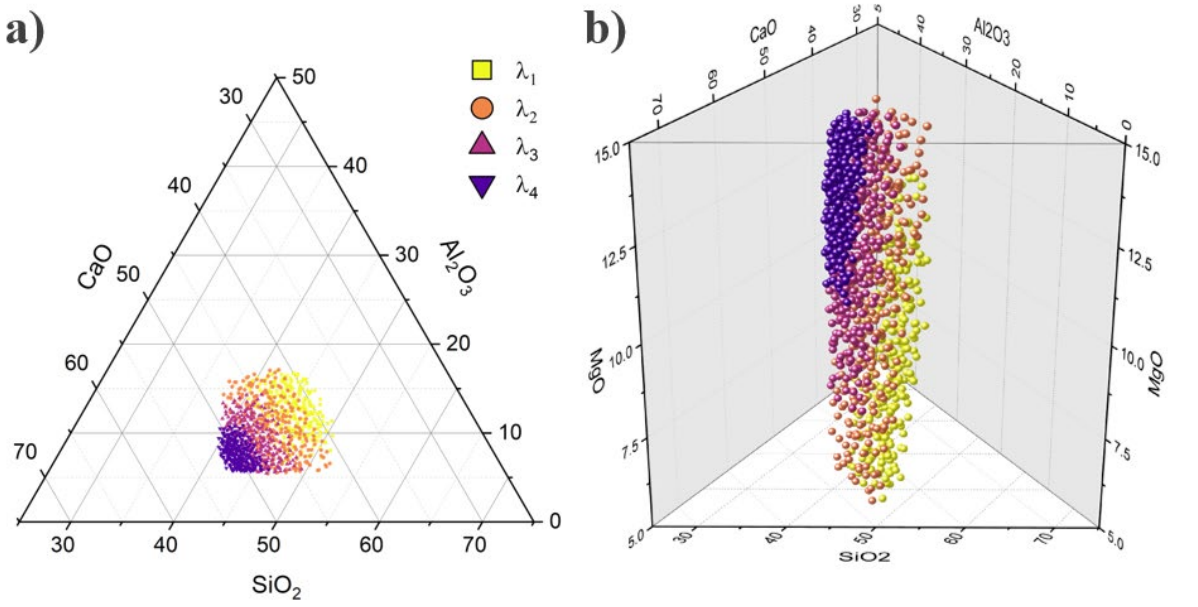

Figure 7: a) Ternary diagram showing the initial 1000 IGC designs and b) a 3D ternary showing the MgO concentration on the height axis.

These 1000 compositions were categorized into different groups according to a ratio, λ, given in Equation 2, that is hypothesized to give an estimation of the phases that form while the composition undergoes a cementitious reaction [7].

$$\lambda = \frac{\mathrm{CaO} + \mathrm{MgO}}{\mathrm{SiO_2} + \mathrm{Al_2O_3}} \tag{2}$$

Where the four λ groups are defined by the following ranges:

$$0.85 < \lambda_1 < 0.95 \tag{3}$$
$$0.95 < \lambda_2 < 1.10 \tag{4}$$
$$1.10 < \lambda_3 < 1.25 \tag{5}$$
$$1.25 < \lambda_4 < 1.40 \tag{6}$$

And CaO, MgO, SiO_2, and Al_2O_3 represents the concentration of these oxides in wt.%. From these 1000 glasses, we down-selected four compositions from each λ group. The down-selected compositions are shown in Figure 8.

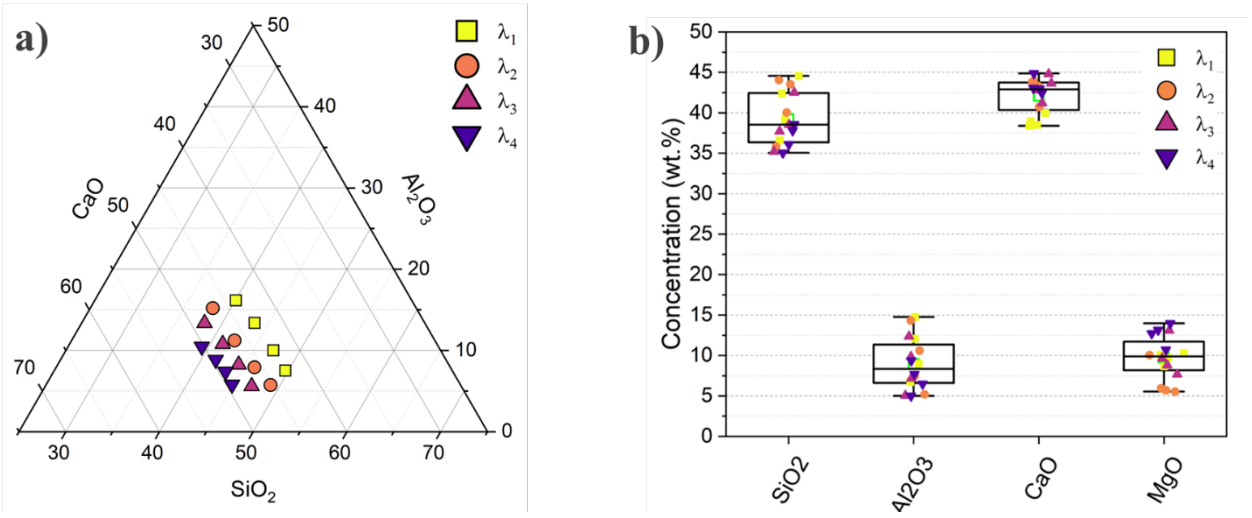

Figure 8: a) Ternary diagram of the initial 16 down-selected IGC glasses, and b) a box plot showing the distribution of these oxides.

Inspection of Figure 8a reveals the compositional "consequences" of the λ-constraints. That is to say, not all regions of the compositional space are accessible for all λ groups. In Figure 9a and 9b, we show the same ternary as in Figure 8a but with the phase diagrams for the SiO_2-Al_2O_3-CaO system superimposed.

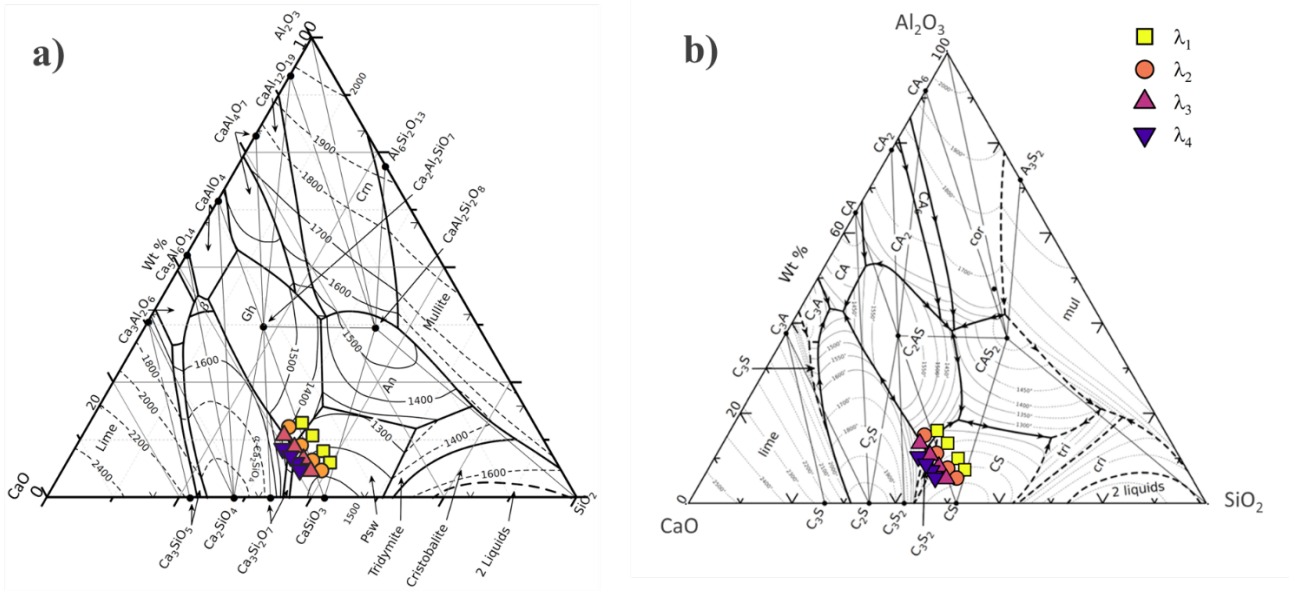

Figure 9: The initial 16 IGCs overlayed onto phase diagrams in the SiO_2-Al_2O_3-CaO system - a) shows the phases in ceramist's notation and b) shows the phases in cement science notation. The four sets of compositions indicated by lambda (1-4) are shown on both plots for comparison.

Interestingly, the compositions of the IGC in this ternary are very similar to that of BFS, which is known to be cementitious in salt waste systems. In Figure 10a,b, the historical data for OPC, BFS, and FA(F) are displayed on the two phase diagrams in Figure 9a,b.

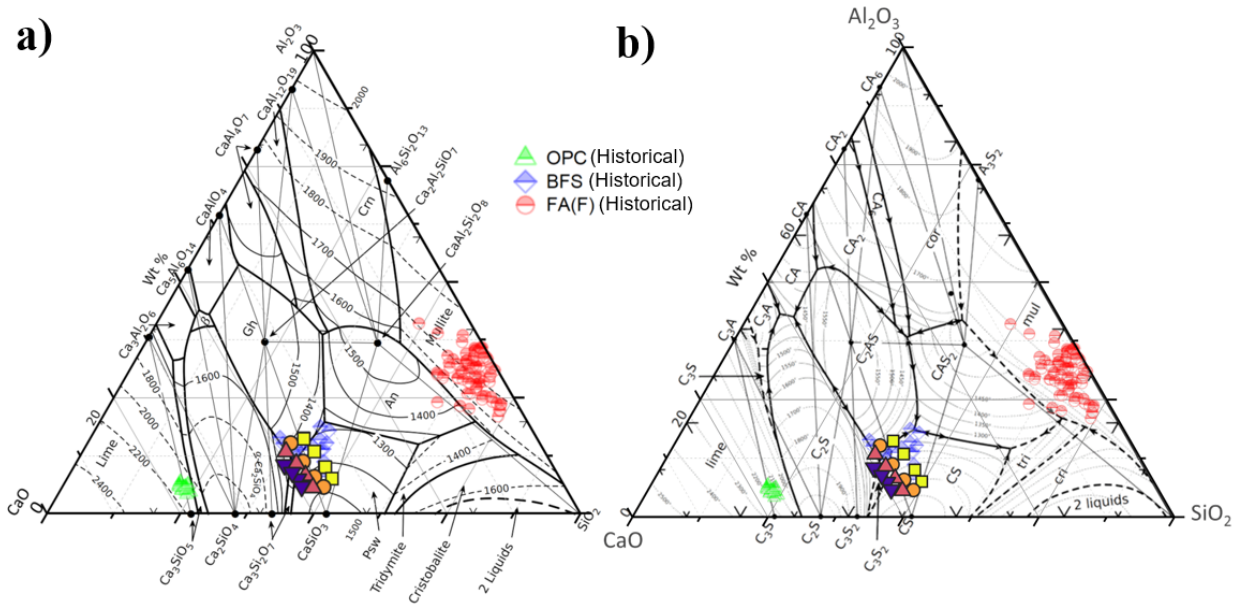

Figure 10: The same phase diagrams shown in Figure 9 with the historical data for OPC, BFS, and FA(F) shown for reference.

The compositions of the 16 IGC glasses are given in Table 3.

Table 3: The compositions of the original IGCs fabricated in these experiments. The table is color-coded to the λ-group of the compositions shown in Figure 10.

Glass ID	Group	SiO_2 (wt%)	Al_2O_3 (wt%)	CaO (wt%)	MgO (wt%)	SiO_2 (mol%)	Al_2O_3 (mol%)	CaO (mol%)	MgO (mol%)
DOE210	λ_1	42.39	9.00	38.52	10.09	40.76	5.10	39.68	14.46
DOE12	λ_1	36.60	14.76	39.97	8.66	36.23	8.61	42.39	12.78
DOE237	λ_1	44.57	6.74	38.40	10.29	42.43	3.78	39.18	14.60
DOE45	λ_1	39.22	12.08	38.97	9.74	38.22	6.94	40.69	14.14
DOE347	λ_2	43.54	7.48	43.30	5.68	42.35	4.29	45.13	8.23
DOE360	λ_2	40.03	10.61	43.82	5.53	39.45	6.16	46.27	8.12
DOE322	λ_2	35.81	14.32	43.93	5.94	35.75	8.43	46.99	8.83
DOE414	λ_2	44.05	5.18	40.73	10.04	41.67	2.89	41.28	14.16
DOE596	λ_3	42.50	5.06	42.79	9.65	40.20	2.82	43.37	13.61
DOE745	λ_3	35.20	12.35	44.79	7.66	34.55	7.14	47.11	11.20
DOE703	λ_3	37.70	9.84	43.65	8.81	36.46	5.61	45.24	12.69
DOE578	λ_3	38.52	7.17	41.21	13.10	36.19	3.97	41.49	18.35
DOE915	λ_4	35.06	9.37	44.86	10.70	33.51	5.28	45.95	15.25
DOE806	λ_4	37.82	6.47	42.99	12.72	35.46	3.58	43.19	17.77
DOE959	λ_4	36.10	7.70	43.05	13.15	33.94	4.26	43.37	18.42

DOE837	λ_4	38.57	5.00	42.45	13.98	35.77	2.73	42.18	19.32

3.2 IGC Glass Synthesis

We started to synthesize the IGCs in late FY24 initially melting the λ_1 glasses. We immediately observed some notable behavior in these glass systems:

1. The glasses have a high liqiudus temperature, in some cases >1500 °C, relative to soda lime silicate glasses that are typically used for ECM synthesis (~1000-1100 °C).
2. The viscosity of the glasses at the melting was very low – the glasses were extremely fluid when poured compared to soda lime silicate glass (e.g., the IGC glasses poured more like water, whereas soda lime silicate glasses pour more like syrup).
3. Some minor crystallization was observed on the melt patties for the λ_1 glasses.

The glasses were melted in Pt/Rh crucibles and poured onto stainless steel quench plates such that the resulting glass mass would be approximately 250 g. An image of the partial crystallization is shown in Figure 11a. Images of all the IGC melted and plate cooled glasses can be found in Appendix A. As we continued to melt the glasses, we noted increasing crystallization effects with increasing λ ratio, where only one composition from λ_3 and no compositions from λ_4 were stable upon plate cooling. An example of a significantly crystallized glass is shown in Figure 11b.

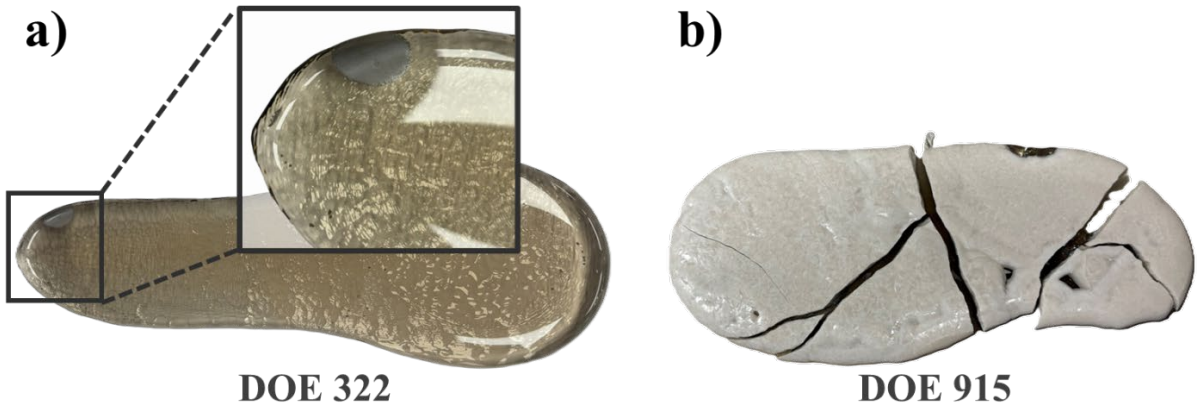

Figure 11: a) Photograph of a "stable" λ_1 glass, DOE 322, with the inset showing an enlarged view of the crystallized area, and b) photograph of λ_4 glass, DOE 915, that was significantly crystallized upon plate quenching.

We should note here that cementitiously reactive BFS, which is compositionally similar to the IGCs, is water quenched during the iron melting process. This water quenching, “locks” in the amorphous, glassy structure and cools the glasses sufficiently fast to prevent crystallization [8]. If the BFS is not water quenched during production, the material crystallizes into mineral phases. Similarly, we water quenched many of the unstable IGC glasses in small amounts and observed that these glasses were also stable if water quenched. Additionally, about 70 g of glasses was separated form the bulk and remelted for additional testing. These glasses were remelted for ~ 15 minutes at 1500 °C. Glasses were poured into small cylindrical graphite molds yielding “pucks” that were annealed at 725 °C for 1 hour for future processing.

3.3 Design of Uniform Spacing Glasses (USG)

The ISG compositions were designed via a stochastic process utilizing several criteria coupled with multiple constraints. We also designed and synthesized a set of glasses with uniform spacing to enable the study of compositional variability on phenomenological behaviors. These USG compositions are shown in the ternary and box plots in Figure 12 along with the IGC glasses. Due to the large amounts of crystallization observed on the λ_3 and λ_4 IGC glasses, we limited the design of the USGs to λ_1 and λ_2 ratios.

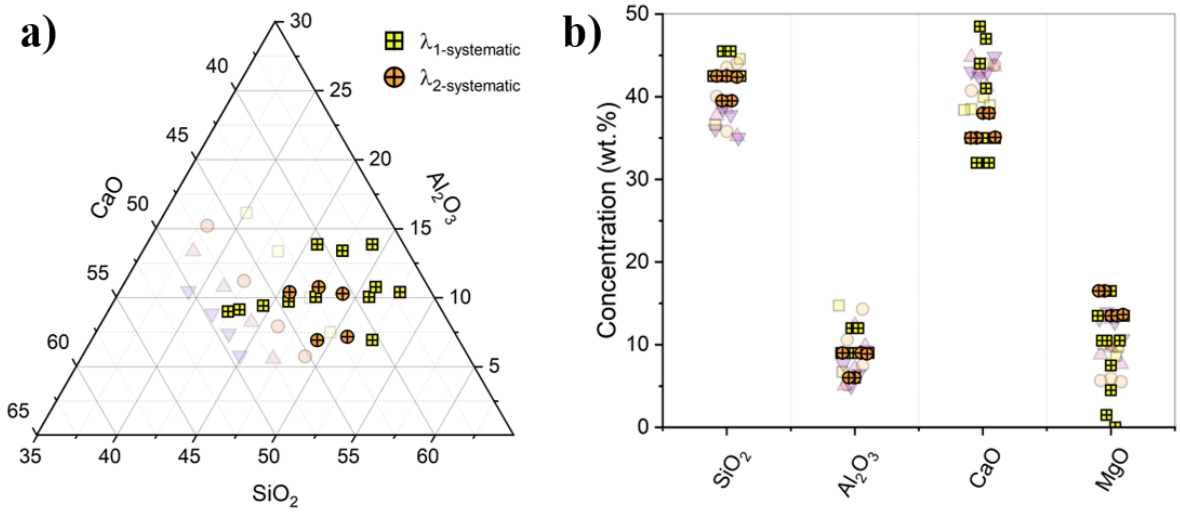

Figure 12: The ternary diagram (a) and box plot (b) of the USG systems with respect to the IGC glasses.

Inspection of the ternary diagram reveals that the USG glasses generally have a higher silicon concentration relative to the IGC glasses. The primary reason for including compositions with higher SiO_2 concentrations was to increase the stability of the glasses during plate cooling with the understanding that doing so would likely decrease the cementitious reactivity of these glasses. The compositions of the USG glasses are given in Table 4.

Table 4: The composition of the USG glasses.

Glass ID	Group	SiO_2 (wt.%)	Al_2O_3 (wt.%)	CaO (wt.%)	MgO (wt.%)	SiO_2 (mol%)	Al_2O_3 (mol%)	CaO (mol%)	MgO (mol%)
DOE1002	λ_1	45.5	6.0	35.0	13.5	42.7	3.3	35.2	18.9
DOE1003	λ_2	45.5	9.0	35.0	10.5	43.8	5.1	36.1	15.1
DOE1004	λ_2	45.5	9.0	32.0	13.5	43.2	5.0	32.6	19.1
DOE1005	λ_2	42.5	6.0	38.0	13.5	39.8	3.3	38.1	18.8
DOE1006	λ_1	42.5	9.0	38.0	10.5	40.8	5.1	39.1	15.0
DOE1007	λ_2	42.5	6.0	35.0	16.5	39.3	3.3	34.7	22.7
DOE1008	λ_2	42.5	12.0	35.0	10.5	41.4	6.9	36.5	15.2
DOE1009	λ_1	42.5	9.0	32.0	16.5	39.8	5.0	32.1	23.1
DOE1010	λ_2	42.5	12.0	32.0	13.5	40.9	6.8	33.0	19.4
DOE1011	λ_2	39.5	9.0	38.0	13.5	37.4	5.0	38.5	19.1

Glass ID	Group	SiO_2 (wt.%)	Al_2O_3 (wt.%)	CaO (wt.%)	MgO (wt.%)	SiO_2 (mol%)	Al_2O_3 (mol%)	CaO (mol%)	MgO (mol%)
DOE1012	λ_2	39.5	9.0	35.0	16.5	36.9	5.0	35.1	23.0
DOE1013	λ_1	39.5	12.0	35.0	13.5	37.9	6.8	36.0	19.3
DOE1014	λ_1	42.5	9.0	41.0	7.5	41.3	5.2	42.7	10.9
DOE1015	λ_1	42.5	9.0	44.0	4.5	41.8	5.2	46.4	6.6
DOE1016	λ_1	42.5	9.0	47.0	1.5	42.3	5.3	50.2	2.2
DOE1017	λ_1	42.5	9.0	48.5	0.0	42.6	5.3	52.1	0.0
DOE1001	λ_2	42.36	8.89	35.10	13.64	40.14	4.96	35.63	19.27
B2-Slag	λ_2	44.02	4.99	46.12	4.87	42.48	2.84	47.68	7.01

3.4 USG Glass Synthesis

The USG glasses were fabricated using the same method as the IGC glasses. Batches were prepared to yield approximately 250 grams of glass when melted. The glasses were melted in Pt/Rh crucibles at 1500 °C for approximately 3 hours and poured onto a stainless-steel plate to cool. Very minor crystallization was observed on some of these compositions, but none of the glasses showed the significant crystallization that was observed on many of the IGC glasses. After cooling, a portion of each glass was separated to be prepared for additional measurements using the same technique (puck and anneal) as was conducted for the IGC compositions.

Glasses labeled “DOE1001”, and “B2-Slag” were not part of the original IGC design but were fabricated as surrogates for BFS compositions that SRNL had characterized in past efforts. We include these glasses in the USG system because we have subjected these glasses to the same types of measurements that were performed for the IGC glasses.

We hypothesize that the greater stability observed in the USG glasses relative to the IGC glasses is caused by the increased SiO_2 concentration, or perhaps more accurately, the higher network former to network modifier ratios in these glasses.

4. Characterization of IGC/USG Glasses

Several techniques have been used to characterize the novel glass systems developed in this program including: viscosity measurements (rotating spindle and parallel plate), Raman spectroscopy, differential scanning calorimetry (DSC), heat treatments, and X-ray diffraction (XRD). The goal of these characterizations was two-fold: 1) develop a fundamental understanding of the phenomenological behavior of glass systems in a historically unexplored compositional space, and 2) generate data that covers existing gaps in compositional information to better train our predictive models. The following sections describe the results of the measurements we have performed to date.

4.1 Viscosity

Viscosities in the softening region (10^4 to 10^8 Pa·s) were measured using a parallel plate viscosity (PPV) method with a reproducibility of ± 3 °C. The sample height was monitored as a function of temperature and used to calculate the viscosity as shown below:

$$\eta = 2\pi \frac{Mgh^5}{30V\left(dh/dt\right)(2\pi h^3 + V)} \tag{7}$$

where η is the viscosity in poise, M is the applied load (grams), g is the acceleration due to gravity (cm/s^2), h is the sample height (cm) at time t (s), V is the sample volume (cm^3), and dh/dt is the compressive rate (cm/s). Rectangular samples (3-6 mm height and 8-12 mm sides) with parallel faces fine ground and polished were prepared from annealed “pucks”.

High temperature viscosity (1300 to 1500 °C) utilized a rotating spindle method where the spindle torque was considered to calculate viscosity as follows:

$$\eta = SC * TK/RPM \tag{8}$$

where SC is the spindle constant, TK is the percent torque and RPM represents the measured rotational speed of the spindle. Both the low temperature and high temperate viscosities were considered because of scarcity in the data associated with invert glasses within the IGC and USG compositional window. Data collected was directly incorporated into models to help improve the accuracy of the predictive modeling associated with the glasses. The graphs of the viscosity data can be found in Appendix B.

The softening region was of particular interest, since it directly overlaps with the foaming window of the glasses. By knowing the temperature associated with the foaming viscosity, it is possible to determine if $CaCO_3$ (a traditional foaming agent used for SLS) may be used as the foaming agent. From the low temperature viscosity curves, it is observed that the IGC and USG glasses show a steep viscosity curve. That is, compared to the viscosity curve of SLS glass, the change in temperature between viscosities is more rapid. In addition, the viscosity curves of the IGC and USG glasses are ~100 °C higher than that of SLS, indicating that a higher temperature is required to successfully foam the glasses. Finally, within the PPV measurements, the end point for the IGC and USG glasses is around 5 ± 5 Pa·s, whereas the viscosity of SLS could be measured the full range (down to 4 Pa·s). Indicating that the samples start to crystallize at a lower viscosity than SLS glass and are therefore less stable. Measurements in the high temperature viscosity region were difficult to obtain since the IGC and USG glasses tended towards crystallization, even at high temperatures. Because of this lack of stability in the glasses, it would be difficult to achieve industrial scalability with these compositions. This is consistent with observations made during melting, where small crystallites were seen on the glass surface after pouring.

4.2 Raman Spectroscopy

The high frequency Raman region (800 – 1200 cm^{-1}) in silicate and aluminosilicate glasses is primarily associated with the symmetric stretching of silicate units. More specifically, data can be used to qualitatively and/or quantitatively describe the tetrahedral units, or Q^n species, where n = 0 – 4 represents the number of bridging oxygen (BO) per tetrahedra. Within this region, the

local maxima associated with each Q^n species have been well defined and on average are as follows: Q^4 ~ 1200 cm^{-1}, Q^3 ~ 1050 – 1100 cm^{-1}, Q^2 ~ 950 – 1000 cm^{-1}, Q^1 ~ 900 cm^{-1}, and Q^0 ~ 850 cm^{-1} [9, 10]. The Q^n envelope for both the IGC and USC compositions all show three main bands centered at ~ 875 cm^{-1}, 945 – 965 cm^{-1}, and 1050 cm^{-1}, which are interpreted as the signal from Q^1, Q^2, and Q^3 respectively [11, 12]. Regardless of composition, the 1050 cm^{-1} mode has the lowest intensity and always appears as a shoulder to the main envelope. Conversely, the signal of the Q^1 and Q^2 species are seen to change intensity with composition of the glass.

Fitting of the high frequency Raman region gives quantitative information about the Q^n distribution of the silicate network, which can then be used to directly correlate property trends to the glass structure. Estimation of the silicate microstructure was determined using the relative intensity of fit bands associated with specific Q^n species. Due to the compositional complexity of the IGC and USC glasses, it was assumed that all Raman cross sections were equal to 1 and the presence of free oxygen in the system was neglected, yielding semi-quantitative data [13, 14]. Detailed fittings of each spectrum can be found in Appendix C.

Additionally, when fitting, the least number of bands possible were used to describe the Q^n distribution. It was found that all the spectra could be fit where single bands are used to describe each Q^n species, however this resulted in bands with large full width half maximum (FWHM) values that are not necessarily representative of a single physical vibration [10]. Therefore, additional bands were needed to reduce the FWHM to achieve a more physically possible band shape. The FWHM and shape factor of the Pseudo-Voight band corresponding to each Q^n species was determined as described by Moulton et al. and kept constant across all glasses in both series [15]. The FWHM associated with Q^1, Q^2, and Q^3 species for binary barium silicate glasses with an oxygen to tetrahedron (O/T) ratio equal to 2.81 have been reported as 32.6, 51.1, and 66.3 cm^{-1} respectively [11]. Similarly, fitting of sodium metasilicate (O/T = 3) resulted in a FWHM of 35, 40, and 53.6 cm^{-1} for the same species mentioned above [9]. For the IGC and USG glasses, the FWHM of Q^1, Q^2, and Q^3 species were held constant at 50.5, 54.08, and 63.3 cm^{-1}, which is consistent with previously reported values. Although there has been discussion regarding the assignments of these additional bands in the literature [9, 10, 15-18], no specific assignments have assigned because of the convolution of modes in the quaternary system.

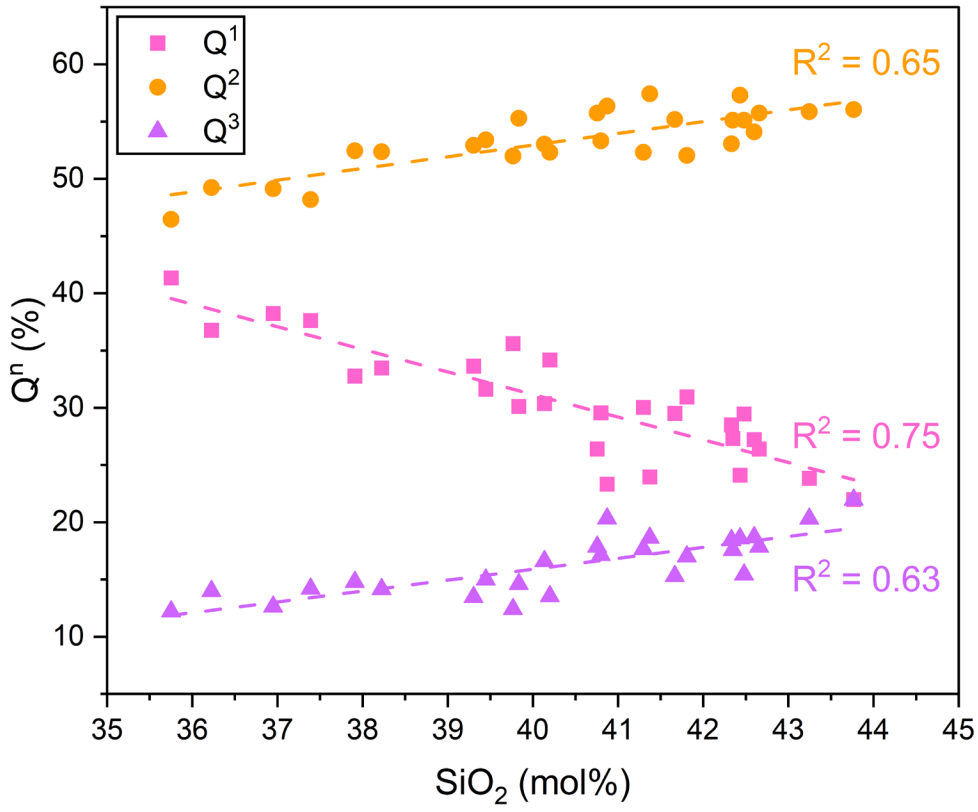

Figure 13: Composition dependence of the relative Raman activity of the different Q^n species for the IGC and USG glasses.

The resulting Q^n distribution from fitting each spectrum are presented in Figure 13 and Table 5. The results of both the IGC and USG glasses are combined in Figure 13 where it is seen that as the SiO_2 content of the glasses increases, the Q^2 + Q^3 concentration increases while the Q^1 population decreases, indicating an overall increase in connectivity of the system. This is unsurprising, as depolymerization of the network is expected as the modifier increases, which follows trends seen in binary alkali silicate glasses [19].

Alternatively, the Q^n distribution can be discussed in terms of the mean polymerization, also referred to as the O/T of the system (moles of oxygen per mols of tetrahedra). Experimentally, the O/T ratio is determined by the following:

$$O/T_{(\exp)} = 4(X_{Q^0}) + 3.5(X_{Q^1}) + 3(X_{Q^2}) + 2.5(X_{Q^3}) + 2(X_{Q^4}) \quad (9)$$

where X_{Q^n} is the molar fraction of a Q^n species experimentally determined by the Raman fitting multiplied by the stoichiometric oxygen associated with each unit [11]. When calculated from the target composition, the O/T is determined as the following:

$$O/T_{(nom)} = \frac{X_O}{X_{SiO_2} + 2 * X_{Al_2O_3}} \quad (10)$$

where X_O is the total moles of oxygen, and X_{SiO_2} and $X_{Al_2O_3}$ are the moles of SiO_2 and Al_2O_3 respectively. In compositions where SiO_2 is the only glass former, the Equation 10 denominator is simply the moles of SiO_2, however for the IGC and USG glasses the contribution of $[AlO_4]^-$ tetrahedra must be considered. Since the glasses all have low Al_2O_3 concentrations and high modifier content, all the target compositions are in the peralkaline regime (alkali/Al >1), where all Al^{3+} is assumed to be charge compensated to form $[AlO_4]^-$, and higher coordinated Al sites are not expected. As such, the model is adapted to incorporate the Al contribution.

By comparing the IGC and USG glasses to binary silicates, it is observed that the IGC and USG glasses are under-modified, i.e. there is a higher concentration of Q^2 and Q^3 units than expected for the composition. In binary M_2O and NO silicates, where M and N correspond to alkali and alkaline earth metals respectively, the target metasilicate (O/T = 3) composition occurs when the SiO_2 content is equal to 50 mol%. At this composition it is expected that Q^1 formation increases at the expense of both Q^2 and Q^3 species. One issue with this direct analogy is that it does not consider the contribution of Al_2O_3 in the system. Utilizing Equation 9, for the IGC glasses, the target metasilicate composition occurs at a silica concentration of 42.43 mol% (DOE 237) and at 40.14 mol% (DOE 1001) in the USC series.

Table 5: Q^n for IGC and USG glasses

Glass ID	$O/T_{(target)}$	$O/T_{(exp)}$	Q^1 (%)	Q^2 (%)	Q^3 (%)
DOE 12	2.87	3.11	36.78	49.24	13.98
DOE 45	2.92	3.10	33.48	52.36	14.16
DOE 210	2.96	3.04	26.4	55.75	17.85
DOE 237	3.00	3.03	24.11	57.3	18.59
DOE 322	2.90	3.15	41.35	46.45	12.20
DOE 347	2.96	3.05	27.32	55.11	17.57
DOE 360	2.93	3.08	31.61	53.4	14.99
DOE 414	3.11	3.07	29.51	55.19	15.3
DOE 596	3.18	3.10	34.17	52.31	13.52
DOE 1001	3.00	3.07	30.38	53.02	16.6
DOE1002	3.03	3.04	26.4	55.75	17.85
DOE1003	2.85	3.00	21.99	56.05	21.96
DOE1004	2.88	3.02	23.83	55.87	20.3
DOE1005	3.16	3.12	35.6	51.99	12.41
DOE 1006	2.96	3.06	29.56	53.32	17.12
DOE 1007	3.18	3.10	33.63	52.92	13.45
DOE 1008	2.81	3.03	23.95	57.42	18.63
DOE 1009	3.01	3.08	30.11	55.29	14.6
DOE 1010	2.84	3.02	23.33	56.35	20.32
DOE 1011	3.11	3.12	37.62	48.19	14.19
DOE 1012	3.13	3.13	38.24	49.13	12.63

Glass ID	$O/T_{(target)}$	$O/T_{(exp)}$	Q^1 (%)	Q^2 (%)	Q^3 (%)
DOE 1013	2.94	3.09	32.76	52.45	14.79
DOE 1014	2.94	3.06	30.03	52.32	17.65
DOE 1015	2.91	3.07	30.95	52.05	17
DOE 1016	2.89	3.05	28.51	53.06	18.43
DOE 1017	2.88	3.04	27.22	54.09	18.69
B2-Slag	3.08	3.07	29.46	55.12	15.42

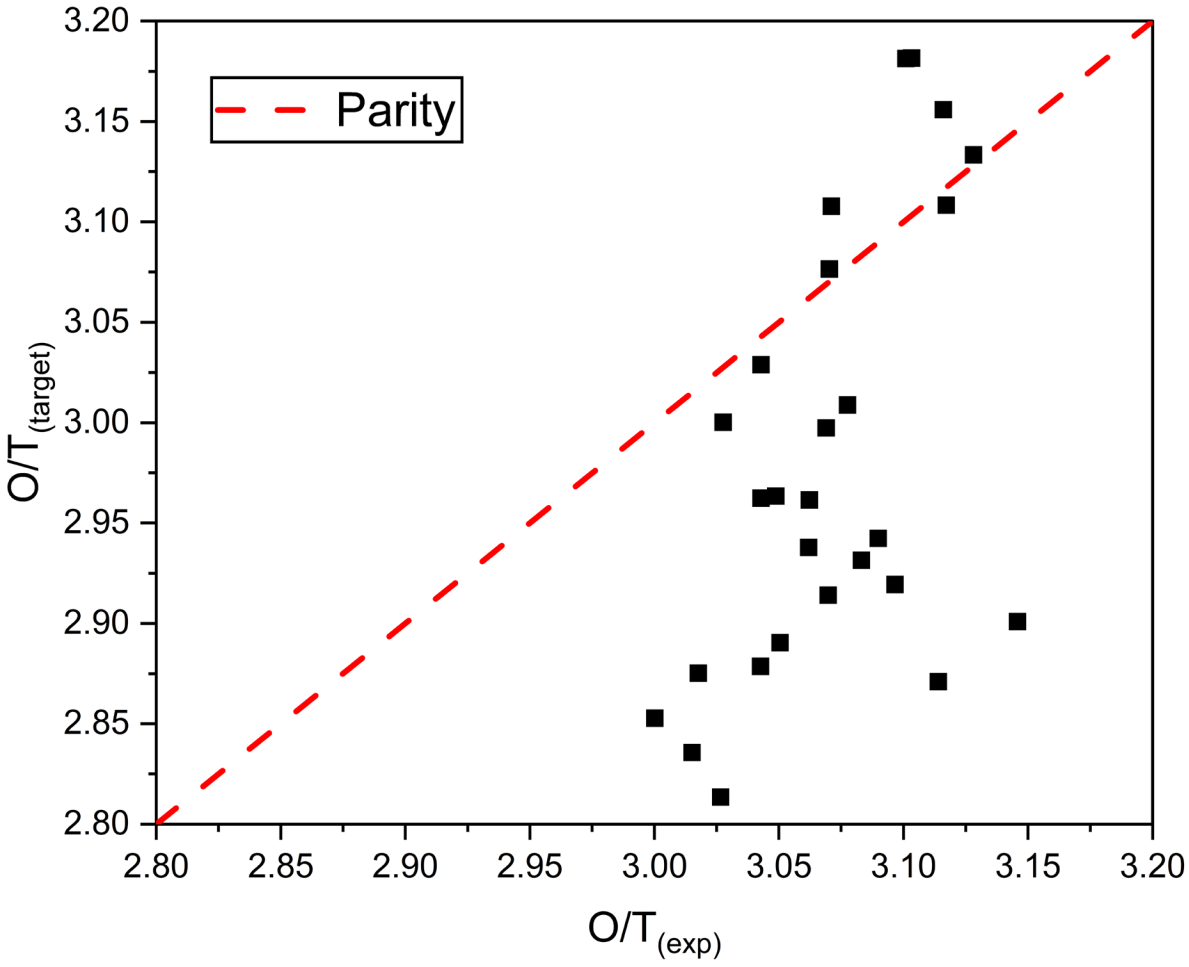

Figure 14: Comparison of the O/T calculated from the experimental Q^n speciation and target composition. Parity is represented by the red dashed line.

By comparing $O/T_{(exp)}$ to the $O/T_{(nom)}$, it is seen in Figure 14 that $O/T_{(nom)}$ results in a lower mean polymerization with an average deviation of ± 0.09. In other words, the mean polymerization calculated from the target composition predicts a higher degree of connectivity than what was

found from the Raman data. One interpretation for this difference is that the assumptions made in Equation 10 are not representative of the system. Conversely, the deviation could arise from the experimental composition significantly varying from thetarget composition. For the former, any contribution from [AlO_5] or [AlO_6] sites would reduce the total possible moles of Al_2O_3 available to form [AlO_4]$^-$ and would be reflected by adjusting the denominator of Equation 10. However, as stated before, these higher coordinated Al sites are unlikely. For the latter case, chemical analysis was performed on select glasses, where it was found that the experimental and target compositions were in reasonable agreement, refer to Table 6. Each experimental value was measured via inductively coupled plasma (ICP) analysis averaged over two measurements with an error of ± 10%. Alternatively, the difference in the mean polymerization could originate from the Q^n distribution obtained from the Raman spectra analysis.

Table 6: Target and Experimental Compositions

Glass ID	SiO_2 (wt%)	Al_2O_3 (wt%)	CaO (wt%)	MgO (wt%)
1003 (target)	45.50	9.00	35.00	10.50
1003 (avg. exp.)	45.56	8.19	36.09	10.16
1011 (target)	39.50	9.00	38.00	13.50
1011 (avg. Exp.)	39.86	8.35	39.48	12.31

Fitting of the Raman data was done through the interpretation of spectral features in combination with expected structures determined from the target composition. The 800 – 1200 cm^{-1} region of each spectrum was fit assuming that the only species present within the glass were Q^1, Q^2, and Q^3. The presence of Q^4, was neglected since there is little to no signal present at ~ 1250 cm^{-1} in any of the spectra. Conversely, even though signal is present where Q^0 is assigned, it is assumed that there is a negligible amount within the system based on the target compositions of the glasses. In comparison, it has been reported for binary CaO-SiO_2 glasses by both Raman and ^{29}Si magic-angle spinning nuclear magnetic resonance (MAS NMR) spectroscopies that the appearance of Q^0 does not show significant distinguishable features until the O/T ≥ 3.38 [20, 21]. The largest target O/T calculated for the IGC and USG glasses was 3.18 (DOE 596 and DOE 1007) making the presence of Q^0 unlikely. Additionally, the frequency difference between Q^0 and Q^1 is small, < 50 cm^{-1}, which would require a large portion of the Q^n distribution to be Q^0 to properly differentiate between the two. All the spectra in this study are broad, so it is assumed that any weak signal form Q^0 convolutes with the Q^1 signal, resulting in inhomogeneous broadening of the band which is best described by a Gaussian function. If this were the case, the resulting $O/T_{(exp)}$ would indicate a slightly higher degree of polymerization, which is not reflected in the reported $O/T_{(exp)}$ values.

Still focusing on the Q^1 signal, it is noted that the band is slightly broader than what is reported in the literature for binary glasses. This could be due to (i) the convolution of Q^0 and Q^1 signal (as discussed previously), or (ii) the contribution of Al_2O_3 in the system. The compositional dependence on the structure with the addition of Al_2O_3 is demonstrated in Figure 15, where the modifier content (MgO + CaO mol%) remains relatively unchanged in the system (within 1 mol%) and SiO_2 replaces Al_2O_3. The incorporation of Al_2O_3 causes the Al^{3+} and Si^{4+} to compete for the alkaline present, where Al^{3+} is preferentially charge compensated before the Si^{4+}. Ultimately, this results in the formation of Si-O-Al bonds which have a slightly lower bond strength and polarizability when compared to silica tetrahedra bonding together. The lower bond

strength causes the vibrational modes to shift to lower wavelengths, especially as more Al_2O_3 is added [22, 23]. In Figure 15, DOE 1013 has a higher mol% of Al_2O_3 than DOE 1002 which results in a significant shift in the Q^n envelope to lower wavelengths. This likely occurs because signal from $[SiO_4]^-$ tetrahedra and Si-O-Al converge, resulting in a broadening of the signal associated with Q^1. As such, as Al_2O_3 mol% increases, the Q^1 contribution is artificially increased, leading to a higher O/T, indicating a more depolymerized system than expected. Results of the Q^n distribution can be directly correlated with physical glass properties and cementitious reactivity.

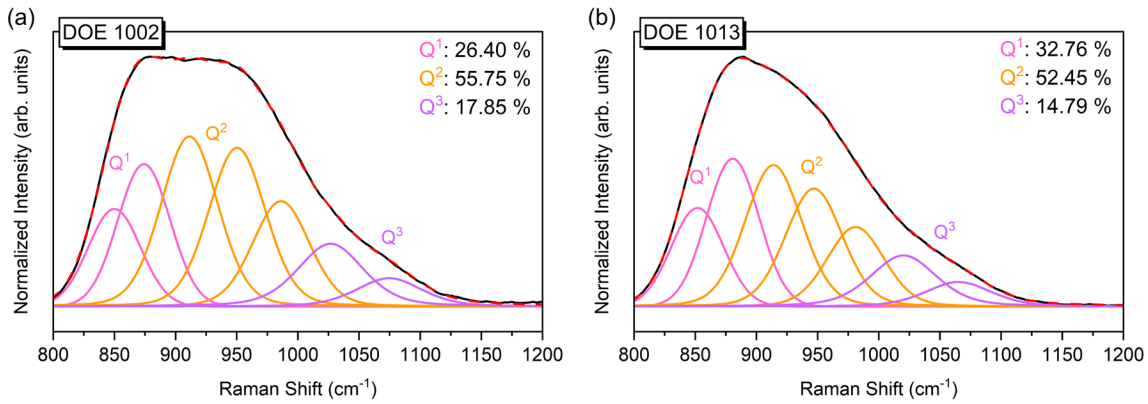

Figure 15: Raman fitting of (a) DOE 1002, and (b) DOE 1013 using a pseudo-Voight line shape.

4.3 Differential Scanning Calorimetry

DSC was used to determine various temperature-dependent properties of the IGC and USG glasses. In particular, we were interested in the glass transition temperature (T_g), crystallization temperatures (T_x), and liquidus temperatures (T_l). These data are important for several reasons related to the sparseness of the data in these glass compositional regions, which were required for the predictive modeling that is needed for foaming process strategies. The DSC data are given in Table 7. The graphs of these DSC measurements can be found in the Appendix D section of this report.

Table 7: The results of the DSC measurements for the IGC and USG glasses. The heating rate for these measurements was (10 K/min)

DOE	$T_g \pm 2$ (°C)	$T_x \pm 2$ (°C)	$\Delta T_s = T_x - T_g$ °C)	$T_l \pm 2$ (°C)	$\rho \pm 0.01$ (g/cm^3)	V_m (cm^3/mol)	C_g	Λ^{th}
12	762	916	154	1416	2.92	20.34	0.5258	0.683
45	752	813	161	1382	2.92	20.04	0.5274	0.679
210	754	902	148	1377	2.93	19.75	0.5302	0.674
237	752	911	159	1387	2.92	19.60	0.5303	0.671

DOE	$T_g \pm 2$ (°C)	$T_x \pm 2$ (°C)	$\Delta T_s = T_x - T_g$ °C)	$T_l \pm 2$ (°C)	$\rho \pm 0.01$ (g/cm^3)	V_m (cm^3/mol)	C_g	Λ^{th}
322	778	910	132	1440	2.93	20.48	0.5242	0.687
347	761	890	129	1341	2.91	20.05	0.5274	0.671
360	768	918	150	1350	2.92	20.27	0.5259	0.678
414	752	915	163	1452	2.93	19.38	0.5308	0.678
596	756	892	136	1406	2.94	19.31	0.5301	0.685
1001	746	924	178	1368	2.92	19.49	0.5301	0.676
1002	744	915	171	1444	2.91	19.34	0.5308	0.670
1003	746	943	197	1336	2.89	20.01	0.5283	0.660
1004	742	945	203	1331	2.89	19.79	0.5288	0.661
1005	743	905	162	1405	2.94	19.14	0.5308	0.684
1006	746	903	157	1376	2.91	19.80	0.5283	0.674
1007	744	896	152	1401	2.94	18.88	0.5327	0.685
1008	750	963	213	1339	2.90	20.18	0.5282	0.664
1009	742	923	181	1385	2.92	19.30	0.5310	0.676
1010	744	947	203	1335	2.90	19.91	0.5298	0.666
1011	749	880	131	1396	2.94	19.35	0.5293	0.689
1012	744	885	141	1388	2.94	19.15	0.5296	0.690
1013	748	925	177	1373	2.92	19.75	0.5284	0.680
1014	754	921	167	1359	2.92	19.99	0.5287	0.672
1015	772	933	161	1323	2.92	20.24	0.5278	0.671
1016	782	929	147	1351	2.93	20.43	0.5287	0.670
1017	789	920	131	1374	2.91	20.70	0.5247	0.669
B2	763	914	151	1374	2.93	19.78	0.5288	0.676

One important observation from the DSC measurements is that the T_g is, on average, approximately 200 °C higher than the T_g for soda lime silicate glass. The effect this temperature difference has on processability, and foaming will be discussed in a later section.

4.4 Crystallization/X-ray Diffraction

Given the instability of the initial IGC glasses in terms of crystallization, we initially performed multiple crystallization and XRD analyses to determine what crystals were forming in these invert glass systems. Crystallization can affect our planned processes in several ways:

1. Excessive crystallization will lower the amount of glass in the system which will negatively impact foamability.
2. Crystallization temperatures, T_x in DSC, that fall within the foaming window will cause the glass to crystallize during ECM synthesis. Depending on the phases that form, the physical and chemical properties of the ECM could change sufficiently to render the material unsuitable for its intended application.
3. In our case, crystallization during the foaming process could lessen or eliminate the cementitious reactivity of the ECM material.

To determine the phase of the crystals that would form in the IGC glasses, we subjected samples of several IGC glasses to various heat treatments, and then used XRD to identify the resulting crystalline phases. The heat treatments consisted of maintaining approximately 10 grams of shards from four of the IGC glasses near the T_x identified by DSC for three hours.

The results of these analyses are shown in Figure 16. The most prevalent mineral phases that were observed were akermanite ($Ca_2MgSi_2O_7$) or merwinite ($Ca_3MgSi_2O_8$). We should note that neither of these phases are expected to be cementitious, even in the high molarity and pH solutions associated with LAW.

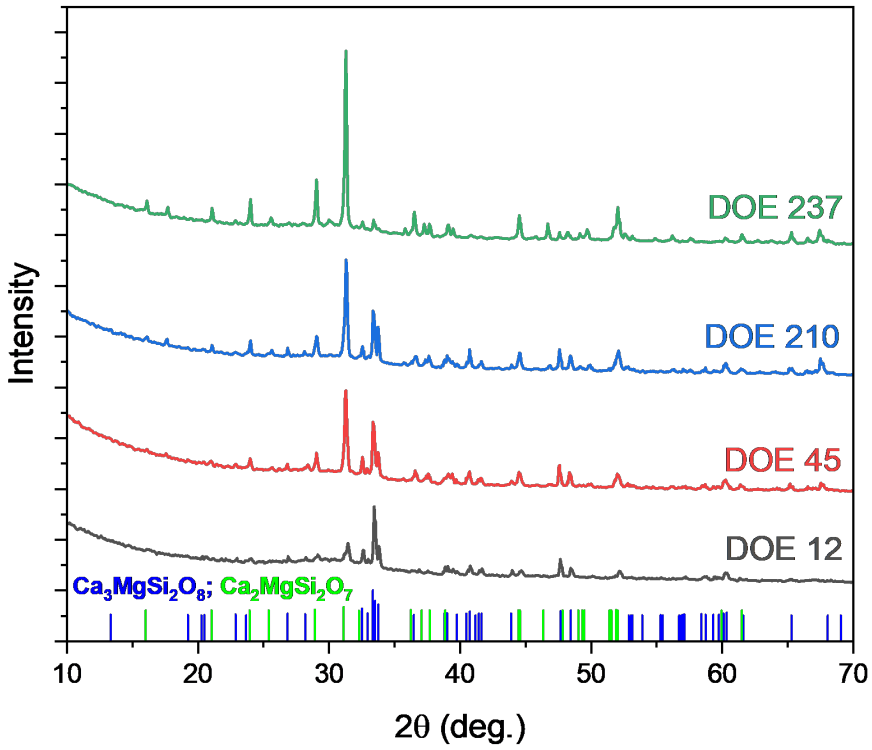

Figure 16: XRD of four IGC glasses that were initially stable during the pour and then heat treated near T_x to induce crystallization. Two major phases were observed to form: akermanite and merwinite.

Interestingly, these phases, along with phases observed in the more unstable, crystallized glasses, are the same minerals that are present in unquenched blast furnace slag. We surmise this is a result of the similarity between the composition of the IGCs and the liquid slag phase during steel making.

One of the most important aspects of our work is to control the mineralogy of the ECMs that will be synthesized from the glass or glassy materials that we incorporate into the foam batches. The primary mechanism by which we initially control the mineralogy is via the batch composition. In the instance of the IGCs and USGs, we are optimizing between processability and cementitious reactivity, and often, this leads to compromises in one or more properties to have a technologically sound and industrially scalable product.

5. Foaming of IGC/USG Glasses

In year one, the team was mostly relying on trial and error experimentation in terms of foaming the IGC and USG glasses. One of the largest differences between the IGC/USG glasses and the materials we have traditionally used for foaming is the high T_g and viscosity of our novel compositions. Compared to soda lime silicate, for example, the IGC/USG compositions have a T_g that is approximately 200 °C higher. Additionally, we tried to foam in a specific viscosity range for a given glass composition – similar to the T_g, where this foaming temperature is significantly higher for the IGC/USG compositions.

To improve the foamability of the compositions, we may use additives to lower the temperature ranges. We will discuss the details of these additives and their effects on various glass/ECM properties in a later document.

By decreasing the viscosity and the T_g of the melt using additives, we were able to successfully produce a foam at the end of Year 1, that demonstrated sufficient properties to be used as a baseline composition for further work.

6. Cementitious Reactivity

In Phase 1 of this program, we used isothermal calorimetry (ITC) to measure the cementitious reactivity of the both the IGC and USG compositions, as well as some foamed materials that were created in previous tasks. The ITC experiments measured the heat released when the various materials we have created were placed in contact with simulated Hanford waste solutions and underwent hydration reactions similar to the reaction of OPC and water in normal cement applications.

The salt simulant was prepared in a large batch of four liters prior to starting the ITC measurements. The composition of the salt simulant is given in Table 8.

Table 8: Target composition of the simulated salt waste solution used in the cementitious reactivity experiments[24].

Component	Adjusted 5M Na Conc (M)
Al	0.300
K	0.035
Na	5.000
Cl	0.041
F	0.032
PO_4	0.049
SO_4	0.087
NO_2	0.564
NO_3	1.620
CO_3	0.277
OH	1.564
TOC	0.077

All isothermal calorimetry measurements were conducted in TAM Air 2 (TA Instruments) calorimeters. The calorimeters were held at 26 °C to ensure the instruments were always above the ambient room temperature as they can heat but not actively cool.

All ITC experiments were conducted using approximately 7 grams of material with a water-to-solid ratio of 0.5. In the case of the salt simulant solution, we had to account for the presence of

the dissolved solids when determining the amount of solution to add, which yielded a volume of approximately 3.9 mL for all experiments.

6.1 Cementitious Reactivity of IGC Glasses

The initial reactivity measurements were conducted on the “as-prepared” IGC glasses. The glasses were crushed to produce a mean particle size that was approximately equivalent to that of slag as it is well-known that particle size will affect the kinetics of hydration for cementitious materials. The particle size distribution of the IGC glasses is shown in Figure 17.

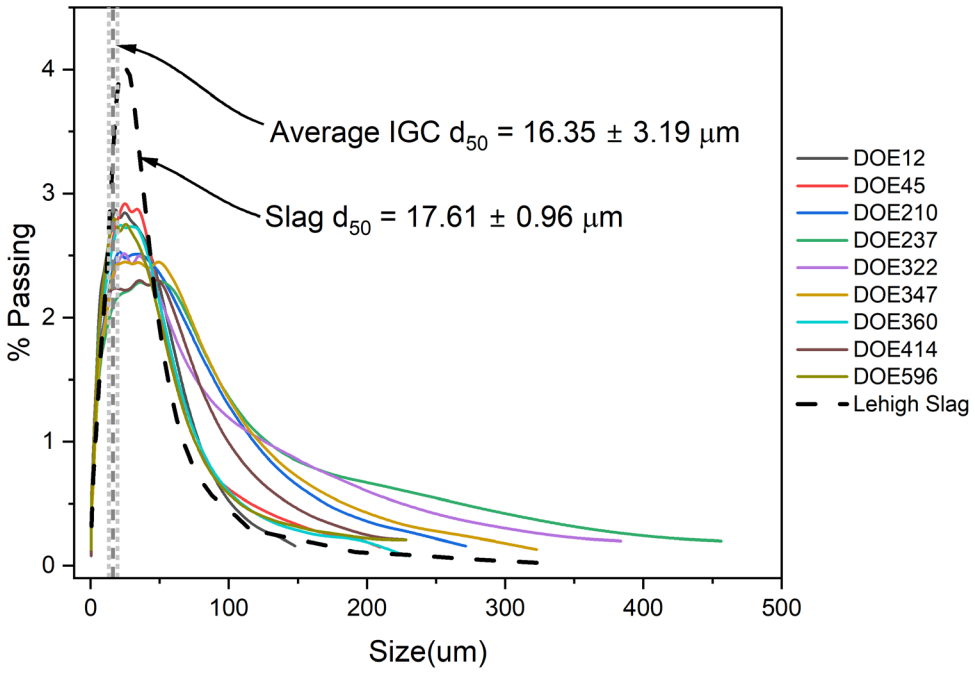

Figure 17: Particle size distributions of the IGC glasses. The dotted lines show the average d_{50} for the 9 glasses along with the standard deviation. The PSD of a reference slag is also shown for comparison.

The distributions of the IGC glasses relative to slag were somewhat different, but the d_{50} values for the IGC glasses were sufficiently close to that of slag to proceed with the measurements. Collecting these data also provides an opportunity to correct measurements for these small differences should we observe anomalistic data with no other valid explanations.

The ITC results for the nine IGC glasses are shown in Figure 18 along with the data for our reference BFS for comparison.

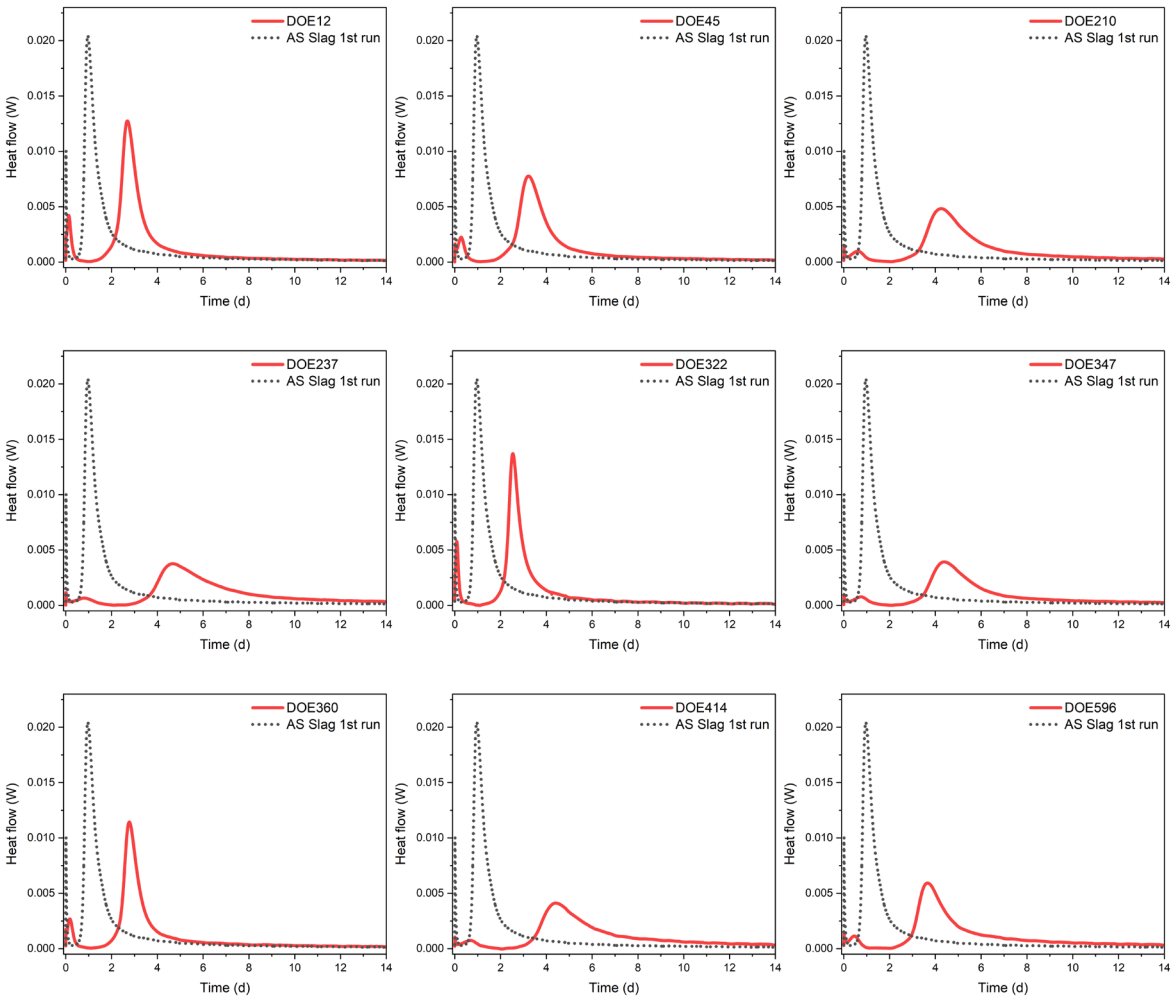

Figure 18: ITC data from the original 9 IGC glasses along with that of a reference BFS for comparison.

Inspection of Figure 18 reveals that all of the glasses showed cementitious reactivity in the simulated waste form scenario. The two glasses that showed the highest peak heat flow and fastest hydration kinetics were DOE12 and DOE322. Here we will define a term, “peak time”, which corresponds to the time at which the maximum heat flow occurs. While not wholly descriptive of the hydration kinetics, we will use this term as a metric of how quickly a given glass composition is reacting with the simulated LAW solution.

The λ ratio of these glasses were 0.95 and 0.99, respectively. We had anticipated that the cementitious reactivity properties would be strongly correlated with the λ ratio; however, inspection of the compositions compared to the peak heat flow and peak time (Figure 19) provides us with evidence that this is not the case.

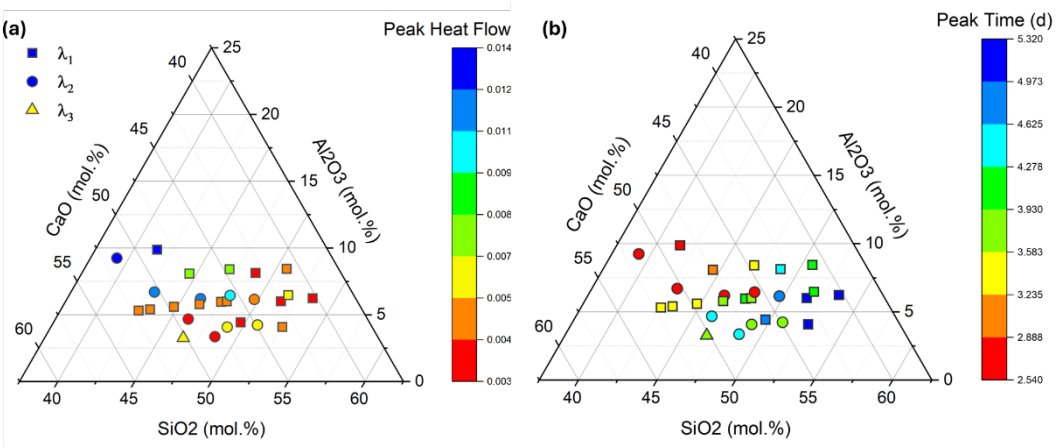

Figure 19: A comparison of the glass composition to the peak heat flow or peak reaction time demonstrates that there is no ostensibly strong correlation between these cementitious properties and the glass composition. The ternaries also contain measurement data for the USG glasses as well.

The results of the USG ITC measurements are shown in Figure 20.

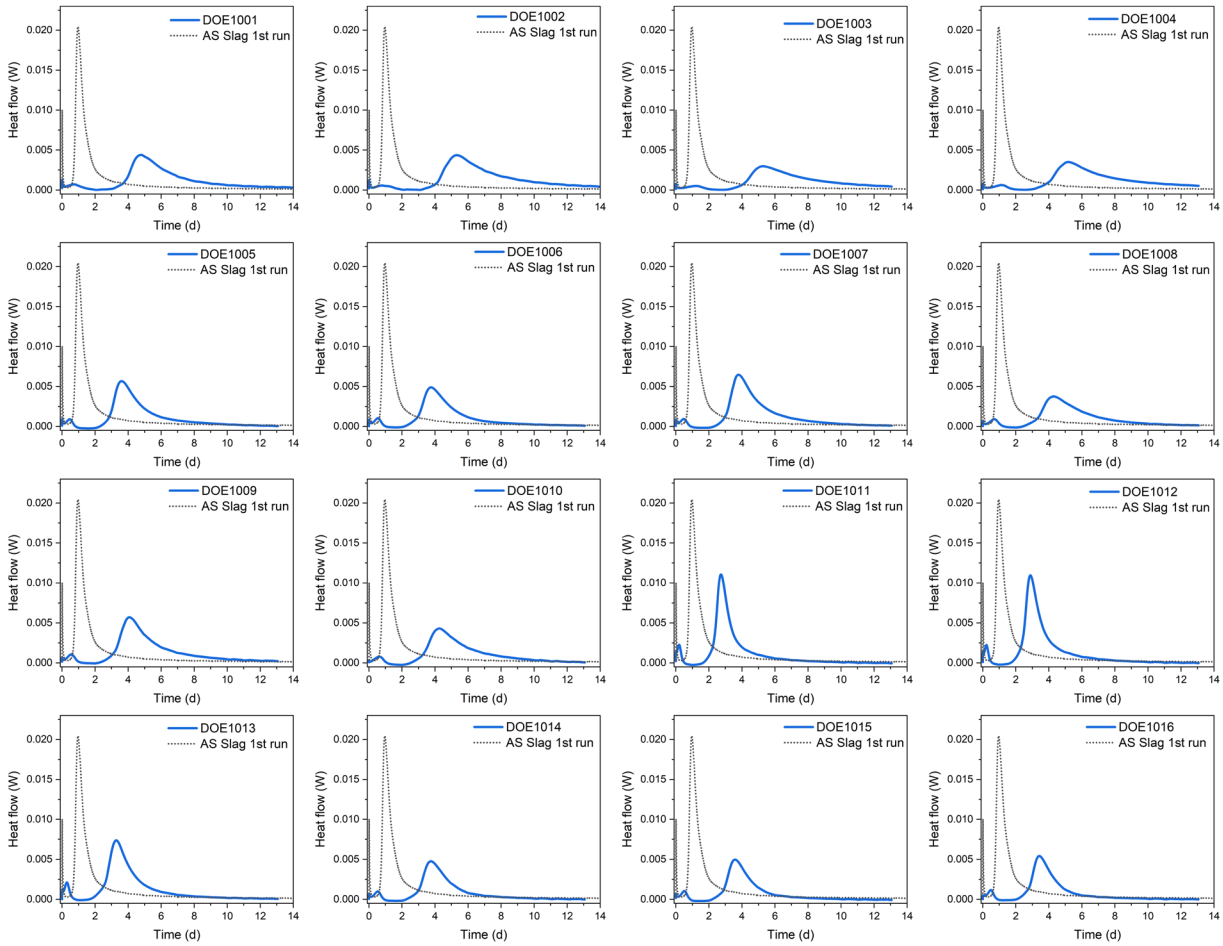

Figure 20: Results of the ITC measurements for the USG glasses.

Some of the USG compositions performed similarly well relative to the IGC compositions – in particular, DOE1011 and DOE1012 had peak heat flows and peak times that were comparable to the DOE322 and DOE12.

We are also using cumulative heat generated to compare the various compositions we designed to standard, known cementitious materials in LAW solutions, such as BFS. The total heat for the IGC glasses is shown in Figure 21. Many of the IGC glasses had a comparable heat generation to BFS, and all the glass compositions generated sufficient hydration reactions to have solidified the simulant when the ITC ampoules were removed from the calorimeter.

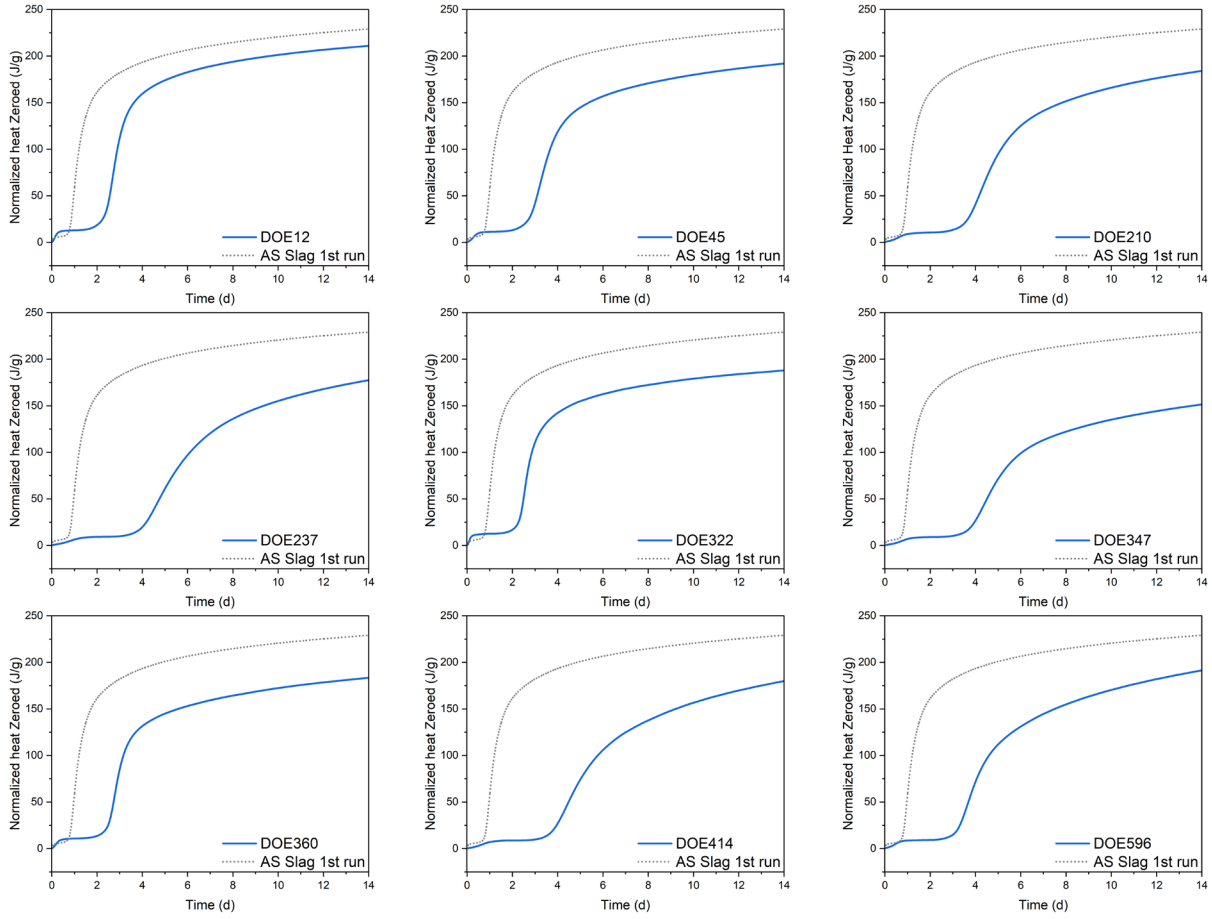

Figure 21: Cumulative heat generated over the course of the experimental duration for the IGC glasses in contact with the LAW simulant. The cumulative heat generation for BFS is shown by the dashed line.

The cumulative heat generation for the USG glasses is shown in Figure 22. Again, these glasses demonstrated clear heat release associated with cementitious reactions, and the products were completely solidified when their respective ampoules were removed from the ITC.

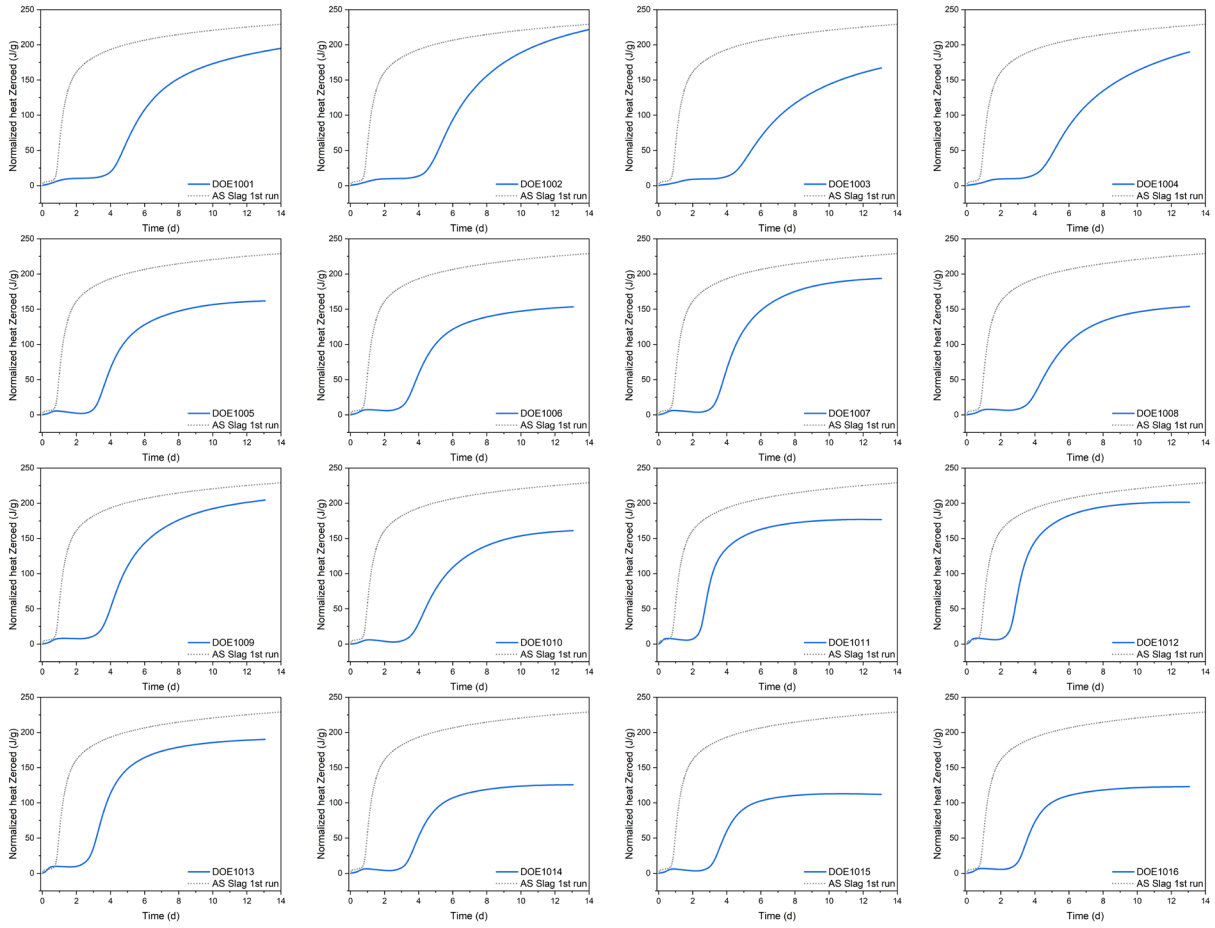

Figure 22: The cumulative heat generation for the USG compositions relative to that of BFS (dashed line).

Interestingly, one of the glasses, DOE1002, generated nearly as much heat over the course of the experiment as the BFS material we used for a control. However, the reaction of DOE1002 with the simulated LAW solution proceeded much more slowly than the BFS hydration reaction.

We also inspected correlations between the isothermal calorimetry measurements and the glass structural measurements made via Raman spectroscopy. Cement hydration, in general, can be thought of as a dissolution/precipitation reaction that is similar to what occurs in glass corrosion, especially when silicate glasses are in contact with high pH (pH > 12) solutions. As such, we hypothesized that the structural configuration of the IGC/USG glasses would have some correlation with their cementitious properties.

We first investigated this by plotting the various speciations measured by Raman spectroscopy (i.e., Q^1, Q^2, and Q^3) with two previously defined cementitious properties: peak heat flow and peak time. The results of the correlations indicated that Q^1 is positively correlated with peak heat flow and negatively correlated with peak time – these results are shown in Figure 23a and Figure 23b, respectively. These correlations are consistent with the hypothesis that increased disorder in the glass (i.e., higher Q^1) will lead to increased reactivity (i.e., higher peak heat flow at lower peak times).

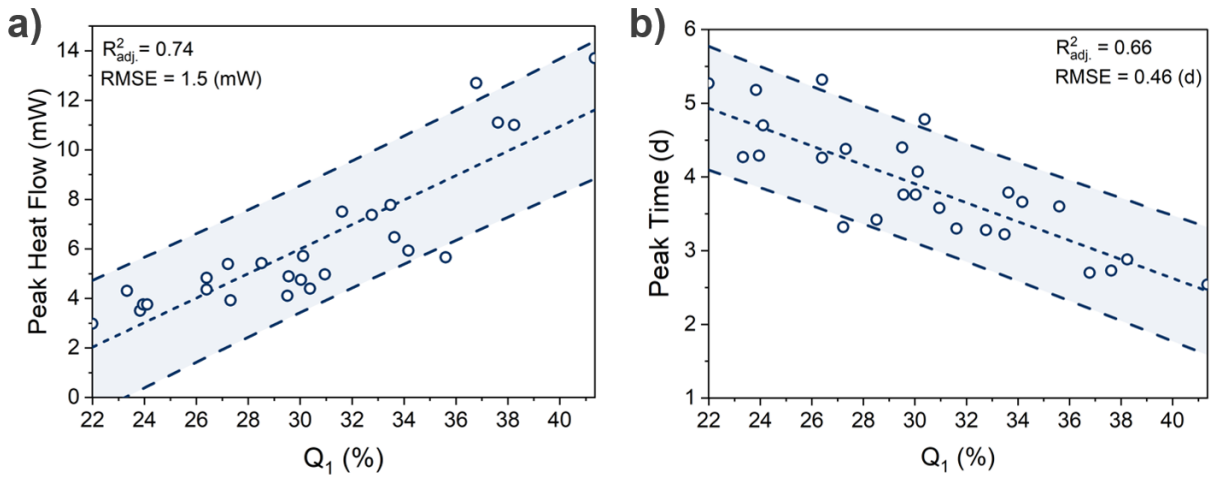

Figure 23: Correlation between peak heat flow and Q^1 concentration (a) indicating increased disorder causes higher peak heat flow, and (b) the correlation between peak time and Q^1 showing that increased disorder leads to faster hydration kinetics (Shaded interval is at 90% prediction confidence).

We can further demonstrate these related effects by considering other species in the development of the correlations – we discovered the strongest correlation between glass structure and cementitious properties occurs when we fit the ratio of Q^1/Q^2 to the measured reactivity properties as shown in Figure 24a and Figure 24b.

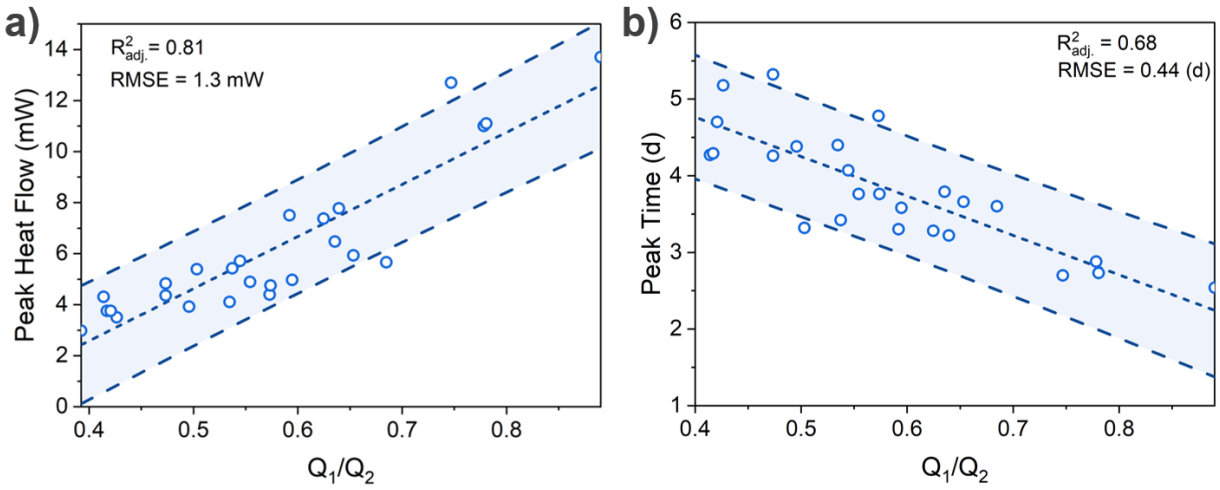

Figure 24: Correlation between the ratio of glass structural descriptors, Q^1 and Q^2, with (a) the peak heat flow and (b) the peak time (Shaded interval is at 90% prediction confidence).

These types of correlations will be used to develop predictive modeling that relies solely on a prior knowledge to determine a system's cementitious reactivity. As the project progresses into Year 2/Phase 2, we will need to rely on such models to reduce the number of experiments required to determine a given batch formulation's cementitious reactivity. This experimental reduction will becoming increasingly valuable as we start to incorporate sustainable materials into the ECM batches.

7. Predictive Modeling

Predictive modeling of the properties of the glass forming systems within this report was used to expedite the development of new glasses that can be foamed. To do this, the foaming window of the glasses must be determined. This is done by considering the temperature dependent variables associated with creating a foam glass such as sintering, bubble formation, secondary fining and viscosity. Additional variables that are kept constant include particle size, heat rate, sample size, and concentration of foaming agent.

Using statistical mechanics to predict the proportion of glass forming species (Q^n, AlO_4), and topological constraint theory to predict the fragility based on the structure, it is possible to determine the projected viscosities of the glass. From the predicted viscosity curves of the IGC and USG glasses, it was possible to anticipate the required melting temperature of each composition, mitigating a trial-and-error period during the initial melting of the glass. Additionally, glass formability information acquired in the fabrication of the IGCs was then used to help predict the probability of future compositions (such as the USG glasses) forming a glass.

Figure 25 shows the parity plot of select IGC and USG viscosities obtained experimentally and through modeling. Data points obtained from the model relied on predicted structures and data available in the literature. As seen in the parity plot, the modeled and predicted data were in reasonable agreement with each other, with the modeled data consistently predicting slightly higher temperatures than the experimental data. In Phase 2, as experimental structural and viscosity data is introduced, the model accuracy should show improvements.

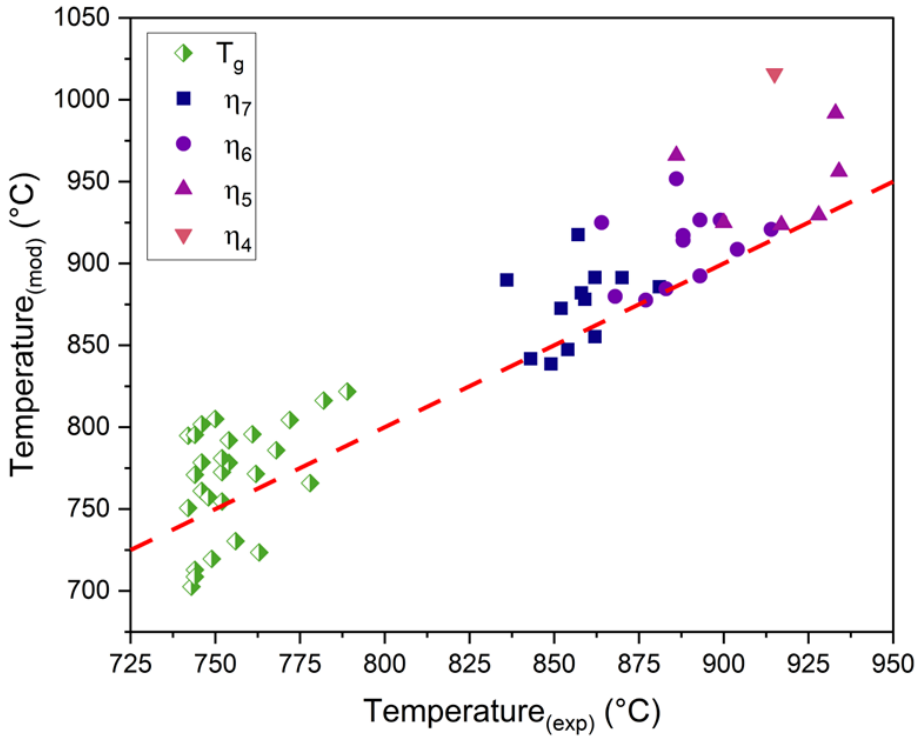

Figure 25: Parity plot of the model and experimental viscosities of the IGC and USG glasses.

Using the modeled viscosity data, it was possible to determine the probability of a glass to form a foam via the prediction of the glass foaming window. This was done by considering the relationship between gas escape (produced by the foaming agent) and the sintering time of the glass. If the release of gas occurs at a faster rate than the sintering time, the escaping gas becomes trapped within the fluid, allowing pores to form. Conversely, if the gas release is slower than the sintering time, the gas escapes without creating pores. Figure 26 illustrates the predicted foaming region of soda-lime silicate and DOE 322 using SiC as the foaming agent.

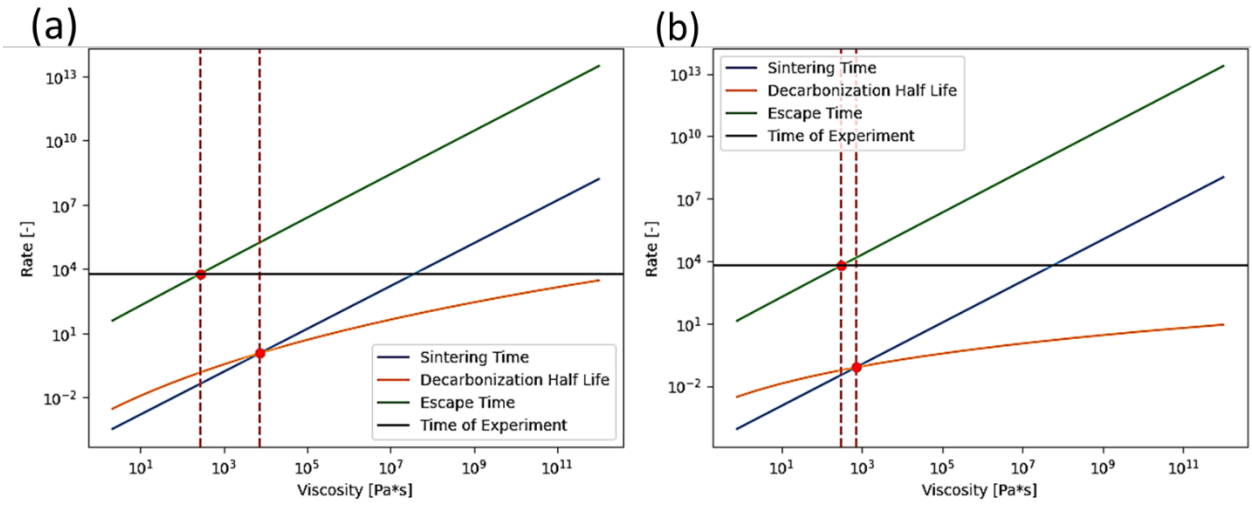

Figure 26: An illustration of the predicted foaming region for (a) green soda-lime silicate bottle glass, and (b) DOE 322 with SiC as a foaming agent.

Consequently, it was found that the foaming window of the IGC and USG glasses is very narrow, spanning ~ 10 °C for each composition, compared to the nearly 170 °C range of SLS glass. The challenge of a small foaming window, is that although it is possible to obtain the desired foaming temperature range on the lab scale, maintaining a narrow temperature range in an industrial process is not feasible. In addition to the IGC and USG glasses all being invert aluminosilicate glasses, it was also found that all the compositions had a higher surface tension (via modeling) and a higher viscosity (via modeling and DSC) when compared to SLS. As such, for the next iteration of glasses, it was desirable to decrease the surface tension and viscosity of the glasses. This was achieved through the addition of boron oxide and potassium oxide to the compositions. By introducing these oxides to the model and down selecting compositions based on desirable foaming properties, it was possible to identify glass compositions that would not only be able to create a foam with the use of $CaCO_3$ as the foaming agent, but also react cementitiously when introduced to the simulated salt solution.

8. Historical Slag Analyses

We have begun to inspect historical grout-based samples as a means of delineating the nature of slag dissolution under simulated salt-waste conditions. We have primarily investigated these samples utilizing scanning electron microscopy (SEM) coupled with energy-dispersive X-ray spectroscopy (EDS). There are many reasons to undertake such analyses that are presently being developed as part of the team's intellectual property – as such, they will not be discussed here.

Figure 27 is an image of one of these measurements conducted on a 15-year-old Cast Stone material. Spectrum 1 in the image was taken from the bulk area of a slag particle. Spectrum 2 was taken from a dissolution “rind” region that is observed around nearly all the slag particles shown in the SEM/EDS image. Spectrum 3 was taken in the surrounding cementitious matrix.

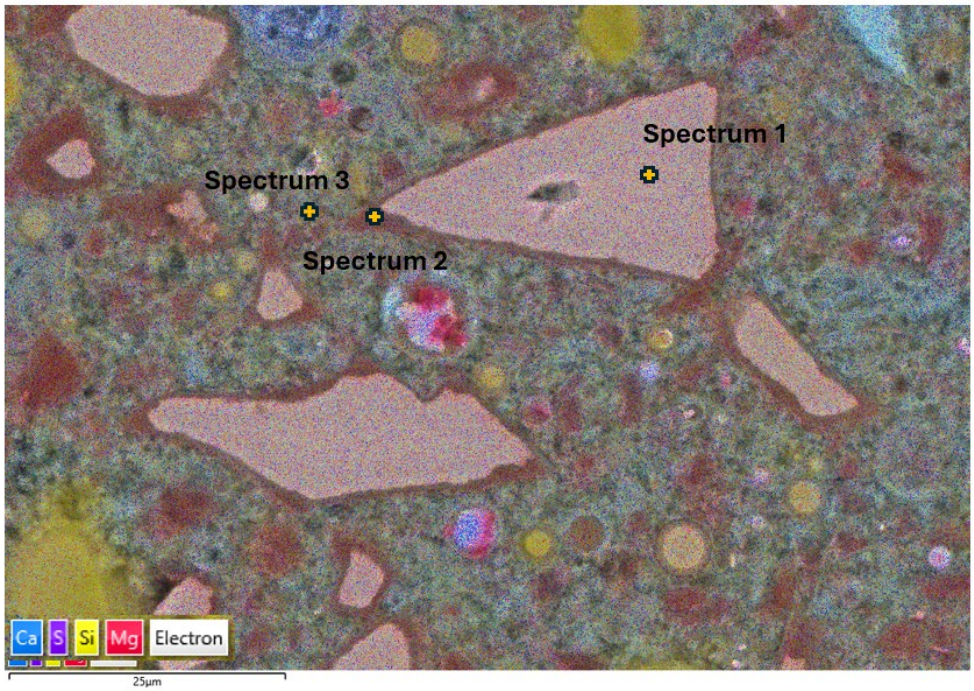

Figure 27: SEM/EDS image of a cross-section from a 15-year old Cast Stone sample showing the dissolution of slag particles (light pinkish particles with darker rinds – Spectrum 1 and Spectrum 2, respectively) within the cementing matrix.

The results of the EDS are shown in Table 9.

Table 9: Elemental EDS analysis of the spectra shown in Figure 27. All values are in wt.%.

	Inside Particle		Particle Transition Zone (“Rind”)		Away from Particle	
Element	Spectrum #1	Spectrum #1 Normalized	Spectrum #2	Spectrum #2 Normalized	Spectrum #3	Spectrum #3 Normalized
Ca	25.8	43.9	7.0	22.2	15.6	41.4
Si	19.2	32.7	11.5	36.4	12.5	33.2
Mg	7.1	12.1	6.6	20.9	3.9	10.3
Al	5.6	9.5	5.5	17.4	5.3	14.1
S	1.1	1.9	1.0	3.2	0.4	1.1

The EDS analysis reveals that the rind is depleted in Ca relative to the bulk particle, but the amount of Si (normalized) is consistent with the bulk. Additionally, we did not observe a significant difference between the stoichiometry of the bulk particle and the surrounding cementitious matrix. The rind also appears to be “enriched” in Mg, Al, and S relative to the other regions. The mechanisms responsible for these observations will be delineated in future studies.

9. Industrial Scalability Index

The industrial scalability index (ISI) is a tool that serves as a system of “checks and balances” for the technology being developed at the lab scale. Essentially, we use the ISI to ensure that our solutions are feasible from a practical and economic standpoint. In other words, we could easily develop a system that achieves the desired goal in a very short period of time; however, the industrial-scale implementation of that technology would likely be cost or time-prohibitive.

Given that the major crux of the work in Year 1 was to develop an ideal glass composition that would be synthesized from raw, virgin materials and then processed into foams, the ISI factorization started with that concept. We looked at two possibilities:

1. Utilize specialty glass manufacturers to produce large quantities of our ideal glass which would then be transferred to a facility for foam synthesis – this would be similar to the way frit is produced and handled at the Defense Waste Processing Facility (DWPF) at SRS.
2. Construct and operate a specialty glass melting facility that produces the IGC on the front end of the foaming plant.

It is important to note that both options are the most economically conservative models we can envision where virgin glass forming chemicals are used; whereas our final solution will incorporate a fraction of sustainable materials such as, recycled container glass or industrial glass, coal ash, waste to energy ash?, etc.

Option 1 Details: We initially contacted two specialty glass manufacturers to get an estimate of the expense for producing glass and then shipping it to or near the Hanford Site for foaming. The two independent, US-based manufacturers we contacted were: Bekeson Glass, LLC and Specialty Glass, LLC. The parameters for the glass quote were 15,000 Tons Per Year (TPY) pre-sized to a particle size distribution of less than 150 μm, which is a baseline particle size range for ECM synthesis. The most competitive cost estimate from these two manufacturers was given at $2.50-$3.00 per pound. This range equates to $75M/yr-$90M/yr.

Option 2 Details: The second option is to construct a glass melting facility that would produce the tailored glass compositions on the front-end of the ECM synthesis. Given the present variability in the compositional space, our efforts have been focused on generating a “rough order of magnitude (ROM)” estimate. We approached several glass melter manufacturers and engaged in multiple conversations to develop the ROM for an integrated facility that has flexible cooling capabilities (for quenching the glass) and is capable of being couple to an “ECM-ready” process. The estimates below give the capital equipment expense for two such facilities – again, it is important to point out these are ROM estimates:

ROM 1 – Production capability: 20,000 TPY = $15M-$25M
ROM 2 – Production capability: 20,000 TPY to 60,000 TPY = $25M-$60M

Based on these initial estimates, we currently envision the most cost-effective facility would be one that incorporates a glass melter to produce an IGC that is coupled to the front end of the ECM synthesis facility.

A typical single ECM kiln can produce approximately 15,000 TPY of foamed product. If we assume that the density of the material will be anywhere from 0.6 g/cm^3 to 0.8 g/cm^3, this equates to approximately 2.25M to 3M gal/yr of LAW that could be stabilized from a single kiln.

Given the present uncertainty in the final recipe as well as cooling strategies for producing the IGC, it is difficult to project a reasonable ROM for the cost per gallon of waste treated at this time. However, as we expand the feedstock materials in Phase 2, we will work to hone a cost per gallon of waste treated estimated based on the most current processing strategies.

10. Go/No-go Milestone Completion

Per our proposed schedule, our team had a go/no-go milestone near the end of Year 1. The proposed milestone was:

"The major deliverable in Phase 1 is the production of one or more ECM materials based on the IGC that are cementitiously reactive in the presence of simulated LAW streams. Go/No-Go decision: has the team successfully produced an ECM material that is cementitiously reactive with LAW-based waste streams?"

The SRNL team accomplished this milestone by 1) designing a series of glasses that mimicked the chemical and mineralogical properties of various cementitious premix materials, 2) developing strategies by which these glasses could be processed into ECMs, and 3) observation and measurement of these materials' cementitious reactivity when in contact with simulated low-activity waste.

To that end, we designed a glass composition that can foamed into an advanced ECM (AECM). The glass was then crushed and thermally processed to create the AECM. Approximately 7 g of the AECM material was crushed into a fine powder, D_{50} ~ 10-20 µm, and another 7 grams of the material was crushed to approximately 1-3 mm in size. Each size fraction of the ECM was then put into contact with 3.9 g of simulated Hanford LAW solution (~50% waste loading) and placed in a TAM Air isothermal calorimeter to measure the heat released during any potential cementitious reactions that may occur between the AECM and the simulated LAW. The results of this measurement are shown in Figure 28 for each size fraction. For comparison, the heat released from a literature-reference geopolymer [25] is also shown. Upon removing the sample vials from the isothermal calorimeter, we observed no free-standing liquid in the sample containers – only solid products remained in the vials.

In addition to the isothermal calorimetry data, we have observed "before and after" images of the AECM material from the isothermal calorimetry sample vial that provide further evidence of cementitious reactivity via scanning electron microscopy. The images are shown in a collage form in Figure 29. Inspection of Figure 29A shows the visual characteristics of an open-cell AECM with variable pore size distribution. As we imaged a similar section of this AECM after contact with LAW simulant, we observed that the pore structure was no longer visible but rather appeared to be closed-off by a secondary phase(s) (Figure 29B, Figure 29D). Higher magnification of the "After Salt Simulant Contact" piece of AECM revealed the presence of "wispy-looking" secondary phases that are indicative of calcium-silicate-hydrate minerals, which confirms that cementitious reactions had occurred between the AECMs and the salt simulant (Figure 29F, Figure 29H).

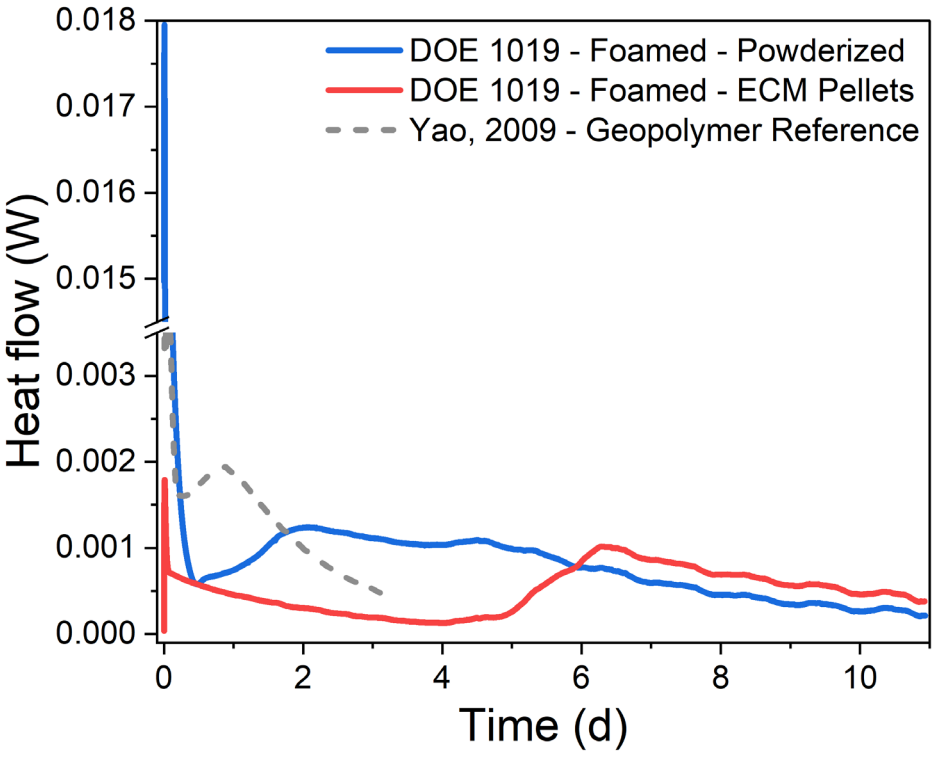

Figure 28: Heat flow measurements from AECM materials in contact with simulated LAW solution along with reference data from a geopolymer specimen[25] showing the heat generated from the AECM materials is analogous to geopolymer formation.

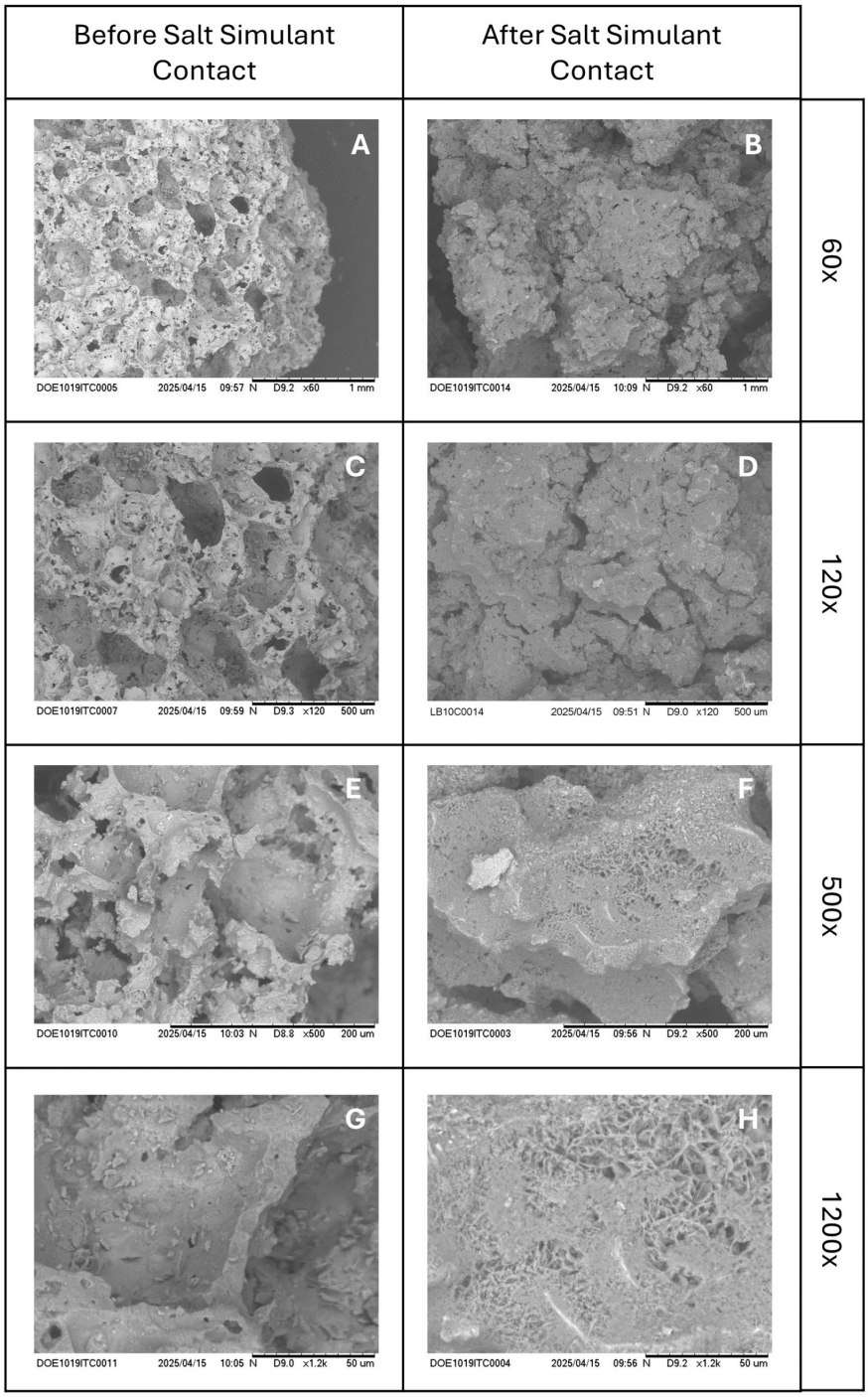

Figure 29: SEM collage showing the visual differences between unreacted AECMs (left column) and AECMs that were in contact with simulated LAW (right column). The images in the left column show the open pore structure prior to contacting the salt solution, and the images in the right column show that the pores have been closed after approximately 12 days of contact. At higher magnification (subfigures F,H), secondary mineral phases that have the appearance of calcium silicate hydrate are visible.

11. Summary

The work completed in year 1 culminated in the completion of the Year 1 go/no-go milestone for creating a cementitious ECM that reacts with a simulated low-activity waste solution to form cementitious mineral phases. We achieved this goal through the following tasks:

1. Design and synthesis of glasses that mimic the chemical and mineralogical properties of grout waste form premix components.
2. Characterizing these glasses via several methods including viscometry, Raman spectroscopy, XRD, differential scanning calorimetry and isothermal calorimetry.
3. Using this data to develop statistical mechanics-based models that can optimize glass composition based on several factors including cementitious reactivity and foaming window.
4. Performing analysis of historical grout waste forms to determine how the various premix components react with the salt simulant.
5. Developing the initial industrial scalability index that helps guide the technoeconomic aspect of the ECM compositional development.

In Year 2, we will focus on completing the development of the IGC space with respect to boron inclusion to increase foaming window size. In addition, we will be working on the inclusion of repurposed waste materials (e.g., recycled glass) into the compositional matrix. Our initial efforts will focus on E glass waste as these materials have the most similar composition to the IGC/USG glasses we have developed.

References

1. Hede, A., D. Reid, and T. Wooley, *Technology and Innovation Roadmap*. 2022, Washington River Protection Solutions, Richland, WA.
2. National Academies of Science, Engineering, and Medicine, *Final Review of the Study on Supplemental Treatment Approaches of Low-Activity Waste at the Hanford Nuclear Reservation: Review #4*. 2020, The National Academies Press: Washington, DC.
3. Herman, C., et al., *R&D Roadmap for Hanford Tank Waste Mission Acceleration*. 2022, Savannah River National Laboratory, Aiken, SC.
4. Bates, W., et al., *Report of Analysis of Approaches to Supplemental Treatment of Low-Activity Waste at the Hanford Nuclear Reservation*. 2019, Savannah River National Laboratory, Aiken, SC.
5. Bernards, J., et al., *River Protection Project System Plan*. 2020, U.S. Department of Energy Office of River Protection, Richland, WA.
6. Wilhite, E.L., et al., *Saltstone processing startup at the Savannah River Plant*. 1988, Savannah River Site (SRS), Aiken, SC (United States). Savannah River ….
7. Langton, C.A. and D.M. Missimer, *X-ray Diffraction of Slag-based Sodium Salt Waste Forms*. 2014, Savannah River National Laboratory.
8. Tripathy, S.K., et al., *Utilisation perspective on water quenched and air-cooled blast furnace slags.* Journal of Cleaner Production, 2020. **262**: p. 121354.
9. Bancroft, G.M., et al., *Lorentzian dominated lineshapes and linewidths for Raman symmetric stretch peaks (800–1200 cm−1) in Qn (n = 1–3) species of alkali silicate glasses/melts.* Journal of Non-Crystalline Solids, 2018. **484**: p. 72-83.

10. O'Shaughnessy, C., et al., *The influence of modifier cations on the Raman stretching modes of Qn species in alkali silicate glasses.* Journal of the American Ceramic Society, 2020. **103**(7): p. 3991-4001.
11. Moulton, B.J.A., et al., *A critical evaluation of barium silicate glass network polymerization.* Journal of Non-Crystalline Solids, 2022. **583**: p. 121477.
12. McMillan, P., *A Raman spectroscopic study of glasses in the system CaO-MgO-SiO_2.* American Mineralogist, 1984. **69**(7-8): p. 645-659.
13. Park, J.H., *Effect of silicate structure on thermodynamic properties of calcium silicate melts: Quantitative analysis of Raman spectra.* Metals and Materials International, 2013. **19**(3): p. 577-584.
14. Mysen, B.O., et al., *Curve-fitting of Raman spectra of silicate glasses.* American Mineralogist, 1982. **67**(7-8): p. 686-695.
15. Moulton, B.J.A., et al., *Speciation and polymerization in a barium silicate glass: Evidence from 29Si NMR and Raman spectroscopies.* Chemical Geology, 2021. **586**: p. 120611.
16. Nesbitt, H.W., et al., *Electron densities over Si and O atoms of tetrahedra and their impact on Raman stretching frequencies and Si-NBO force constants.* Chemical Geology, 2017. **461**: p. 65-74.
17. Koroleva, O.N., et al., *Structure of Na2O–SiO2 melt as a function of composition: In situ Raman spectroscopic study.* Journal of Non-Crystalline Solids, 2013. **375**: p. 62-68.
18. Olivier, L., et al., *Combined 29Si double quantum NMR and MD simulation studies of network connectivities of binary Na2O·SiO2 glasses: new prospects and problems.* Journal of Non-Crystalline Solids, 2001. **293-295**: p. 53-66.
19. Larson, C., et al., *A 29Si MAS NMR study of silicate glasses with a high lithium content.* Journal of Physics: Condensed Matter, 2006. **18**(49): p. 11323.
20. Retsinas, A., A.G. Kalampounias, and G.N. Papatheodorou, *Glass formation and Raman spectra of CaO–SiO2 glasses towards the orthosilicate limit.* Journal of Physics and Chemistry of Solids, 2016. **99**: p. 19-24.
21. Kaseman, D.C., et al., *Q-Speciation and Network Structure Evolution in Invert Calcium Silicate Glasses.* The Journal of Physical Chemistry B, 2015. **119**(26): p. 8440-8445.
22. Bechgaard, T.K., et al., *Structure of MgO/CaO sodium aluminosilicate glasses: Raman spectroscopy study.* Journal of Non-Crystalline Solids, 2017. **470**: p. 145-151.
23. Wójcik, N.A., et al., *The influence of Be addition on the structure and thermal properties of alkali-silicate glasses.* Journal of Non-Crystalline Solids, 2019. **521**: p. 119532.
24. Westsik, J.H., et al., *Supplemental Immobilization of Hanford Low-Activity Waste: Cast Stone Screening Tests*. 2013: United States.
25. Yao, X., et al., *Geopolymerization process of alkali–metakaolinite characterized by isothermal calorimetry.* Thermochimica Acta, 2009. **493**(1-2): p. 49-54.

Appendix A: **Photographs of Glasses**

IGC Compositions

DOE12	

DOE45	
DOE210	

DOE237	
DOE322	

DOE347	
DOE360	

DOE414	
DOE578	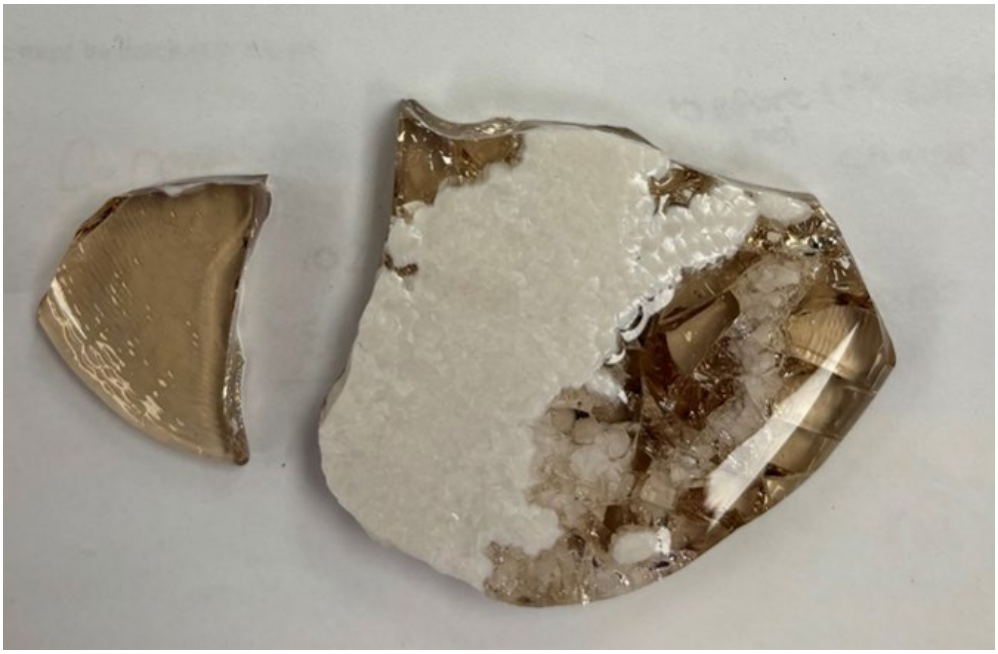

DOE596	
DOE703	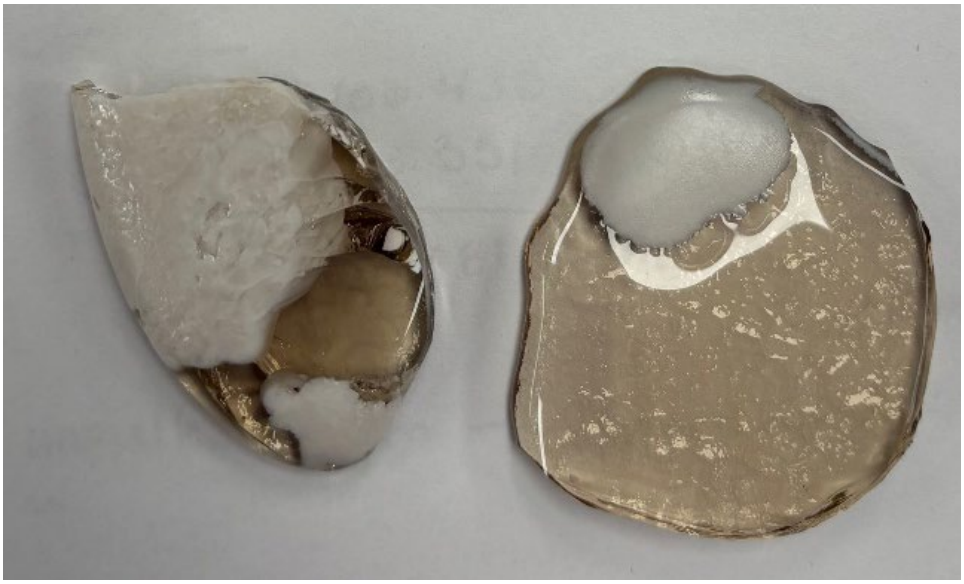

DOE745	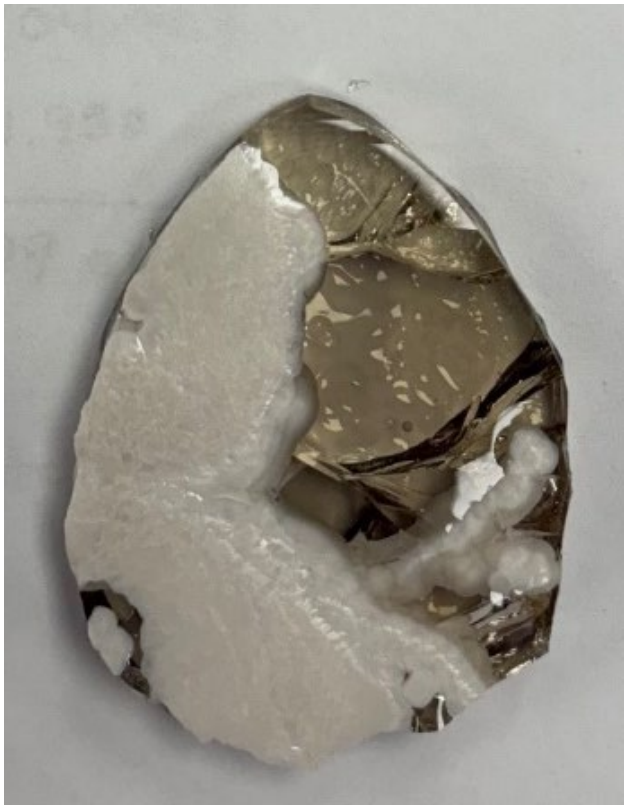
DOE806	

DOE837	
DOE915	

DOE959	

USG Compositions

DOE1001	
DOE1002	

DOE1003	
DOE1004	

DOE1005	
DOE1006	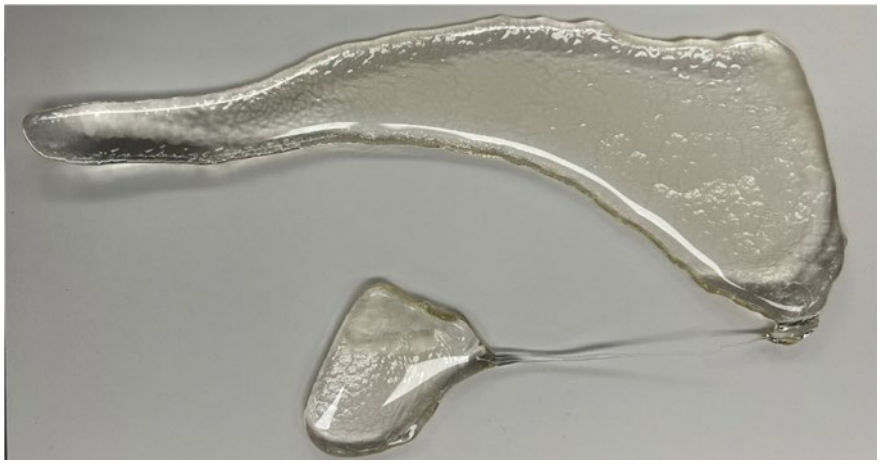

DOE1007	
DOE1008	

DOE1009	
DOE1010	

DOE1011	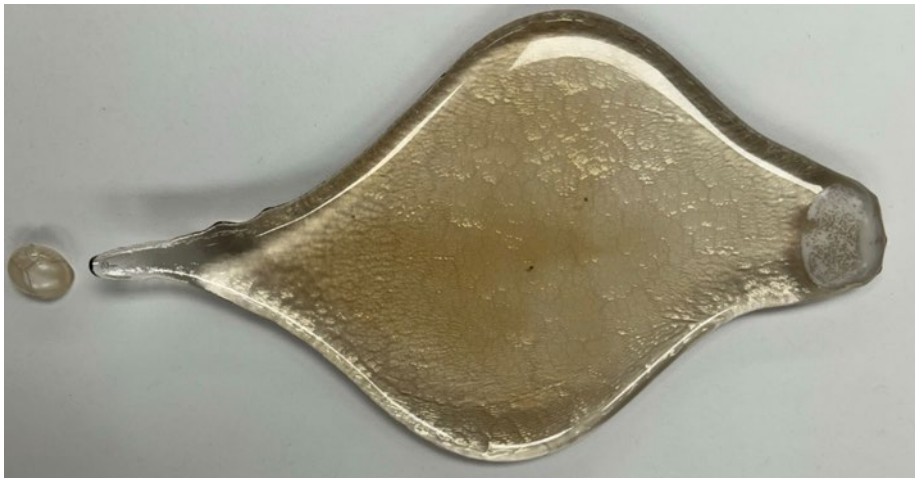
DOE1012	

DOE1013	
DOE1014	

DOE1015	
DOE1016	

DOE1017	

Appendix B: **Viscosity Data**

IGC Compositions

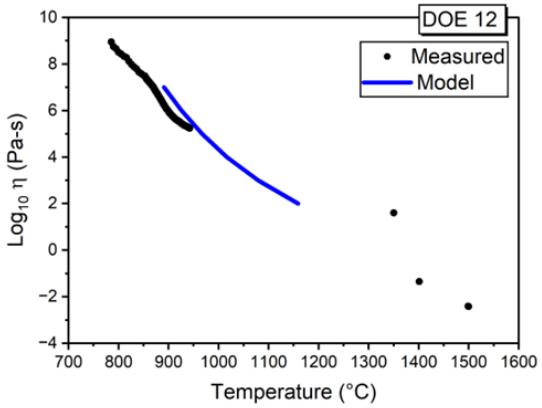

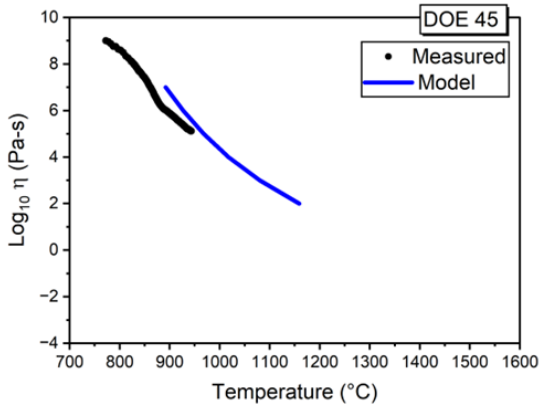

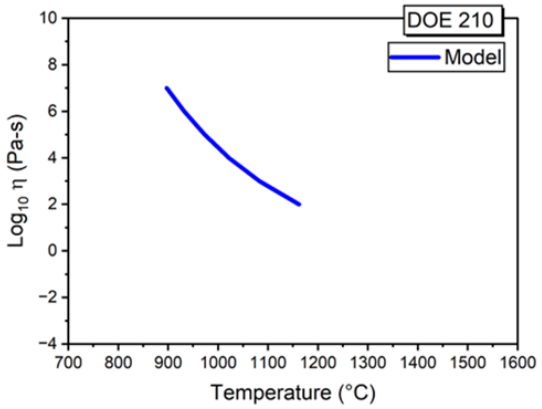

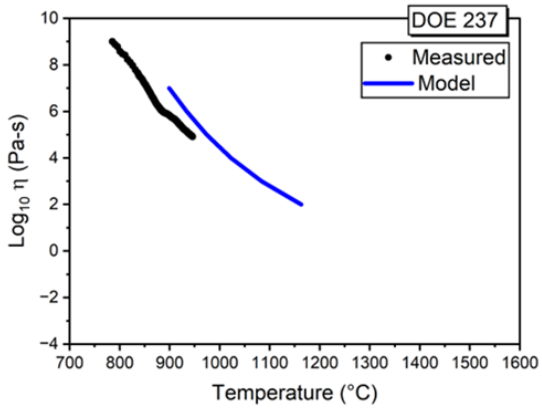

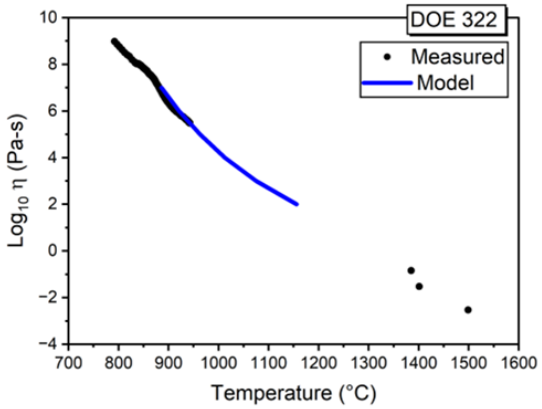

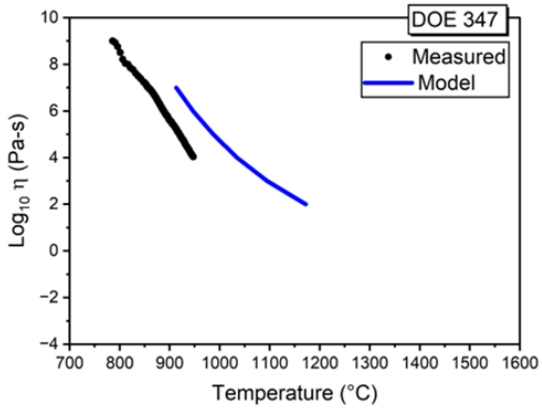

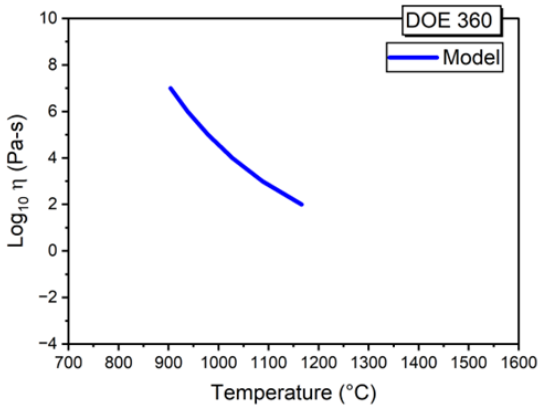
DOE 360
Model
Log10 η (Pa-s)
Temperature (°C)

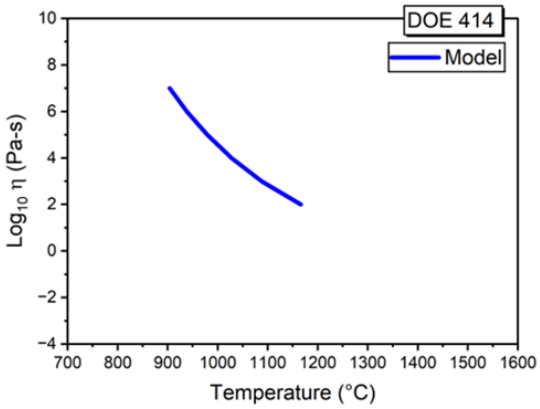
DOE 414
Model
Log10 η (Pa-s)
Temperature (°C)

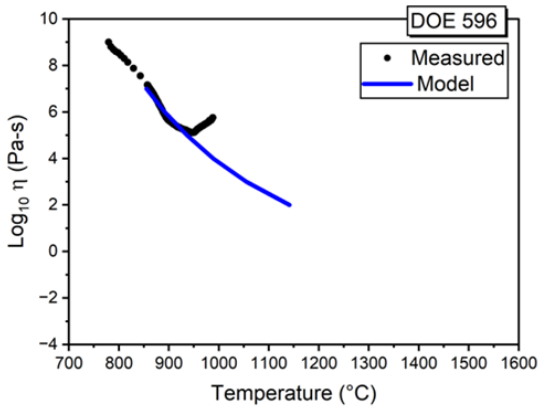
DOE 596
Measured
Model
Log10 η (Pa-s)
Temperature (°C)

USG Compositions

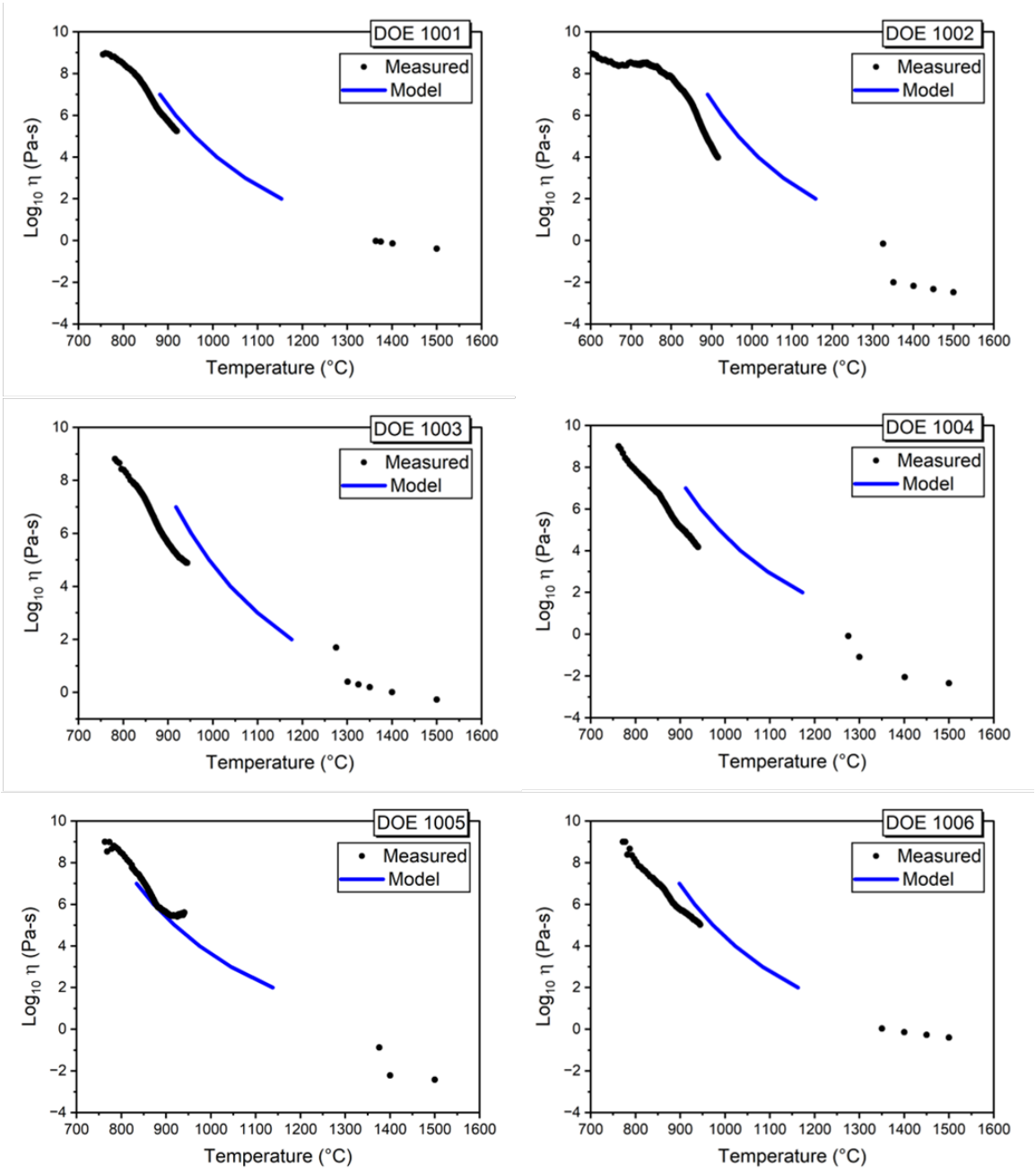

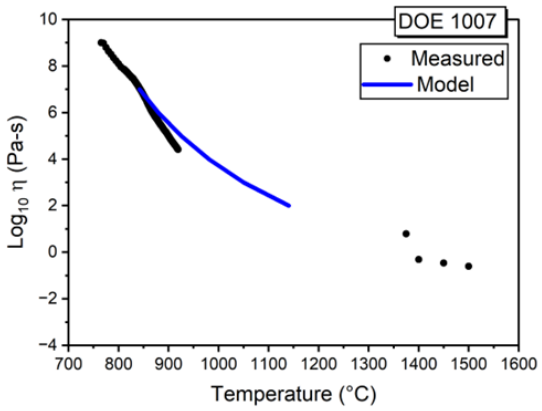
DOE 1007
Measured
Model
Log10 η (Pa-s)
Temperature (°C)

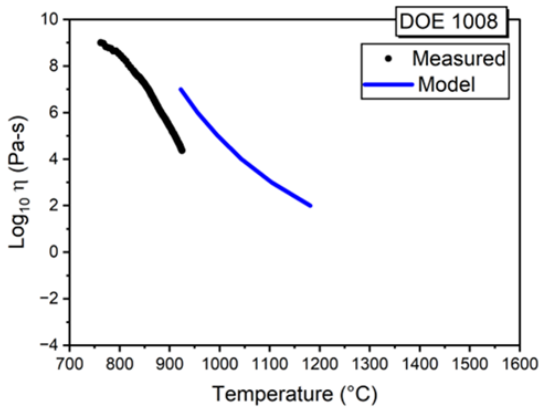
DOE 1008
Measured
Model
Log10 η (Pa-s)
Temperature (°C)

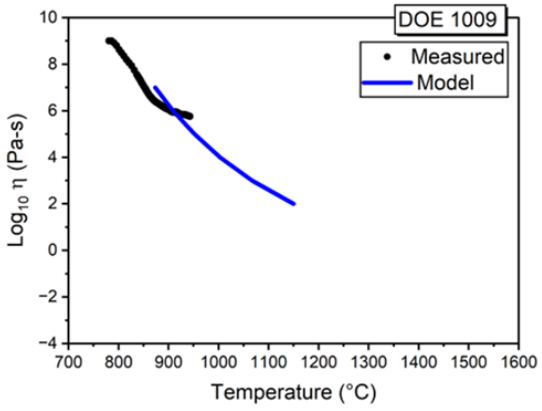
DOE 1009
Measured
Model
Log10 η (Pa-s)
Temperature (°C)

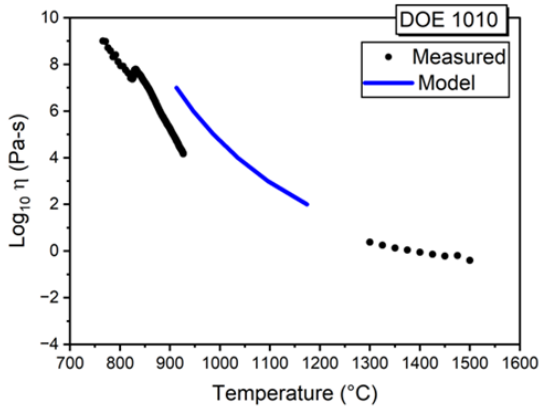
DOE 1010
Measured
Model
Log10 η (Pa-s)
Temperature (°C)

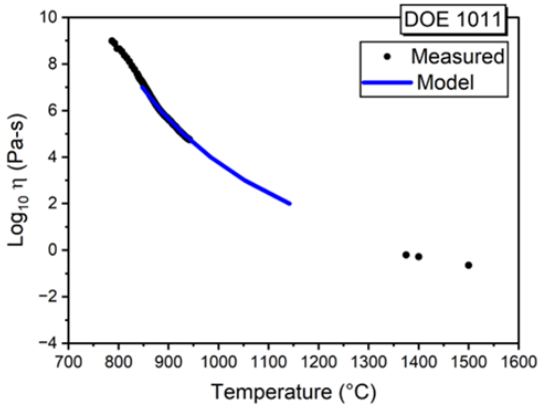
DOE 1011
Measured
Model
Log10 η (Pa-s)
Temperature (°C)

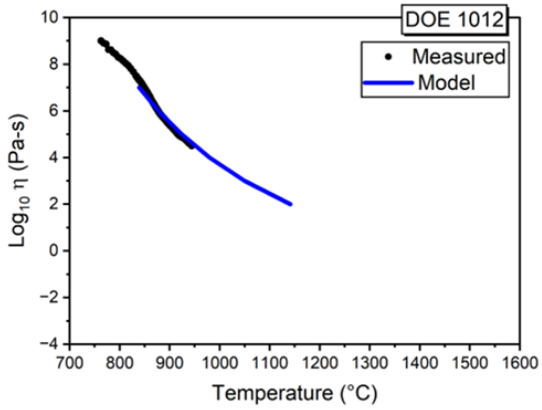
DOE 1012
Measured
Model
Log10 η (Pa-s)
Temperature (°C)

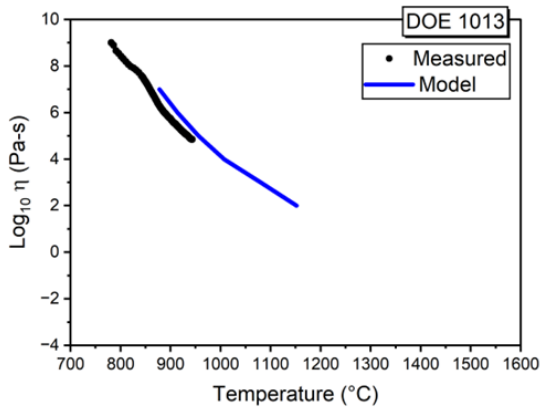
DOE 1013
Measured
Model
Log10 η (Pa-s)
Temperature (°C)

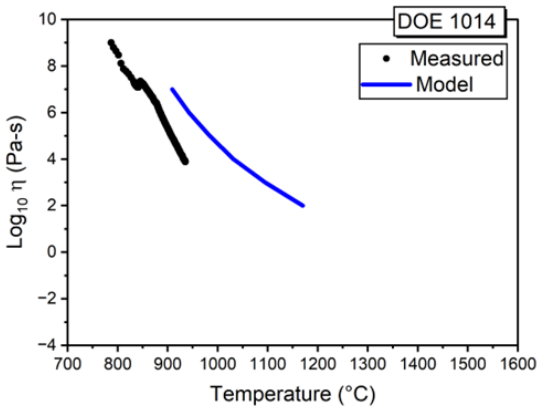
DOE 1014
Measured
Model
Log10 η (Pa-s)
Temperature (°C)

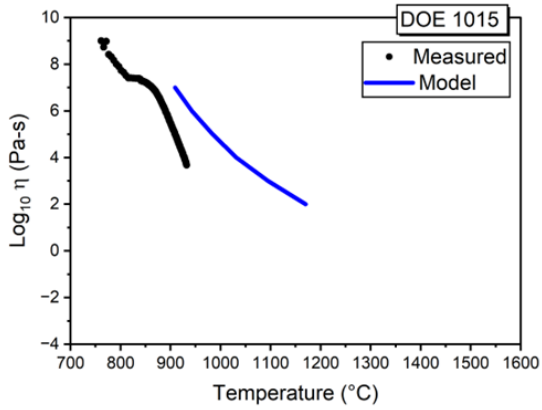
DOE 1015
Measured
Model
Log10 η (Pa-s)
Temperature (°C)

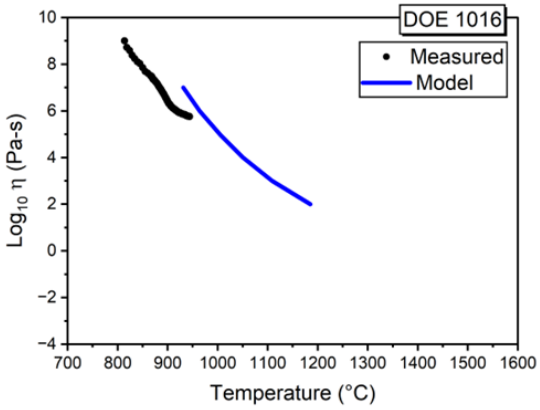
DOE 1016
Measured
Model
Log10 η (Pa-s)
Temperature (°C)

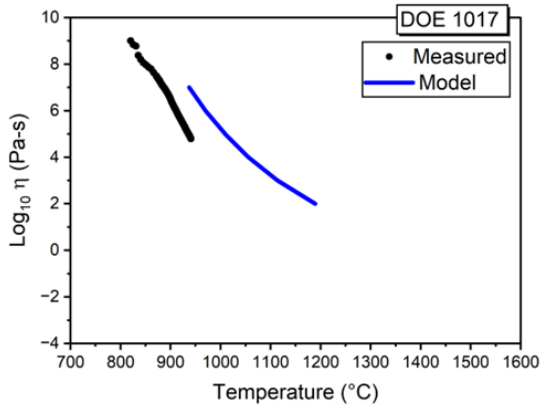
DOE 1017
Measured
Model
Log10 η (Pa-s)
Temperature (°C)

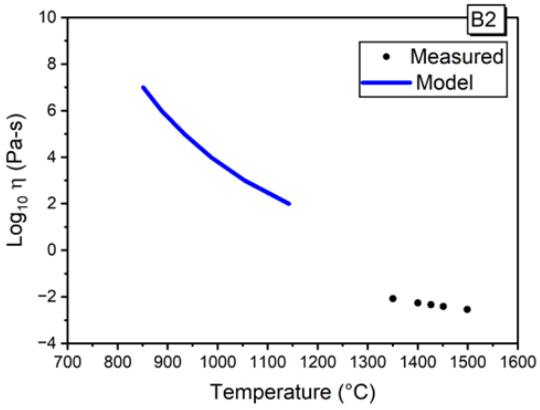
B2
Measured
Model
Log10 η (Pa-s)
Temperature (°C)

Appendix C: **Raman Spectroscopy Fittings**

IGC Compositions

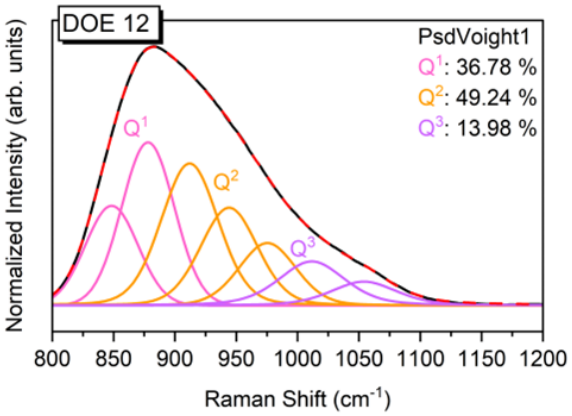

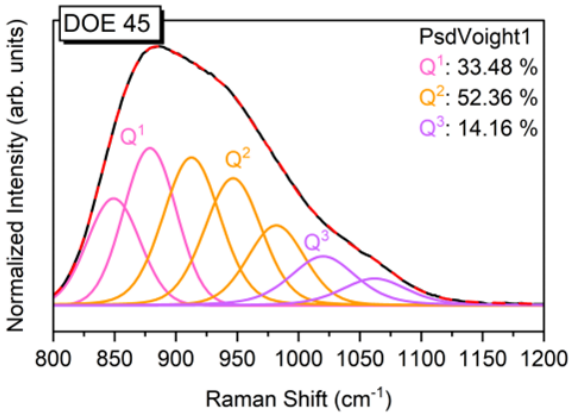

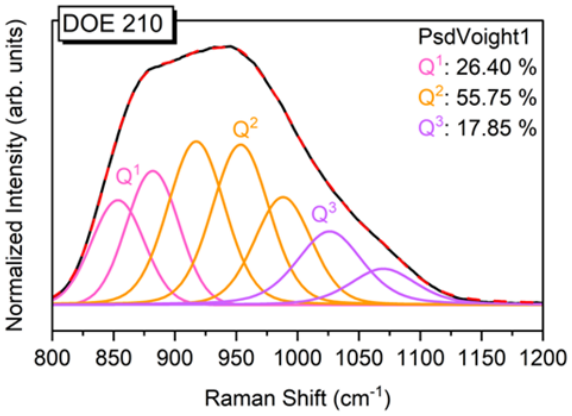

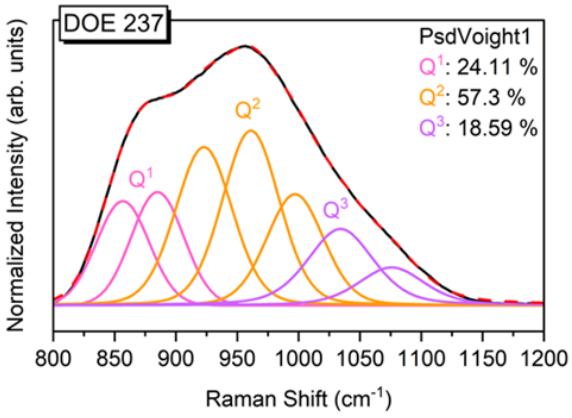

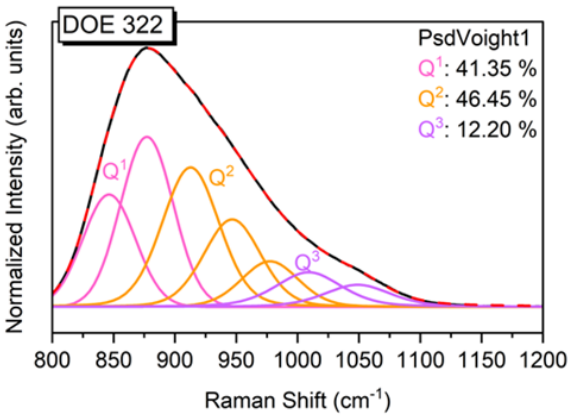

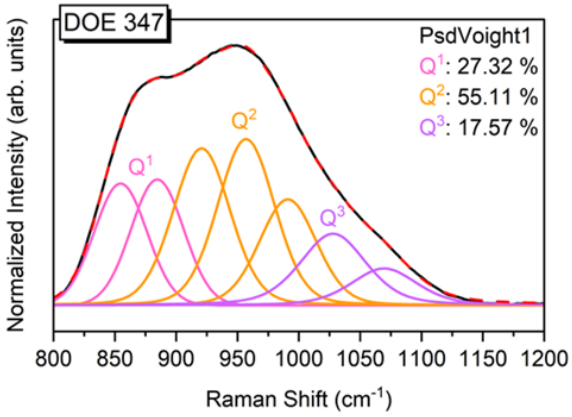

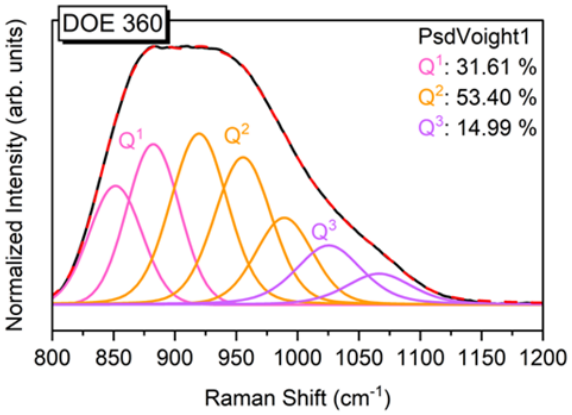
DOE 360
PsdVoight1
Q1: 31.61 %
Q2: 53.40 %
Q3: 14.99 %
Normalized Intensity (arb. units)
Raman Shift (cm-1)
800 850 900 950 1000 1050 1100 1150 1200

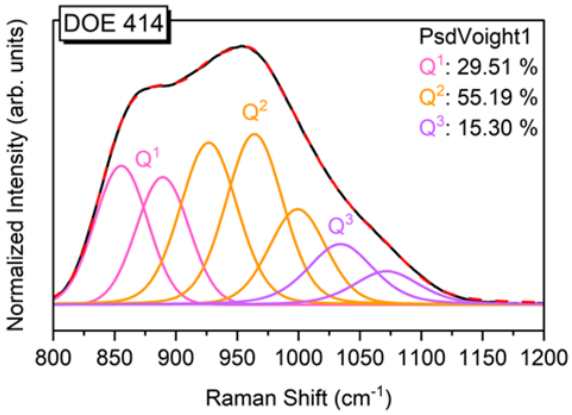
DOE 414
PsdVoight1
Q1: 29.51 %
Q2: 55.19 %
Q3: 15.30 %
Normalized Intensity (arb. units)
Raman Shift (cm-1)
800 850 900 950 1000 1050 1100 1150 1200

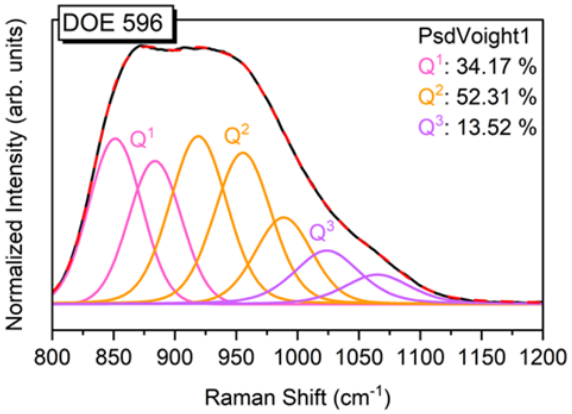
DOE 596
PsdVoight1
Q1: 34.17 %
Q2: 52.31 %
Q3: 13.52 %
Normalized Intensity (arb. units)
Raman Shift (cm-1)
800 850 900 950 1000 1050 1100 1150 1200

USG Compositions

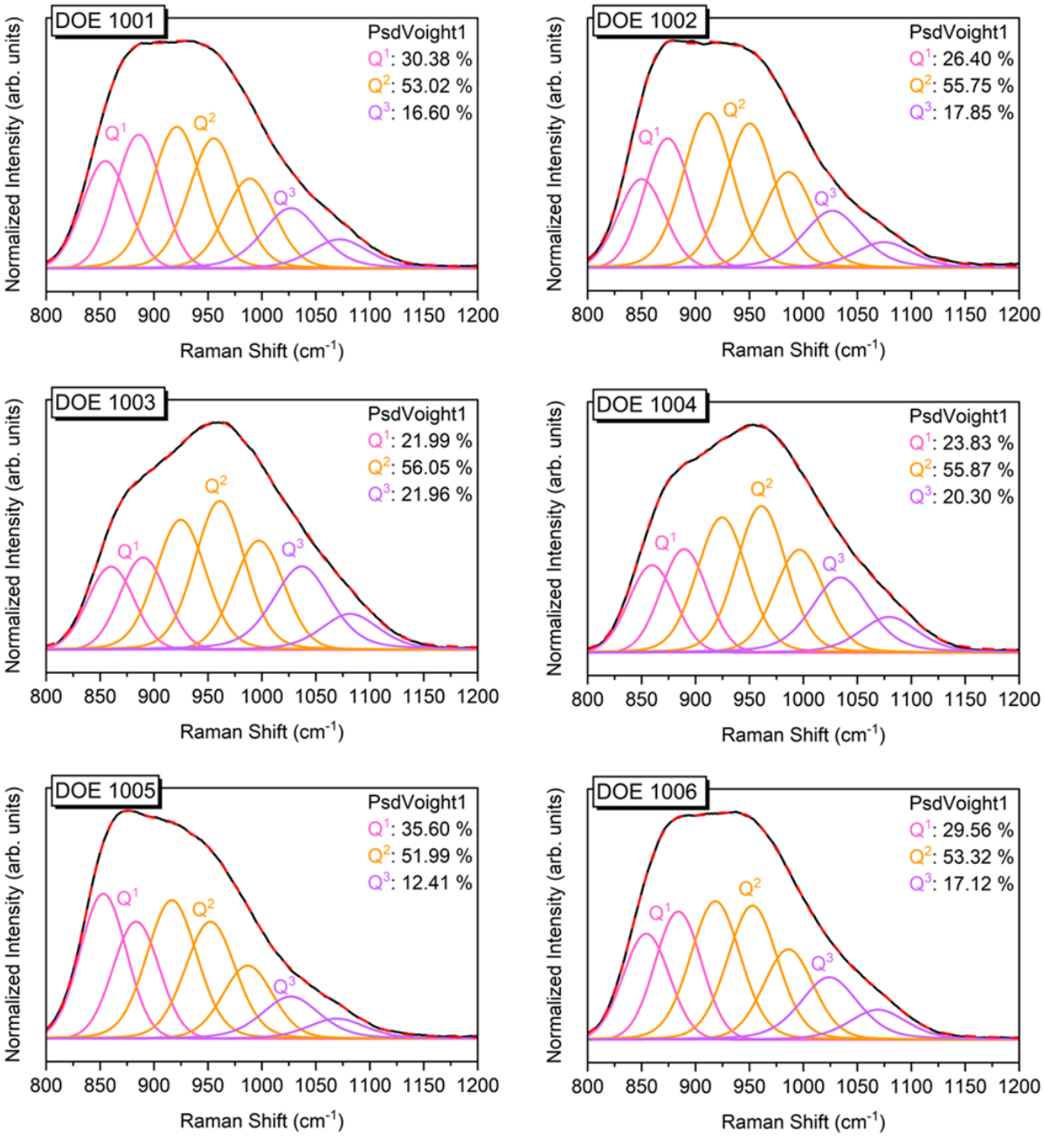

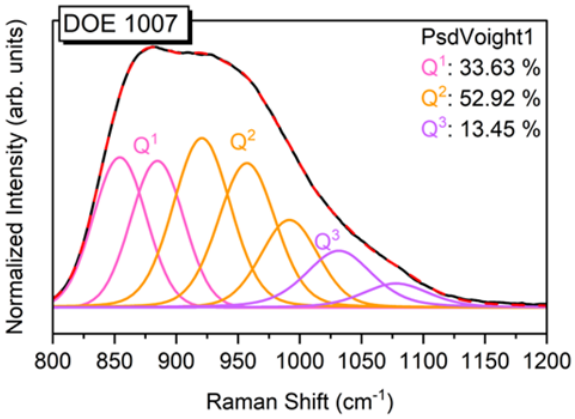
DOE 1007
PsdVoight1
Q1: 33.63 %
Q2: 52.92 %
Q3: 13.45 %
Normalized Intensity (arb. units)
Raman Shift (cm-1)
800 850 900 950 1000 1050 1100 1150 1200

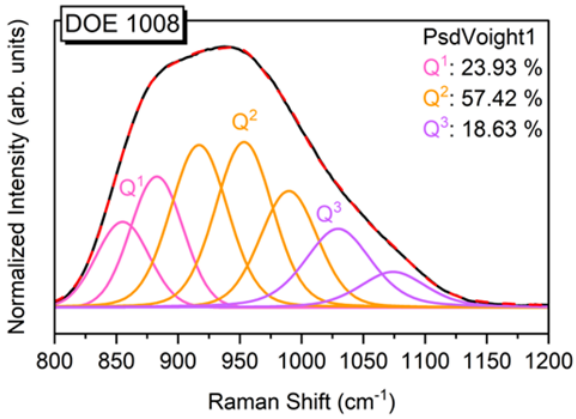
DOE 1008
PsdVoight1
Q1: 23.93 %
Q2: 57.42 %
Q3: 18.63 %
Normalized Intensity (arb. units)
Raman Shift (cm-1)
800 850 900 950 1000 1050 1100 1150 1200

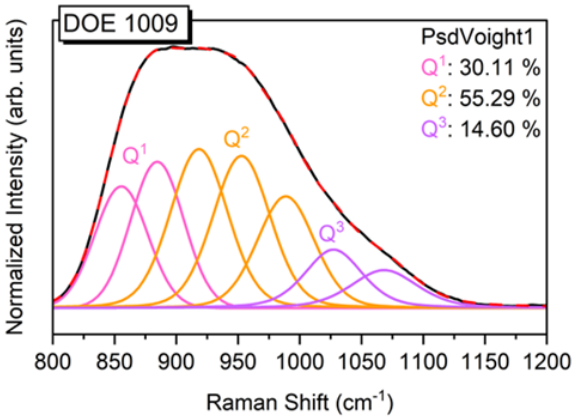
DOE 1009
PsdVoight1
Q1: 30.11 %
Q2: 55.29 %
Q3: 14.60 %
Normalized Intensity (arb. units)
Raman Shift (cm-1)
800 850 900 950 1000 1050 1100 1150 1200

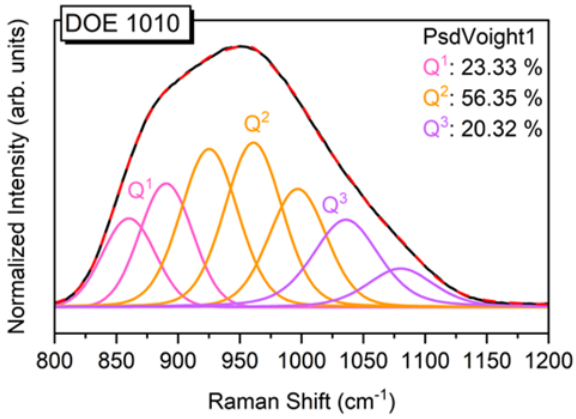
DOE 1010
PsdVoight1
Q1: 23.33 %
Q2: 56.35 %
Q3: 20.32 %
Normalized Intensity (arb. units)
Raman Shift (cm-1)
800 850 900 950 1000 1050 1100 1150 1200

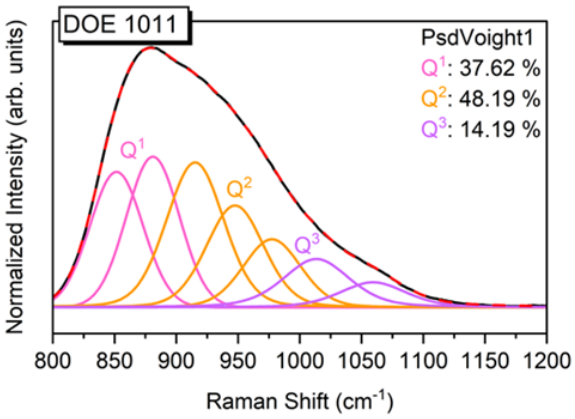
DOE 1011
PsdVoight1
Q1: 37.62 %
Q2: 48.19 %
Q3: 14.19 %
Normalized Intensity (arb. units)
Raman Shift (cm-1)
800 850 900 950 1000 1050 1100 1150 1200

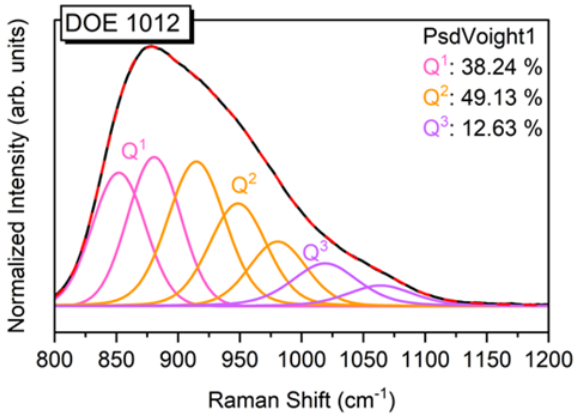
DOE 1012
PsdVoight1
Q1: 38.24 %
Q2: 49.13 %
Q3: 12.63 %
Normalized Intensity (arb. units)
Raman Shift (cm-1)
800 850 900 950 1000 1050 1100 1150 1200

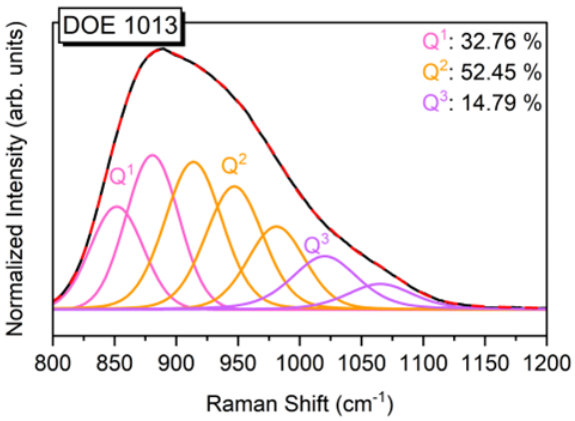
DOE 1013
Q1: 32.76 %
Q2: 52.45 %
Q3: 14.79 %
Normalized Intensity (arb. units)
Raman Shift (cm-1)

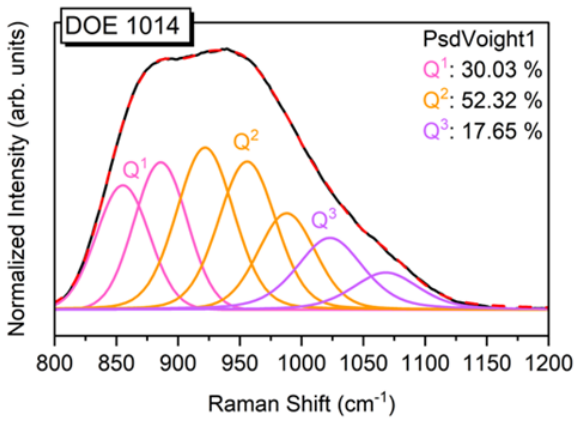
DOE 1014
PsdVoight1
Q1: 30.03 %
Q2: 52.32 %
Q3: 17.65 %
Normalized Intensity (arb. units)
Raman Shift (cm-1)

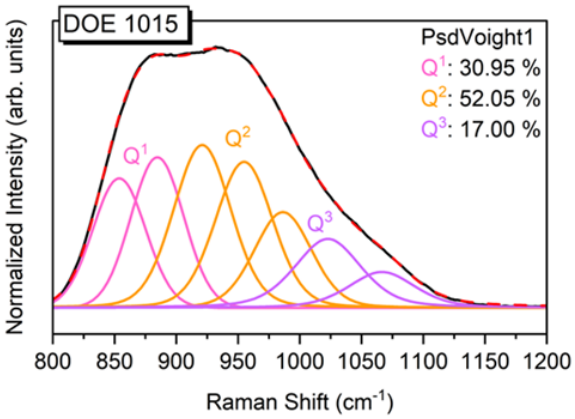
DOE 1015
PsdVoight1
Q1: 30.95 %
Q2: 52.05 %
Q3: 17.00 %
Normalized Intensity (arb. units)
Raman Shift (cm-1)

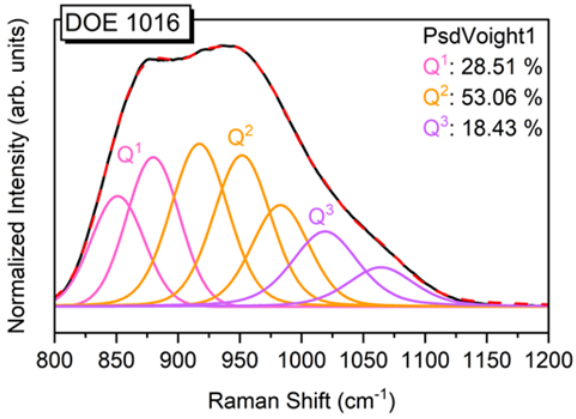
DOE 1016
PsdVoight1
Q1: 28.51 %
Q2: 53.06 %
Q3: 18.43 %
Normalized Intensity (arb. units)
Raman Shift (cm-1)

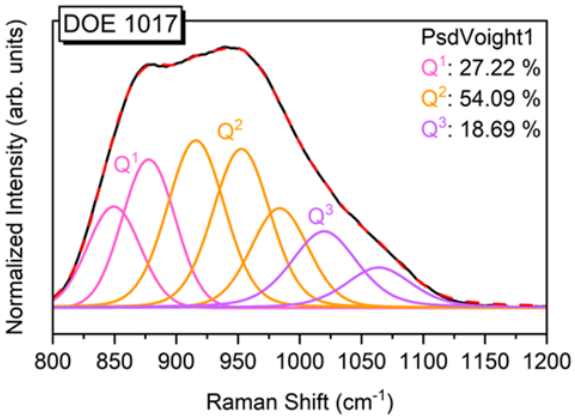
DOE 1017
PsdVoight1
Q1: 27.22 %
Q2: 54.09 %
Q3: 18.69 %
Normalized Intensity (arb. units)
Raman Shift (cm-1)

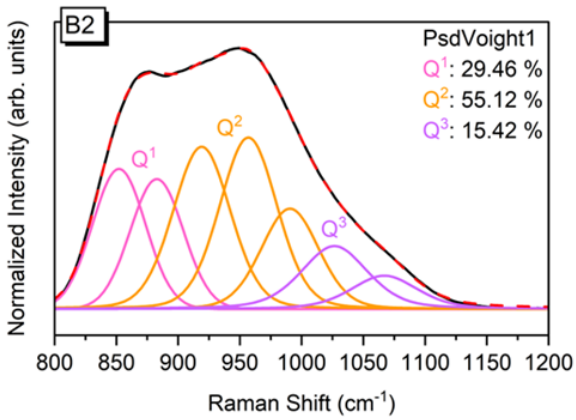
B2
PsdVoight1
Q1: 29.46 %
Q2: 55.12 %
Q3: 15.42 %
Normalized Intensity (arb. units)
Raman Shift (cm-1)

Appendix D: Differential Scanning Calorimetry Data

IGC Compositions

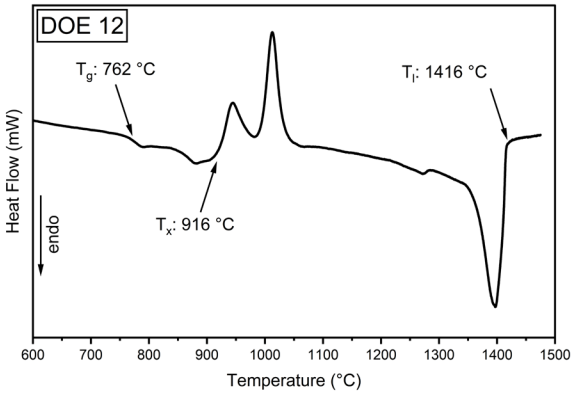

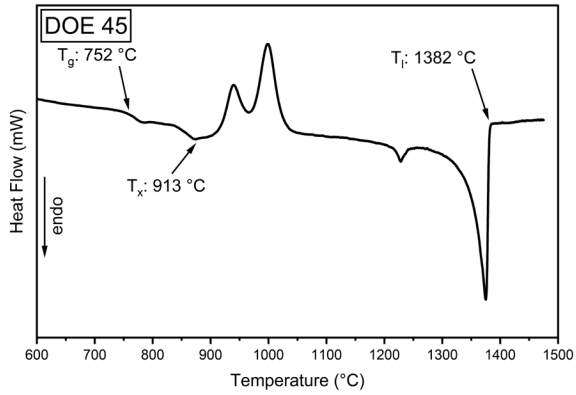

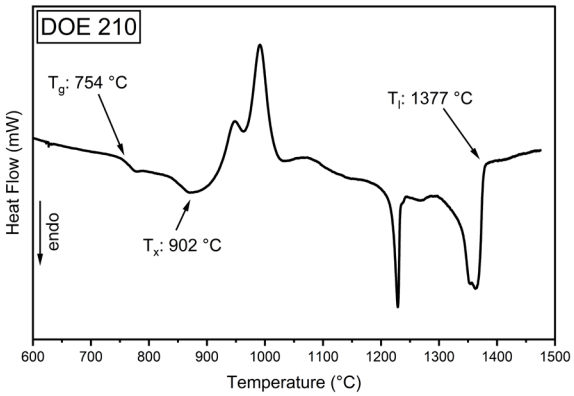

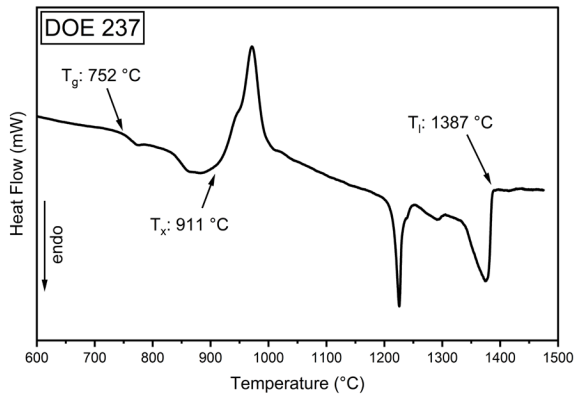

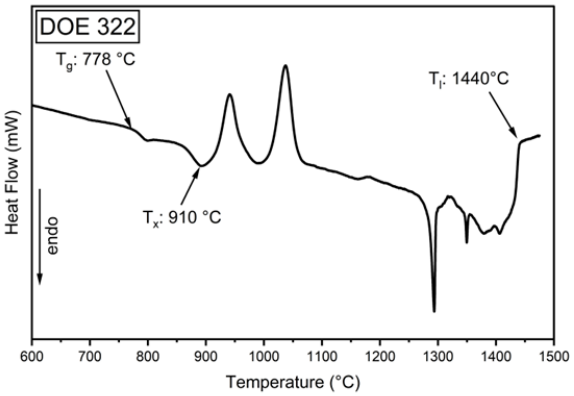

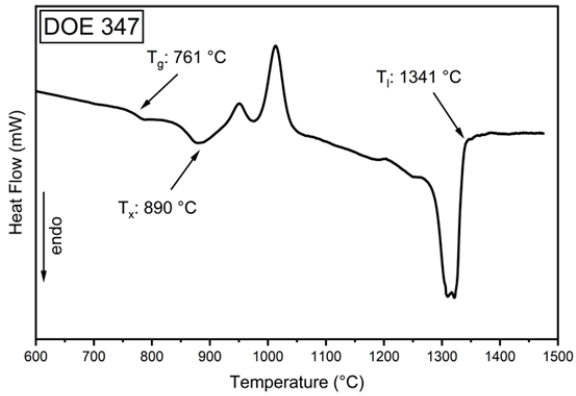

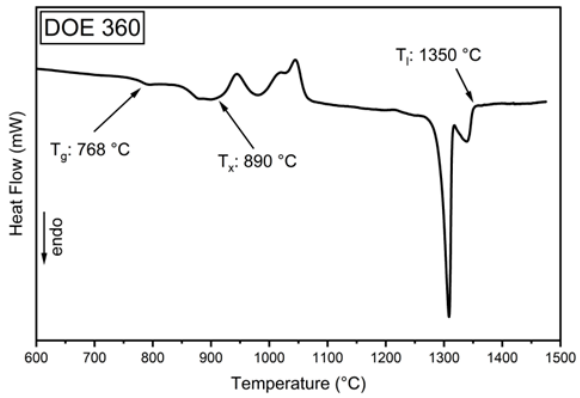
DOE 360
T_i: 1350 °C
T_g: 768 °C
T_x: 890 °C
Heat Flow (mW)
endo
600 700 800 900 1000 1100 1200 1300 1400 1500
Temperature (°C)

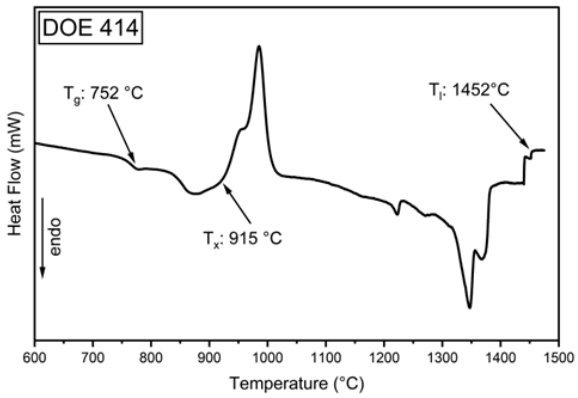
DOE 414
T_g: 752 °C
T_i: 1452°C
T_x: 915 °C
Heat Flow (mW)
endo
600 700 800 900 1000 1100 1200 1300 1400 1500
Temperature (°C)

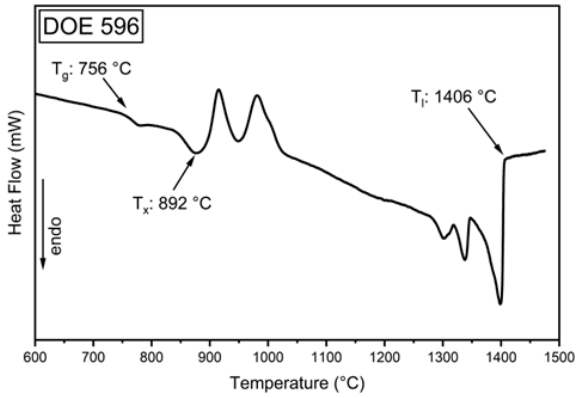
DOE 596
T_g: 756 °C
T_i: 1406 °C
T_x: 892 °C
Heat Flow (mW)
endo
600 700 800 900 1000 1100 1200 1300 1400 1500
Temperature (°C)

USG Compositions

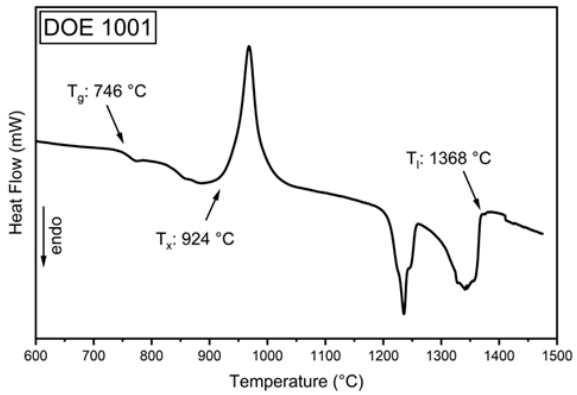

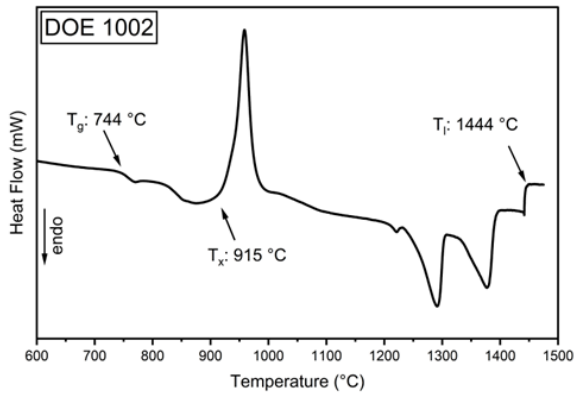

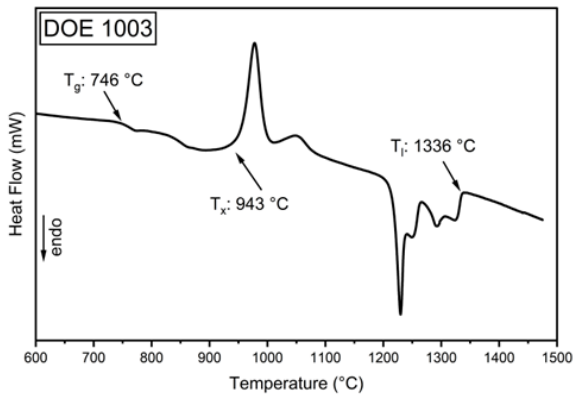

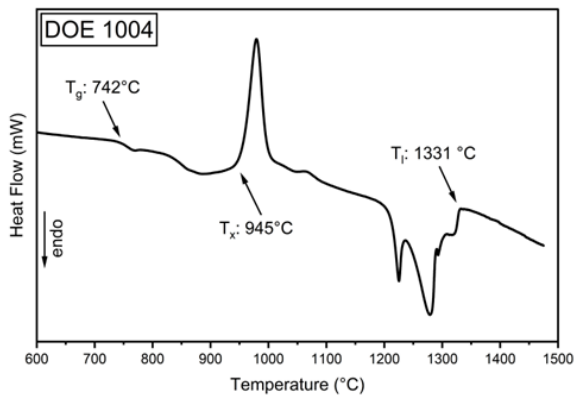

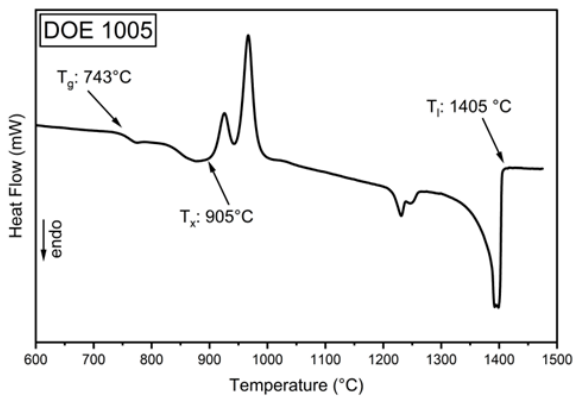

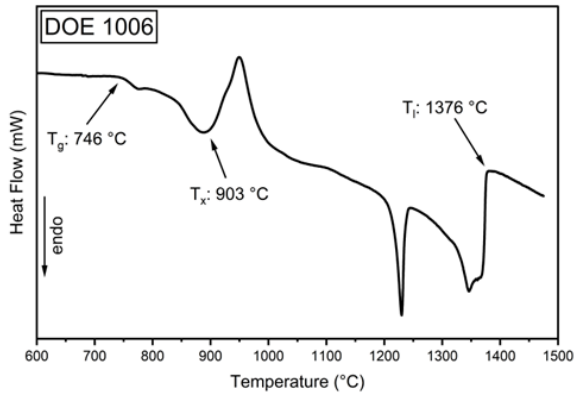

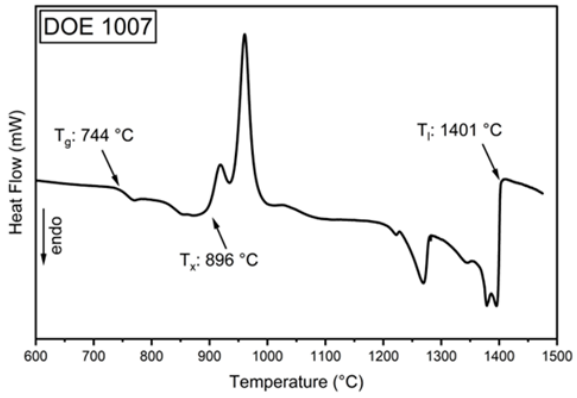
DOE 1007
T_g: 744 °C
T_x: 896 °C
T_l: 1401 °C
Heat Flow (mW)
endo
600 700 800 900 1000 1100 1200 1300 1400 1500
Temperature (°C)

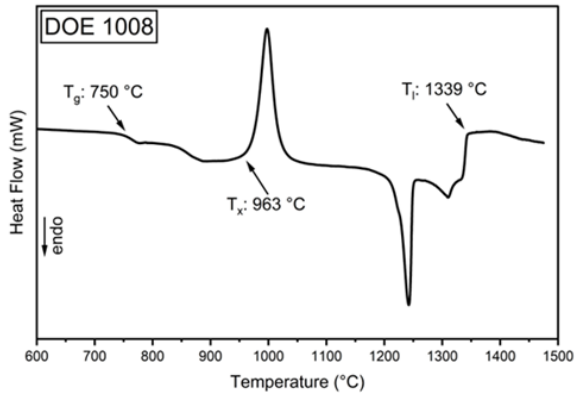
DOE 1008
T_g: 750 °C
T_x: 963 °C
T_l: 1339 °C
Heat Flow (mW)
endo
600 700 800 900 1000 1100 1200 1300 1400 1500
Temperature (°C)

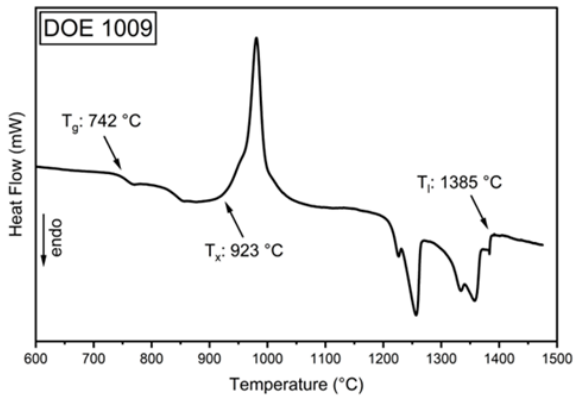
DOE 1009
T_g: 742 °C
T_x: 923 °C
T_l: 1385 °C
Heat Flow (mW)
endo
600 700 800 900 1000 1100 1200 1300 1400 1500
Temperature (°C)

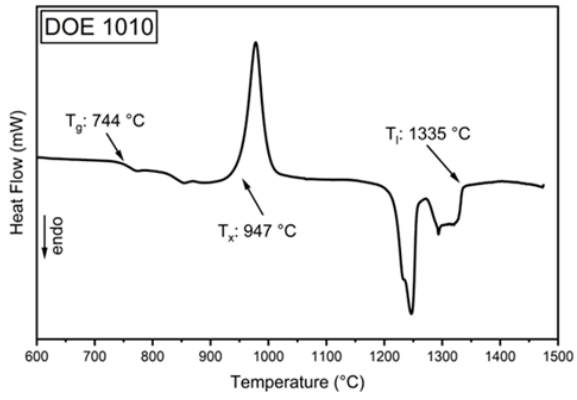
DOE 1010
T_g: 744 °C
T_x: 947 °C
T_l: 1335 °C
Heat Flow (mW)
endo
600 700 800 900 1000 1100 1200 1300 1400 1500
Temperature (°C)

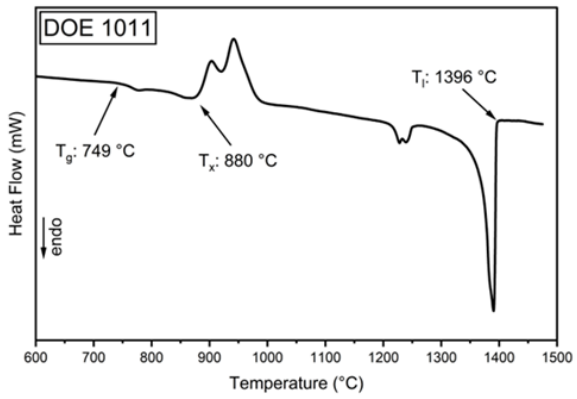
DOE 1011
T_g: 749 °C
T_x: 880 °C
T_l: 1396 °C
Heat Flow (mW)
endo
600 700 800 900 1000 1100 1200 1300 1400 1500
Temperature (°C)

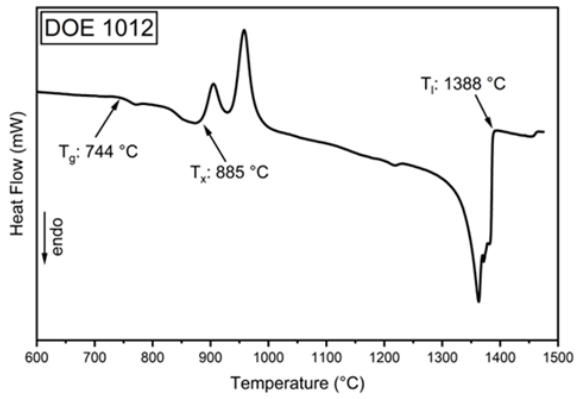
DOE 1012
T_g: 744 °C
T_x: 885 °C
T_l: 1388 °C
Heat Flow (mW)
endo
600 700 800 900 1000 1100 1200 1300 1400 1500
Temperature (°C)

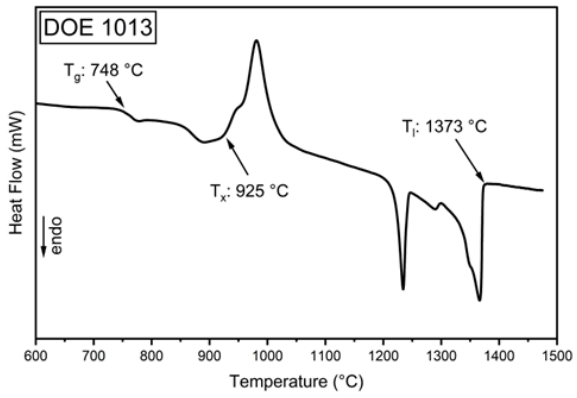
DOE 1013
T_g: 748 °C
T_x: 925 °C
T_l: 1373 °C
Heat Flow (mW)
endo
600 700 800 900 1000 1100 1200 1300 1400 1500
Temperature (°C)

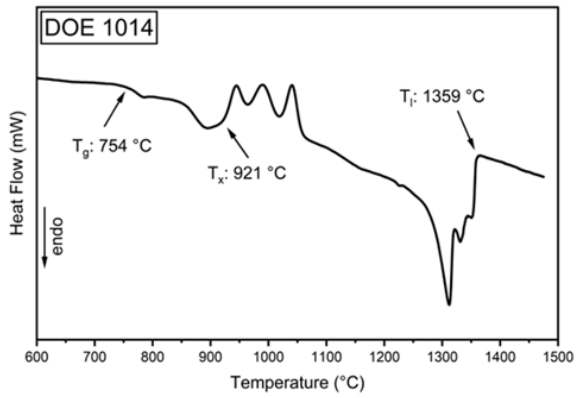
DOE 1014
T_g: 754 °C
T_x: 921 °C
T_l: 1359 °C
Heat Flow (mW)
endo
600 700 800 900 1000 1100 1200 1300 1400 1500
Temperature (°C)

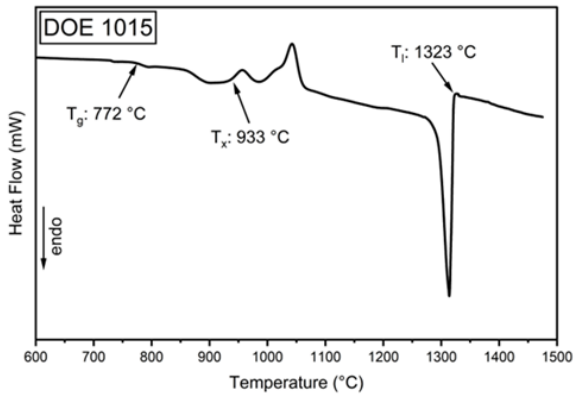
DOE 1015
T_g: 772 °C
T_x: 933 °C
T_l: 1323 °C
Heat Flow (mW)
endo
600 700 800 900 1000 1100 1200 1300 1400 1500
Temperature (°C)

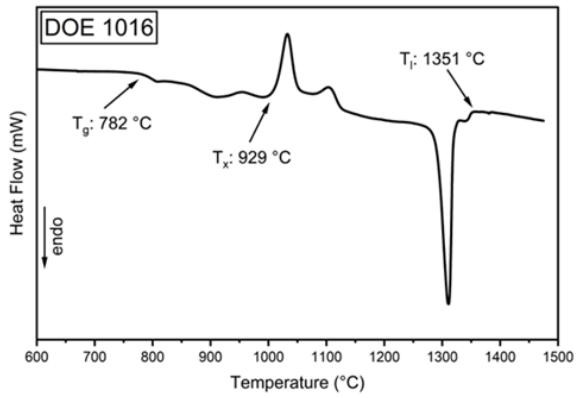
DOE 1016
T_g: 782 °C
T_x: 929 °C
T_l: 1351 °C
Heat Flow (mW)
endo
600 700 800 900 1000 1100 1200 1300 1400 1500
Temperature (°C)

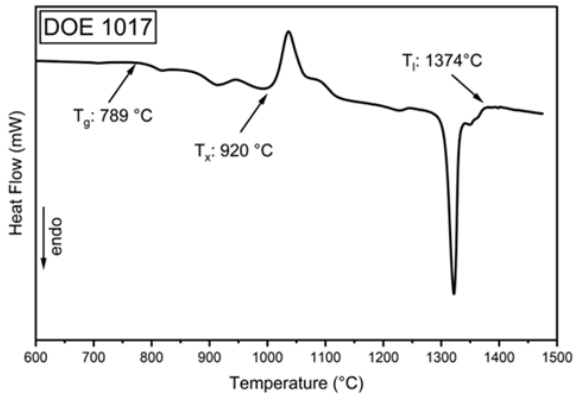
DOE 1017
T_g: 789 °C
T_x: 920 °C
T_l: 1374°C
Heat Flow (mW)
endo
600 700 800 900 1000 1100 1200 1300 1400 1500
Temperature (°C)

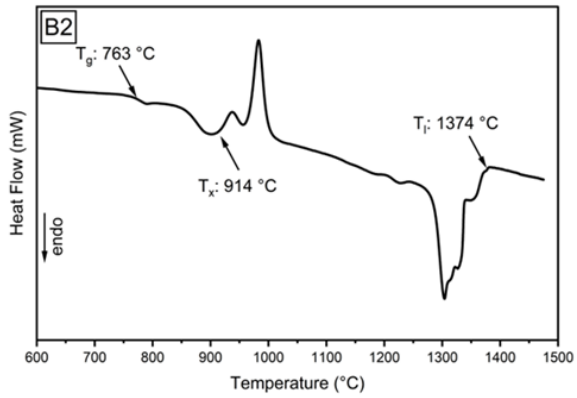
B2
T_g: 763 °C
T_x: 914 °C
T_l: 1374 °C
Heat Flow (mW)
endo
600 700 800 900 1000 1100 1200 1300 1400 1500
Temperature (°C)